ATLAS CONF Note

ATLAS-CONF-2020-015

24th May 2020

Search for chargino-neutralino pair production in final states with three leptons and missing transverse momentum in $\sqrt{s} = 13$ TeV pp collisions with the ATLAS detector

The ATLAS Collaboration

A search for chargino-neutralino pair production in three-lepton final states with missing transverse momentum in $\sqrt{s} = 13$ TeV pp collisions with the ATLAS detector is presented. The search targets a model in which the chargino ($\tilde{\chi}_1^{\pm}$) and next-to-lightest neutralino ($\tilde{\chi}_2^0$) are mass degenerate. The $\tilde{\chi}_1^{\pm}$ decays to a lightest neutralino ($\tilde{\chi}_1^0$) and a W boson, while the $\tilde{\chi}_2^0$ decays to a $\tilde{\chi}_1^0$ and a Z or Higgs (h) boson. Only leptonic decays of the Standard Model bosons are considered. Strategies targeting scenarios where the mass difference between the $\tilde{\chi}_1^{\pm}/\tilde{\chi}_2^0$ and $\tilde{\chi}_1^0$ is above the Z-boson mass, with on-shell W and Z bosons or W and h bosons, and scenarios where the mass difference is between 10-90 GeV, with off-shell W^* and Z^* bosons, are discussed. A dataset corresponding to an integrated luminosity of 139 fb^{-1} is used and no significant excess is found in data with respect to the Standard Model predictions. Exclusion limits at 95% confidence level are set on a simplified model of pure wino $\tilde{\chi}_1^{\pm}\tilde{\chi}_2^0$ pair production. Models with $\tilde{\chi}_1^{\pm}$ and $\tilde{\chi}_2^0$ masses up to 640 GeV for decays via on-shell W and Z bosons and massless $\tilde{\chi}_1^0$, up to 300 GeV for decays via off-shell W^* and Z^* bosons, and up to 185 GeV for decays via W and h bosons and $\tilde{\chi}_1^0$ masses less than 20 GeV are excluded.

ATLAS-CONF-2020-015
01 June 2020

1 Introduction

Supersymmetry (SUSY) [1–6] predicts new particles that have identical quantum numbers to their Standard Model (SM) partners with the exception of spin, with SM fermions having bosonic partners and SM bosons having fermionic partners. The neutralinos $\widetilde{\chi}^0_{1,2,3,4}$ and charginos $\widetilde{\chi}^\pm_{1,2}$ are collectively referred to as electroweakinos, where the subscripts indicate increasing electroweakino mass. The electroweakino states are formed via a mixing of the SUSY partners of the electroweak gauge fields, the bino for the $U(1)_Y$, the winos for the $SU(2)_L$ fields, and the higgsinos for the Higgs field.

In the minimal supersymmetric extension of the SM (MSSM) [7, 8], M_1, M_2 and μ, are the mass parameters for the bino, wino, and higgsino states, respectively. In scenarios with large values of the ratio of the vacuum expectation value of the two Higgs fields, $\tan(\beta)$, the phenomenology of the electroweakinos is driven by these three mass parameters. If the $\widetilde{\chi}^0_1$ is stable, e.g. as the lightest supersymmetric particle (LSP) in R-parity-conserving SUSY models [9], it is a viable dark-matter candidate [10, 11].

This note presents a search targeting the direct pair production of the lightest chargino ($\widetilde{\chi}^\pm_1$) and the next-to-lightest neutralino ($\widetilde{\chi}^0_2$), with $\widetilde{\chi}^\pm_1$ and $\widetilde{\chi}^0_2$ decaying into $\widetilde{\chi}^0_1$ via a W boson and a Z boson (WZ-mediated) or via a W boson and a Higgs boson (Wh-mediated), as illustrated in Figure 1. The analysis focuses on final state signatures with exactly three light-flavour charged leptons - electrons or muons - and missing transverse momentum $\mathbf{p}_{\mathrm{T}}^{\mathrm{miss}}$ of magnitude $E_{\mathrm{T}}^{\mathrm{miss}}$, where one lepton originates from a leptonic decay of a W boson and two leptons come from the decay of a Z or Higgs boson. Additional jets originating from the presence of initial-state radiation (ISR) are considered, and enhance the missing transverse momentum signature component.

The signatures are inspired by a scenario where mass parameters $|M_1| < |M_2| \ll |\mu|$ are assumed such that the produced electroweakinos have a wino and/or bino nature, with the $\widetilde{\chi}^\pm_1$ and $\widetilde{\chi}^0_2$ being wino dominated, and the $\widetilde{\chi}^0_1$ LSP being bino dominated. Such hierarchy is typically predicted by either a class of models in the framework of gaugino mass unification at the GUT scale (including mSUGRA [12, 13] and cMSSM [14]), or MSSM parameter space explaining the possible discrepancy between the measured muon anomalous magnetic moment and its SM predictions [15–17]. When the mass splitting between $\widetilde{\chi}^\pm_1$ and $\widetilde{\chi}^0_1$ is 15-30 GeV, this hierarchy is also motivated by the fact that the LSP naturally can be a thermal-relic dark-matter candidate that was depleted in the early universe through co-annihilation processes to match the observed dark-matter density [18–23]. This scenario, often referred to as the bino-wino coannihilation dark-matter scenario in the literature, is poorly constrained by dark-matter direct-detection experiments, and collider searches constitute the only direct probe for $|\mu| > 800$ GeV [22].

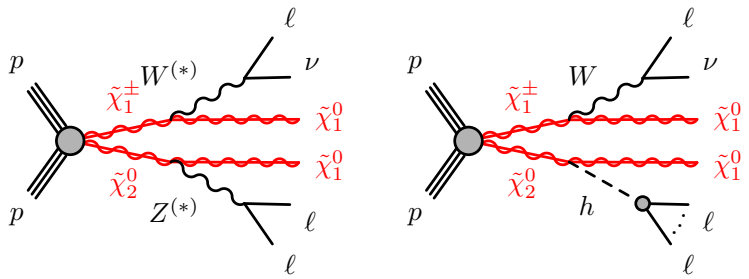

Figure 1: Diagrams of the targeted simplified models: $\tilde{\chi}^\pm_1\tilde{\chi}^0_2$ pair production with subsequent decays into two $\tilde{\chi}^0_1$, via leptonically decaying W, Z and Higgs bosons, three leptons and a neutrino. Diagrams are shown for (left) intermediate WZ (W^*Z^*) as well as (right) intermediate Wh.

In the simplified models [24–26] considered for optimisation of the selections and interpretation of the results the $\widetilde{\chi}_1^{\pm}$ and $\widetilde{\chi}_2^0$ are assumed to be mass degenerate and purely wino. All the other SUSY particles are assumed to be heavier, such that they do not affect the production and decay of the $\widetilde{\chi}_1^{\pm}$ and $\widetilde{\chi}_2^0$. The relative sign of the two neutralino mass parameters $m(\tilde{\chi}_2^0) \times m(\tilde{\chi}_1^0)$ is assumed to be positive in this analysis. The following three simplified model scenarios of $\tilde{\chi}_1^{\pm}\tilde{\chi}_2^0$ pair production are considered with dedicated selections:

- **On-shell *WZ*** selection: $\tilde{\chi}_2^0 \to Z\tilde{\chi}_1^0$ with 100% branching-ratio, where $\Delta m(\tilde{\chi}_1^{\pm}/\tilde{\chi}_2^0, \tilde{\chi}_1^0) \gtrsim m_Z$,
- **Off-shell *WZ*** selection: $\tilde{\chi}_2^0 \to Z\tilde{\chi}_1^0$ with 100% branching-ratio, where $\Delta m(\tilde{\chi}_1^{\pm}/\tilde{\chi}_2^0, \tilde{\chi}_1^0) < m_Z$,
- ***Wh*** selection: $\tilde{\chi}_2^0 \to h\tilde{\chi}_1^0$ with 100% branching-ratio, where $\Delta m(\tilde{\chi}_1^{\pm}/\tilde{\chi}_2^0, \tilde{\chi}_1^0) > m_h$,

where a 100% branching ratio is assumed for $\tilde{\chi}_1^{\pm} \to W\tilde{\chi}_1^0$ for all the models. Unless otherwise indicated, Δm will refer to $\Delta m(\tilde{\chi}_1^{\pm}/\tilde{\chi}_2^0, \tilde{\chi}_1^0)$ in the rest of this note.

Previous searches at the LHC targeting these models are reported by the ATLAS [27–33] and CMS collaborations [34–40]. For $\widetilde{\chi}_1^{\pm}\widetilde{\chi}_2^0$ production with decays via WZ and 3ℓ final states, limits were set for $\widetilde{\chi}_1^{\pm}/\widetilde{\chi}_2^0$ masses up to 500 GeV for massless $\tilde{\chi}_1^0$, up to 200 GeV for $\Delta m \sim m_Z$, and up to 240 GeV for $50 < \Delta m < m_Z$ [35]. Limits for mass splittings $\Delta m < 50$ GeV were set in 2ℓ final states for $\widetilde{\chi}_1^{\pm}/\widetilde{\chi}_2^0$ masses up to 250 GeV [31]. For decays via Wh and 3ℓ final states, limits were set up to 150 GeV for massless $\widetilde{\chi}_1^0$, and up to 145 GeV for a $\widetilde{\chi}_1^0$ mass of 20 GeV [30].

This note extends the previous results by analysing the full LHC Run 2 dataset, improving the signal selection strategies – particularly for intermediate mass splittings, and exploiting improved particle reconstruction performance. Significant gains in lepton identification and isolation performance follow from updates in the electron reconstruction as well as from the use of a novel multi-variate discriminant [41].

A brief overview of the ATLAS detector is presented in Section 2, followed by a description of the dataset and Monte Carlo simulation in Section 3. After a discussion of the event reconstruction and physics objects used in the analysis in Section 4, Section 5 covers the general analysis strategy including the definition of signal regions, background estimation techniques and the systematic uncertainties. This is followed by Section 6, with details specific to the on-shell WZ and Wh selections, and Section 7, with details specific to the off-shell WZ selection. Results are presented in Section 8, together with the interpretation in the context of relevant SUSY scenarios. Finally Section 9 summarises the main conclusions.

2 ATLAS detector

The ATLAS detector [42] is a general-purpose particle detector with almost 4π solid angle coverage around the interaction point.[1] It consists of an inner tracking system surrounded by a superconducting solenoid, sampling electromagnetic and hadronic calorimeters, and a muon spectrometer encompassing three superconducting toroidal magnets with eight coils each.

[1] ATLAS uses a right-handed coordinate system with its origin at the nominal interaction point (IP) in the centre of the detector and the z-axis along the beam pipe. The x-axis points from the IP to the centre of the LHC ring, and the y-axis points upwards. Cylindrical coordinates (r, ϕ) are used in the transverse plane, ϕ being the azimuthal angle around the z-axis. Pseudorapidity is defined in terms of the polar angle θ as $\eta = -\ln\tan(\theta/2)$. Angular distance is measured in units of $\Delta R \equiv \sqrt{(\Delta\eta)^2 + (\Delta\phi)^2}$. Rapidity is defined by $y = \frac{1}{2}\ln[(E + p_z)/(E - p_z)]$, where E is the energy and p_z is the longitudinal component of the momentum along the beam direction.

The inner detector (ID) reconstructs charged-particle tracks in the pseudorapidity range $|\eta| < 2.5$, using silicon pixel and microstrip subsystems within a transition radiation tracker. For $\sqrt{s} = 13$ TeV data-taking an additional innermost layer was added to the pixel tracker, the insertable B-layer [43, 44], to improve tracking performance and flavour identification of quark-initiated jets. The ID is immersed in a 2 Tesla axial magnetic field provided by the surrounding thin, superconducting solenoid.

Beyond the ID a high-granularity lead/liquid-argon (LAr) electromagnetic sampling calorimeter and a steel/scintillator-tile hadronic sampling calorimeter cover $|\eta| < 3.2$ and $|\eta| < 1.7$ respectively. In the forward regions a copper/LAr endcap calorimeter extends the hadronic coverage to $1.7 < |\eta| < 3.2$, while copper/LAr and tungsten/LAr forward calorimeters are used for electromagnetic and hadronic measurements in the $3.1 < |\eta| < 4.9$ region. The muon spectrometer (MS) surrounds the calorimeters and comprises three layers of trigger and high-precision tracking chambers spanning $|\eta| < 2.4$ and $|\eta| < 2.7$, respectively. A magnetic field is provided by a system of superconducting air-core toroidal magnets with eight coils each.

Events of interest are selected using a two-level trigger system [45] consisting of a custom hardware-based first-level (L1) trigger followed by a software-based high-level trigger (HLT). The L1 trigger reduces the 40 MHz bunch crossing rate to below 100 kHz, which the high-level trigger further reduces in order to record events to disk at about 1 kHz.

3 Data and Monte Carlo simulated event samples

This analysis exploits the full Run 2 proton–proton data set recorded by the ATLAS experiment during stable beam conditions between 2015 and 2018. The CERN Large Hadron Collider (LHC) collided protons at a centre-of-mass energy of 13 TeV, with bunch-crossing intervals of 25 ns, and the average number of interactions per crossing in data was $\langle\mu\rangle = 34$. The data set corresponds to an integrated luminosity of 139 fb^{-1}, with an uncertainty in the integrated luminosity of 1.7% [46], obtained using the LUCID-2 detector [47] for the primary luminosity measurements.

The expected contributions of SM processes and $\tilde{\chi}_1^\pm \tilde{\chi}_2^0$ SUSY signals are estimated using Monte Carlo (MC) simulation. The MC samples are used in the optimisation of event selection criteria, as well as for the estimation of systematic uncertainties on the yield prediction. The yield prediction for the dominant WZ background is improved by extracting normalisation factors from data in dedicated control regions, as discussed in Section 5.2. The estimation of the background contribution from events with one or more mis-identified or non-prompt leptons is done using a data-driven method also outlined in Section 5.2. For all other processes the MC predicted yields are used directly. The samples are produced including an ATLAS detector simulation [48] based on GEANT4 [49], or a faster simulation using a parameterised calorimeter response [50] and GEANT4 for all other detector systems. Simulated events are reconstructed in the same way as data events. Details of the MC simulation, including the generators used for the matrix element (ME) calculation and the parton shower (PS), hadronisation and underlying event modelling, the parton density function (PDF) sets used in the ME and PS, the UE tune, and the order of the cross-section calculations used for yield normalisation are given in Table 1 and briefly discussed below.

The SUSY $\tilde{\chi}_1^\pm \tilde{\chi}_2^0 \to WZ/Wh \to 3\ell$ signal samples are generated using MADGRAPH 2.6 + PYTHIA 8.2. MADSPIN [98] is used to model off-shell WZ decays. The ME–PS matching is done using the CKKW-L prescription [99, 100], with the matching scale set to one quarter of the $\widetilde{\chi}_1^\pm/\widetilde{\chi}_2^0$ mass. Samples are generated for $\widetilde{\chi}_1^\pm/\widetilde{\chi}_2^0$ masses between 100 and 850 GeV, and mass splittings Δm between 5 and 850 GeV. Only

Table 1: Monte Carlo simulation details by physics process. The table lists the event generators used for ME and PS calculations, the accuracy of the ME calculation, the PDF sets and UE parameter tunes used, and the order in α_S of cross-section calculations used for yield normalisation ("-" if the cross section is taken from MC directly).

Process	**Event generator**	**ME accuracy**	**ME PDF set**	**Cross section normalisation**
$\tilde{\chi}_1^{\pm}\tilde{\chi}_2^0$	MadGraph 2.6 [51]	0,1,2@LO[2]	NNPDF2.3lo [52]	NLO+NLL [53–58]
Diboson [59]	Sherpa 2.2.2 [60]	0, 1j@NLO + 2,3j@LO	NNPDF3.0nlo [61]	-
Triboson [59]	Sherpa 2.2.2	0j@NLO + 1,2j@LO	NNPDF3.0nlo	-
Triboson (alternative) [59]	Sherpa 2.2.1	0,1j@LO	NNPDF2.3lo	-
Z+jets [62]	Sherpa 2.2.2	0,1,2j@NLO + 3,4j@LO	NNPDF3.0nlo	NNLO[2] [63]
$t\bar{t}$ [64]	Powheg-Box 2.2 [65–67]	NLO	NNPDF3.0nlo	NNLO+NNLL[2] [68–74]
tW [75]	Powheg-Box 2.2	NLO	NNPDF3.0nlo	NLO+NNLL [76, 77]
single-t (t-channel [78], s-channel [79])	Powheg-Box 2.2	NLO	NNPDF3.0nlo	NLO [80, 81]
$t\bar{t}H$ [82]	Powheg-Box 2.2	NLO	NNPDF3.0nlo	NLO [83]
$t\bar{t}V$, tZ, tWZ	MadGraph5_aMC@NLO 2.3	NLO	NNPDF3.0nlo	-
$t\bar{t}$ ($t \to Wb\ell\ell$)	MadGraph5_aMC@NLO 2.3	LO	NNPDF2.3lo	-
$t\bar{t}$ VV, 3-top, 4-top	MadGraph5_aMC@NLO 2.2	LO	NNPDF2.3lo	-
Higgs (ggF)	Powheg-Box 2.2	NNLO+NNLL	NNPDF3.0nlo	NNNLO[2]+NLO(EWK) [83–89]
Higgs (VBF)	Powheg-Box 2.2	NLO+NNLL	NNPDF3.0nlo	NNLO+NLO(EWK) [83, 90–92]
Higgs (VH)	Powheg-Box 2.2	NLO	NNPDF3.0nlo	NNLO+NLO(EWK) [83]
Process	**PS and hadronization**	**PS PDF set**	**PS tune**	
$\tilde{\chi}_1^{\pm}\tilde{\chi}_2^0$	Pythia 8.2 [93]	NNPDF2.3lo	A14 [94]	
Diboson, Triboson, Z+jets	Sherpa 2.2.2	default Sherpa [95]	default Sherpa	
Triboson (alternative)	Sherpa 2.2.1	default Sherpa	default Sherpa	
$t\bar{t}$, tW, single-t, $t\bar{t}H$	Pythia 8.2	NNPDF2.3lo	A14	
$t\bar{t}V$, tZ, tWZ, $t\bar{t}$ ($t \to Wb\ell\ell$)	Pythia 8.2	NNPDF2.3lo	A14	
$t\bar{t}$ VV, 3-top, 4-top	Pythia 8.1	NNPDF2.3lo	A14	
Higgs (ggF, VBF, VH)	Pythia 8.2	CTEQ6L1 [96]	AZNLO [97]	

$\tilde{\chi}_1^{\pm}/\tilde{\chi}_2^0$ decays via bosons, and only leptonic boson decays are considered, with equal branching ratios for e, μ and τ leptons. For the Wh samples only Higgs-boson decays via WW, ZZ and $\tau\tau$ are generated, with cross section times branching fractions corrected to match the SM Higgs branching fractions.

The generated signal events are required to have at least two leptons for the on-shell WZ samples, and at least three leptons for the off-shell WZ and the Wh samples; hadronically decaying τ leptons are not considered in the requirement. Inclusive production cross sections are computed at next-to-leading order (NLO) plus next-to-leading-log (NLL) precision in a limit of mass-degenerate wino $\tilde{\chi}_1^{\pm}$ and $\tilde{\chi}_2^0$, light bino $\tilde{\chi}_1^0$, and with all the other sparticles assumed to be heavy and decoupled [53–58]. For production at a centre-of-mass energy of $\sqrt{s}$ = 13 TeV, the $\tilde{\chi}_1^{\pm}\tilde{\chi}_2^0$ cross section ranges between 22.67 ± 0.97 pb and 3.42 ± 0.41 fb for $\tilde{\chi}_1^{\pm}/\tilde{\chi}_2^0$ masses between 100 and 850 GeV.

Diboson, triboson and Z+jets processes are simulated with the Sherpa 2.2 generator. ME–PS matching and merging is based on Catani-Seymour dipole factorisation [95, 101, 102], using improved CKKW matching [103, 104] extended to NLO accuracy using the MEPS@NLO prescription [102–105], and including NLO virtual QCD corrections for the ME [106, 107]. The standard multiboson samples do not include Higgs-boson production. An alternative triboson sample including off-shell contributions and leptonically decaying $H \to VV$ (with $V = W$ or Z) contributions is used in the off-shell WZ selection, where W^*Z^* decays are targeted and off-shell triboson processes are non-negligible in the estimation of the SM background.

[2] leading order (LO), next-to-next-to-leading order (NNLO), next-to-next-to-next-to-leading order (NNNLO), next-to-next-to-leading-log (NNLL).

The modelling of $t\bar{t}$, single-top tW, t-channel, s-channel and $t\bar{t}H$ processes is done using Powheg-Box 2 + Pythia 8. The h_{damp} parameter[3] is set to 1.5 times the top-quark mass [108]. The samples are generated employing the five-flavour scheme (four-flavour in case of single-top t-channel), and a diagram removal scheme [109] is used in the case of tW to remove interference and overlap with $t\bar{t}$ production. Other top-quark processes ($t\bar{t}V$, tZ, tWZ, $t\bar{t}VV$, $t\bar{t}(t \to Wb\ell\ell)$, 3-top and 4-top) are modelled using MadGraph5_aMC@NLO 2 + Pythia 8. Samples of Higgs-boson production via gluon fusion, vector-boson fusion and associated production are generated using Powheg-Box 2 + Pythia 8.

All background and signal samples make use of EvtGen 1.6.0 and 1.2.0 [110] for the modelling of b and c hadrons, except those generated using Sherpa. The effect of additional interactions in the same and neighbouring bunch crossings (pileup) is included by overlaying simulated minimum-bias interactions onto each hard-scatter process. The simulation is done using Pythia 8.2 with the A3 tune [111] and the `NNPDF2.3lo` set of PDFs, and the samples are re-weighted such that the pileup distribution matches the one in data.

4 Event reconstruction and preselection

Events are selected for the on-shell WZ and the Wh selection using di-lepton triggers and for the off-shell WZ selection using single-, di- and tri-lepton triggers. The off-shell WZ selection is complemented at high $E_{\text{T}}^{\text{miss}}$ with softer lepton events selected using $E_{\text{T}}^{\text{miss}}$ triggers. The lepton triggers use various p_{T} thresholds, depending on the lepton type, quality and multiplicity. To ensure trigger efficiencies are constant in the analysis phase space, tighter quality and p_{T} requirements are applied to fully reconstructed signal leptons, as defined below. Single-electron triggers are not used, to facilitate looser signal lepton identification criteria. The number of leptons in the event that activate the trigger must be at least as many as the number of leptons required in the trigger, and electrons (muons) activating the trigger must have a fully calibrated p_{T} above 18 GeV (27.3, 14.7 or 6.5 GeV, for increasing trigger-lepton multiplicity). For events selected by a $E_{\text{T}}^{\text{miss}}$ trigger, an offline requirement of $E_{\text{T}}^{\text{miss}} > 200$ GeV is imposed to similarly ensure constant trigger efficiencies in the analysis phase space.

Events are required to have at least one reconstructed pp interaction vertex with a minimum of two associated tracks with $p_{\text{T}} > 500$ MeV. In events with multiple vertices, the primary vertex is defined as the one with the highest $\sum p_{\text{T}}^2$ of associated tracks.

The primary objects used in this analysis are electrons, muons and jets. To be considered, reconstructed objects must pass "baseline" loose identification criteria; to be selected for the analysis regions, they must also survive a second, tighter set of "signal" identification requirements. Additionally a lepton "anti-ID" requirement is defined, corresponding to leptons that pass the baseline but fail the signal criteria. These anti-ID leptons are used in the Z+jets background estimation in Section 5.2. Hadronically decaying τ leptons are not considered in the analysis, and the term "lepton" always refers to electrons or muons in this document.

Electron candidates are reconstructed from three-dimensional clustered energy deposits in the electromagnetic calorimeter (ECAL), matched to an ID track [112]. Muon candidates are reconstructed by matching MS tracks or track segments to ID tracks [113]. Electron and muon candidates are calibrated *in-situ* [112, 113], using $Z \to ee$, $Z \to \mu\mu$ and $J/\Psi \to \mu\mu$. Baseline electrons are required to have

[3] The h_{damp} parameter is a resummation damping factor and one of the parameters that controls the matching of Powheg matrix elements to the parton shower and thus effectively regulates the high-p_{T} radiation against which the $t\bar{t}$ system recoils.

$p_{\mathrm{T}} > 4.5$ GeV and fall within the acceptance of the ID ($|\eta| < 2.47$). They are further required to satisfy the calorimeter- and tracking-based "*Loose and B-layer* likelihood" identification [112]. Baseline muons must have $p_{\mathrm{T}} > 3$ GeV and $|\eta| < 2.5$, and should pass *Medium* identification criteria [113]. To suppress pileup, both baseline electrons and baseline muons are required to have a trajectory consistent with the primary vertex, i.e. $|z_0 \sin\theta| < 0.5$ mm[4].

Jet candidates are reconstructed from topological energy clusters in the electromagnetic and hadronic calorimeters [114], grouped using the anti-k_t algorithm [115, 116] with radius parameter $R = 0.4$. After subtracting the expected energy contribution from pileup following the jet area technique [117], the jet energy scale (JES) and resolution (JER) are corrected to particle level using MC simulation, and then calibrated *in-situ* using Z+jets, γ+jets and multi-jet events [118]. Baseline jets must then have $p_{\mathrm{T}} > 20$ GeV, and fall within the full calorimeter acceptance ($|\eta| < 4.5$). For jets with $|\eta| < 2.5$ a multivariate discriminant – constructed using track impact parameters, information about displaced secondary vertices, and trajectories of b- and c- hadrons inside the jet [119] – is used for the identification of b-hadron decays, referred to as b-jets. The b-tagging algorithm working point is chosen such that b-jets from simulated $t\bar{t}$ events are identified with an 85% efficiency, with rejection factors of 2.7 for charm-quark jets and 25 for light-quark and gluon jets.

Photon candidates are reconstructed from energy clusters in the ECAL provided they have no matched track, or have one or more matched tracks consistent with photon conversion origin. Baseline photons, while not used in the signal regions, are included in the calculation of missing transverse momentum, and used in SM background estimation validation. They are required to have $p_{\mathrm{T}} > 25$ GeV, fall inside the ECAL strip detector acceptance ($|\eta| < 2.37$), but outside the ECAL transition region ($|\eta| \in [1.37, 1.52]$). Candidates must also satisfy *Tight* identification criteria [112].

Ambiguities may exist between reconstructed objects. To prevent single detector signatures from being identified as multiple objects, the following overlap removal procedure is applied to baseline leptons and jets. First, all electrons sharing an ID track with a muon are discarded to remove bremsstrahlung from muons followed by a photon conversion. Second, all jets separated from remaining electrons by less than $\Delta R = 0.2$ are removed. Also all jets nearby a muon within $\Delta R = 0.4$ and associated with less than three tracks with $p_{\mathrm{T}} \geq 500$ MeV are removed. Finally, electrons or muons separated from surviving jets by less than $\Delta R = 0.4$ are discarded to reject non-prompt leptons from decays of b- and c-hadrons.

The missing transverse momentum is defined as the negative vector sum of the transverse momenta of all baseline objects (electrons, muons, jets, and photons) and an additional soft term [120]. The soft term is constructed from all tracks that pass basic quality requirements and are associated with the primary vertex, but are not associated with any baseline object. In this way, the $\mathbf{p}_{\mathrm{T}}^{\mathrm{miss}}$ is adjusted for the calibration of the contributing objects, while maintaining robustness against pileup [121]. Additionally an "object-based $E_{\mathrm{T}}^{\mathrm{miss}}$-significance" [122], is defined to test the hypothesis that the total transverse momentum carried by non-interacting particles is equal to zero against the hypothesis that it is different from zero. It quantifies the degree to which the measured $E_{\mathrm{T}}^{\mathrm{miss}}$ is inconsistent with originating purely from fluctuations and mismeasurements. A large value indicates that the $E_{\mathrm{T}}^{\mathrm{miss}}$ genuinely originates from non-interacting particles. In this analysis, the object-based $E_{\mathrm{T}}^{\mathrm{miss}}$ significance characterises the $E_{\mathrm{T}}^{\mathrm{miss}}$ based on the p_{T}, p_{T} resolution and ϕ resolution of all objects in the event and is defined as $\sqrt{|\mathbf{p}_{\mathrm{T}}^{\mathrm{miss}}|^2/(\sigma_{\mathrm{L}}^2(1-\rho_{\mathrm{LT}}^2))}$. In this definition, σ_{L} is the total expected longitudinal resolution of all objects in the event as a function of the p_{T} of each object.

[4] The transverse impact parameter, d_0, is defined as the distance of closest approach in the transverse plane between a track and the beam-line. The longitudinal impact parameter, z_0, corresponds to the z-coordinate distance between the point along the track at which the transverse impact parameter is defined and the primary vertex.

Likewise, ρ_{LT} is the correlation factor between all longitudinal and transverse object resolutions. The resolution on the $E_{\mathrm{T}}^{\mathrm{miss}}$ soft term is taken to be a fixed 8.9 GeV in each of the transverse coordinates. Each jet resolution is further modified by the probability that the jet is a pile-up jet mistakenly tagged as being from the hard scatter interaction, parameterised in p_{T}, η and JVT.

To ensure high quality object measurement and selection purity for the analysis regions, leptons and jets must pass additional tighter "signal" criteria and isolation requirements to be selected. Signal electrons must satisfy *Medium* identification criteria [112]. All signal leptons are then required to be compatible with originating from the primary vertex; the significance of the transverse impact parameter, $\sigma(d_0)$, should satisfy $|d_0/\sigma(d_0)| < 5$ (3) for electrons (muons).

Isolation requirements are applied to suppress contributions from conversions, semi-leptonic decays of heavy-flavour hadrons, or hadrons and jets wrongly identified as leptons, collectively referred as fake or non-prompt (FNP) leptons. The criteria rely on isolation energy variables calculated by $\sum p_{\mathrm{T}}$ of tracks or calo-clusters within a certain size of cone around the lepton candidate. The isolation working points used in this analysis are based on those described in Refs. [112] and [113], including updates to improve the performance under the increased pileup conditions encountered during 2017 and 2018 data taking. The choice of isolation working points is optimised per selection region and per lepton-flavour to account for different levels of contribution from the FNP lepton background. The *FCTight* working point is used for electrons and muons in the on-shell *WZ* and *Wh* selections, while the looser working points *Gradient* and *FCLoose* are employed for electrons and muons respectively in the off-shell *WZ* selection, to maintain a reasonable efficiency down to low p_{T}.

To further suppress FNP lepton backgrounds in the off-shell *WZ* selection, a dedicated multi-variate discriminant "non-prompt lepton BDT" [41] is used to tighten the requirements on the lepton with the lowest p_{T} (which is commonly also the most FNP-like lepton of the three), after selecting exactly three baseline leptons in the event. The discriminant uses eight input variables including the isolation information, combined lepton and track quantities, and the *b*-jet likeliness calculated based on the energy deposits and tracks in a cone around the lepton using the `DL1mu` or `RNNIP` algorithms [123]. The non-prompt lepton BDT selection is designed to maintain 70% – 90% efficiency for real leptons, with a rejection factor of 3-4 for FNP leptons passing the isolation selection. Figure 2 shows the combined signal lepton selection efficiency (including the reconstruction, identification, isolation, vertex association and non-prompt BDT selection) for the leptons from signal events, as well as the differential probability for a Z+jets event to be accompanied by a FNP lepton passing the signal lepton selection criteria.

Signal jets are selected within $|\eta| < 2.8$, and must pass *Loose* quality criteria to reject contamination from non-collision backgrounds or noise bursts [124]. In order to suppress jets originating from pileup, signal jet candidates with $p_{\mathrm{T}} < 120$ GeV and $|\eta| < 2.5$ (within the ID acceptance) are further required to satisfy the *Medium* working point of the track-based jet vertex tagger (JVT) [117, 125].

To account for small efficiency differences between simulated samples and data, simulated samples are corrected with scale factors covering lepton reconstruction, identification, isolation and trigger efficiencies, as well as jet pileup rejection and flavour tagging efficiencies.

A common preselection for all search regions is applied requiring exactly three signal leptons. Events are also required to have exactly three baseline leptons. This additional baseline requirement ensures orthogonality with other ATLAS SUSY analyses [31, 126, 127] and facilitates statistical combinations; it also simplifies the FNP lepton background estimation. Muons in $2.5 < |\eta| < 2.7$ are included in this count if they pass all other baseline muon criteria.

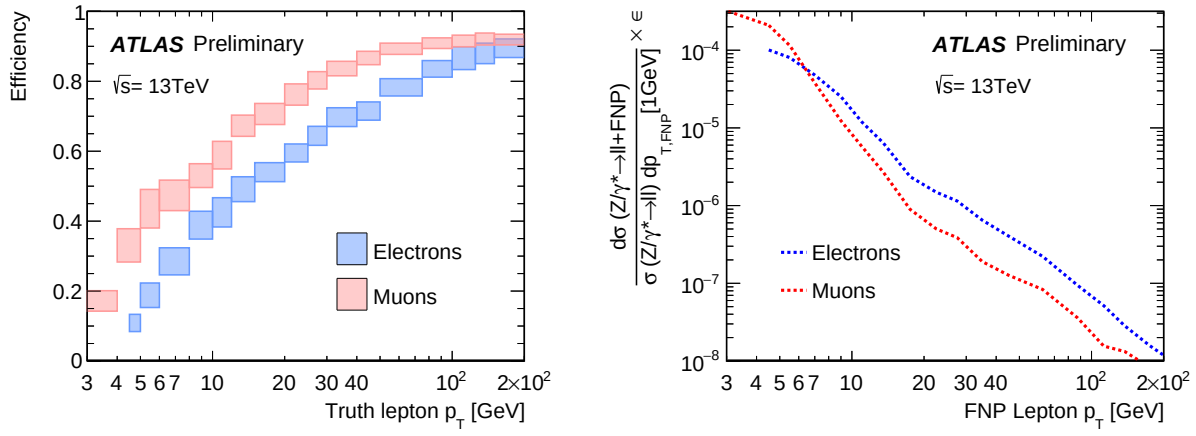

Figure 2: The left panel shows the combined lepton selection efficiencies for the signal electron/muon requirements applied for the lowest-p_{T} lepton after selecting three baseline leptons in the off-shell WZ selection. The efficiencies are calculated using simulated samples of $\widetilde{\chi}_1^{\pm}/\widetilde{\chi}_2^0$ decays and shown as a function of the truth lepton p_{T}. The associated uncertainties represent the range of efficiencies observed across all signal samples used for the given p_{T} bin. The right panel illustrates the differential probability for a Z+jets event to be accompanied by a FNP lepton passing the signal lepton criteria, as a function of the FNP lepton p_{T}. This probability is measured using data events in a region with at least two signal leptons, with the other processes subtracted using the MC samples.

5 Analysis strategy

The on-shell WZ, off-shell WZ, and Wh selections of this analysis, while targeting different simplified model scenarios, all consider final states with exactly three leptons, possible ISR jets, and $E_{\mathrm{T}}^{\mathrm{miss}}$. Therefore, a common approach is used throughout most steps of the analyses. The on-shell WZ, off-shell WZ, and Wh selections are optimised independently and labelled as "`WZ`", "`offWZ`", or "`Wh`", respectively.

This section describes the general analysis strategy, introducing the common parts of the search region definitions (Section 5.1), the background estimation (Section 5.2), and the uncertainty treatment (Section 5.3). The statistical methods used are outlined in Section 5.4. Further details specific to either the on-shell WZ and Wh selections, or the off-shell WZ selection, are then discussed in dedicated Sections 6 and 7.

5.1 Search regions

Event selections enriched in signal (signal regions or SRs), are designed independently for the three targeted models, i.e. for the on-shell WZ, off-shell WZ or Wh selections, and are collected in SR groups $\mathrm{SR}^{\mathtt{WZ}}$, $\mathrm{SR}^{\mathtt{offWZ}}$, and $\mathrm{SR}^{\mathtt{Wh}}$, respectively, based on the presence of a $Z^{(*)}$- or Higgs-boson candidate.

Two leptons are required to be consistent with the decay of a $Z^{(*)}$ or Higgs boson, while the third is required to match the decay of a $W^{(*)}$ boson. Leptons are associated to the $Z^{(*)}$- or Higgs-boson candidate by selecting a same-flavour opposite-charge sign (SFOS) lepton pair in the event, and the remaining lepton is associated to the $W^{(*)}$ boson (labelled W lepton or ℓ_W). If more than one SFOS lepton pair is present in the event, in $\mathrm{SR}^{\mathtt{WZ}}$ the pair with invariant mass, $m_{\ell\ell}$, nearest the Z-boson mass, m_Z, is selected to be assigned to the Z-boson candidate ($m_{\ell\ell}$ assignment); while in $\mathrm{SR}^{\mathtt{offWZ}}$ the pair with the smallest invariant mass, $m_{\ell\ell}^{\mathrm{min}}$, is selected to be assigned to the Z^*-boson candidate ($m_{\ell\ell}^{\mathrm{min}}$ assignment). The $\mathrm{SR}^{\mathtt{WZ}}$ regions are optimised for on-shell WZ signals with mass splittings $\Delta m \gtrsim m_Z$ and require $m_{\ell\ell} \in [75, 105]$ GeV; while the $\mathrm{SR}^{\mathtt{offWZ}}$

regions target off-shell WZ signals with mass splittings $\Delta m < m_Z$, and veto on-shell Z-boson candidates by requiring $m_{\ell\ell}^{\text{min}} \leq m_{\ell\ell} < 75$ GeV. SR^{Wh} consists of two parts: the SFOS regions ($\text{SR}^{\text{Wh}}_{\text{SFOS}}$) with at least one SFOS lepton pair and a Z-veto ($m_{\ell\ell} \notin [75, 105]$ GeV) are optimised for the Wh-mediated model, but additionally benefit the search for WZ-mediated model signals with mass splittings $\Delta m \lesssim m_Z$; and the different-flavour opposite-charge sign (DFOS) regions ($\text{SR}^{\text{Wh}}_{\text{DFOS}}$), where events without SFOS lepton pairs are selected, target the Wh-mediated model.

Full event reconstruction is performed subsequently for regions with at least one SFOS pair. The transverse mass, m_{T}, for the W boson is constructed using the W lepton and the $E_{\text{T}}^{\text{miss}}$, and assuming the SM WZ event hypothesis: $m_{\text{T}} = \sqrt{2p_{\text{T}}^{\ell_{\text{W}}} E_{\text{T}}^{\text{miss}}(1 - \cos(\Delta\phi))}$, where $\Delta\phi$ is the separation in the transverse plane between the lepton and the $E_{\text{T}}^{\text{miss}}$. This exploits the difference between SM WZ, which has a Jacobian peak with a sharp cut-off at $m_{\text{T}} \sim m_W$ (the W-boson mass), and the targeted signals, which have relatively flat distributions. Further, events are separated by jet multiplicity, creating jet-veto ($n_{\text{jets}} = 0$) and jet-inclusive ($n_{\text{jets}} > 0$) SRs.

Finally, in SR^{offWZ}, the choice for $m_{\ell\ell}^{\text{min}}$ assignment is motivated by the presence of a kinematic edge in the signal distribution for this variable, allowing for improved signal over background discrimination for these regions. Other kinematic variables used in SR^{offWZ} are also constructed based on $m_{\ell\ell}^{\text{min}}$ assignment.

Each SR group consists of multiple bins, segmented by a few key discriminating variables. The SR^{WZ} ($\text{SR}^{\text{Wh}}_{\text{SFOS}}$) group is divided into 20 (19) bins based on $E_{\text{T}}^{\text{miss}}$, m_{T} and H_{T}, with the latter defined as scalar sum of the transverse momenta of jets with $p_{\text{T}} > 20$ GeV. The two $\text{SR}^{\text{Wh}}_{\text{DFOS}}$ bins are defined by different jet multiplicity. Finally, SR^{offWZ} has 31 bins based on $m_{\ell\ell}^{\text{min}}$, $E_{\text{T}}^{\text{miss}}$, and jet multiplicity. The bins within each SR group are mutually disjoint, and are statistically combined when calculating the constraints on the target models. A more detailed configuration of the fit is given after the discussion of the background estimation procedure in Section 5.2. Additionally, discovery-oriented inclusive SRs are designed by grouping sets of adjoining nominal-SR bins in order to facilitate quantifying the size of data excesses in a model-independent manner. The definitions of the nominal SRs are further detailed per selection in subsequent Sections 6.1 (SR^{WZ} and SR^{Wh}) and 7.1 (SR^{offWZ}), and the inclusive-SR definitions are discussed in Section 8.1.

5.2 Background estimation

The dominant SM background in most of the SRs in this analysis is from fully-leptonically decaying SM WZ events, followed by $t\bar{t}$ and Z+jets processes associated with at least one FNP lepton. In $\text{SR}^{\text{Wh}}_{\text{DFOS}}$, SM Higgs, triboson and $t\bar{t}$ production are the dominating processes.

A partially data-driven method is used for the estimation of the WZ background, which produces three real and prompt leptons. The background is predicted using MC simulation samples and normalised to data in dedicated control regions (CRs). This normalisation improves the estimation in the phase-space of the selections, and constrains the systematic uncertainties. The CRs are designed to be orthogonal and similar to the SRs, whilst also having little signal contamination; this is achieved by taking the SR definitions and inverting some of the selection criteria. Dedicated validation regions (VRs) are defined kinematically in between the CRs and SRs, and assess the quality of the background estimation and its extrapolation to the SRs. The final estimation of the yields and uncertainties is performed with a simultaneous fit to the CRs and SRs, as discussed in Section 5.4.

The $t\bar{t}$ background is predicted using MC simulation samples and validated in VRs. It is dominated by di-leptonic decays with an additional lepton from a b- or c-hadron decay. As the MC modelling is found to be of good quality, no additional corrections are applied to the MC.

The $(Z/\gamma^* \to \ell\ell)$ + (jets/γ) background has two prompt leptons and one FNP lepton from jets or photons. "Z+jets" will be used in the rest of this document to refer to this set of processes. As there are no invisible particles in these processes at tree level, the observed $E_{\mathrm{T}}^{\mathrm{miss}}$ is mostly due to mis-measured leptons and/or jets, or due to the $E_{\mathrm{T}}^{\mathrm{miss}}$ soft term. The FNP leptons originate from a mix of sources, including light-flavour jets faking leptons, electrons from photon conversion, and non-prompt leptons from b- or c-hadron decays. Such FNP leptons often arise from instrumental effects, hadronisation, and the underlying event, all of which are challenging to reliably model in simulation. Therefore a data-driven method, referred to as the Fake Factor method [128, 129], is used to estimate the Z+jets background. The fake factor (FF) is defined as the ratio of the probability for a given lepton candidate to pass the signal lepton requirements to that to fulfil the anti-ID requirements. This is measured using data in a control region, `CRFF`, designed to target Z+jets events with FNP leptons whose sources are representative of those expected in the SRs. Exactly three baseline leptons and at least one SFOS lepton pair are required in `CRFF`. The Z-boson candidate in the event is identified as the SFOS pair yielding the invariant mass closest to the Z-boson mass, and the remaining lepton is tagged as the FNP lepton candidate. The two leptons from the Z-boson candidate must activate the di-lepton trigger to ensure there is no selection bias from FNP leptons. The Z+jets prediction in a given region is obtained by applying the FFs to the events in its corresponding "anti-ID region". This region is defined requiring the same selection criteria as for the nominal region with three signal leptons, except that at least one of the leptons is anti-ID instead of signal. Each event in the anti-ID region is scaled by a weight based on the FF assigned to each anti-ID lepton in the region. The FFs are derived separately per lepton flavour and are parametrised as a function of lepton p_{T} and lepton η or $E_{\mathrm{T}}^{\mathrm{miss}}$ in the event, depending on the analysis selection. In both the FF measurement and the FF application procedure, contributions from processes other than Z+jets are subtracted using MC simulated samples. Rare SM processes, including multiboson and Higgs-boson production, top-pair production in association with a boson, and single-top production, are estimated from MC simulation in all analysis regions.

While sharing a common approach, due to the different primary target phase-space with different relative background composition and importance, the estimation and validation procedures for the main SM backgrounds were optimised independently for the different selections. Details are given in Section 6.2 ($\mathrm{SR}^{\mathtt{WZ}}$ and $\mathrm{SR}^{\mathtt{Wh}}$) and Section 7.2 ($\mathrm{SR}^{\mathtt{offWZ}}$).

5.3 Systematic uncertainties

The analysis considers uncertainties on the predicted yields of signal or background processes due to instrumental systematic uncertainties as well as statistical uncertainties and theoretical systematic uncertainties of the MC simulated samples. Uncertainties are assigned on the yield in each region, except for WZ processes constrained in CRs, in which case they are assigned on the acceptance in each SR relative to that in the CR. The uncertainty treatment is largely common for the on-shell WZ, Wh and off-shell WZ selections; exceptions are discussed in Sections 6.2 ($\mathrm{SR}^{\mathtt{WZ}}$ and $\mathrm{SR}^{\mathtt{Wh}}$) and 7.2 ($\mathrm{SR}^{\mathtt{offWZ}}$).

The dominant instrumental uncertainties are the jet energy scale (JES) and resolution (JER). The jet uncertainties are derived as a function of p_{T} and η of the jet, as well as of the pileup conditions and the jet flavour composition of the selected jet sample. They are determined using a combination of simulated samples and studies in data, such as measurements of the jet p_{T} balance in dijet, Z+jet and γ+jet events [118]. Another significant instrumental uncertainty is that on the modelling of $E_{\mathrm{T}}^{\mathrm{miss}}$, evaluated by propagating the uncertainties on the energy and momentum scale of each of the objects entering the calculation, as well as the uncertainties on the $E_{\mathrm{T}}^{\mathrm{miss}}$ soft term resolution and scale [120]. Other instrumental uncertainties concerning the efficiency of trigger selection, flavour-tagging and JVT, as well as reconstruction, ID,

impact parameter selection and isolation for leptons, are found to have minor impact. Each experimental uncertainty is treated as fully correlated across analysis regions and physics processes considered.

For the processes estimated using the MC simulation, the predicted yield is also affected by different sources of theoretical modelling uncertainty. All theoretical uncertainties are treated as fully correlated across analysis regions, except those related to MC statistics. The uncertainties for the dominant background processes, WZ, ZZ, and $t\bar{t}$, are derived using MC simulation samples. For the WZ background, which is normalised to data in CRs, these uncertainties are implemented as transfer factor uncertainties and propagated to all VRs and SRs. The uncertainties related to the choice of QCD renormalisation and factorisation scales are assessed by varying the corresponding generator parameters up and down by a factor of two around their nominal values. The renormalisation and factorisation scales are varied both independently and fully correlated, but the method does not allow for anti-correlated variations; each of these six variations is treated as correlated across regions. For the WZ and ZZ samples, the uncertainties due to the resummation and matching scales between ME and PS as well as the PS recoil scheme are evaluated by varying the corresponding parameters in Sherpa. For $t\bar{t}$, modelling uncertainties at ME and PS level are measured by comparing the predictions of nominal and alternative generators, considering Powheg-Box versus MadGraph5_aMC@NLO and Pythia 8 versus Herwig 7 [130, 131], respectively. Uncertainties in the $t\bar{t}$ prediction due to ISR and final-state radiation (FSR) uncertainties are evaluated varying the relevant generator parameters. The uncertainties associated with the choice of PDF set, NNPDF [52, 61], and the uncertainty in the strong coupling constant, α_s, are also considered for the major backgrounds. For minor backgrounds, conservative flat uncertainties in the cross section are assumed. Uncertainties of 13%, 12%, 10% and 20% are applied for $t\bar{t}\,W$, $t\bar{t}\,Z$, $t\bar{t}\,H$ and triboson, respectively [83]; for all other rare top samples an uncertainty of 50% is applied.

The data-driven Z+jets estimation is subject to the statistical uncertainty due to the limited data sample size in CRFF or in the anti-ID regions used in the FF application, the uncertainty due to varying choice of parametrisation, and the uncertainty on the subtraction of non-Z+jets processes. The uncertainties are evaluated by considering the variations in the FF and propagating the effects to the estimated yields. Different prescriptions are applied for the estimation in the off-shell WZ selection compared to on-shell WZ and Wh selections, reflecting the higher presence of Z+jets in $\mathrm{SR}^{\mathtt{offWZ}}$. Details are included in Sections 6.2 and 7.2.

Uncertainties on the expected yields for SUSY signals are estimated by varying by a factor of two the MadGraph5_aMC@NLO parameters corresponding to the renormalisation, factorisation and CKKW-L matching scales, as well as the Pythia8 shower tune parameters. The overall uncertainties on the signal acceptance range from 5% to 20% depending on the analysis region. Uncertainties are smallest in jet-veto regions and slightly larger for higher $E_{\mathrm{T}}^{\mathrm{miss}}$ and jet-inclusive regions.

5.4 Statistical analysis

Final background estimates are obtained by performing a profile log-likelihood fit [132], implemented in the HistFitter [133] framework, simultaneously on all CRs and SRs relevant to a given interpretation. The statistical and systematic uncertainties are implemented as nuisance parameters in the likelihood; Poisson constraints are used to estimate the uncertainties arising from limited MC statistics or limited statistics in the data-driven Z+jets estimation, whilst Gaussian constraints are used for experimental and theoretical systematic uncertainties. Neither the VRs, which solely serve to validate the background estimation in the SRs, nor the CRs used for data-driven Z+jets estimation, are included in any of the fits.

Three types of fit configurations are used to derive the results.

- A "*background-only fit*" is performed considering only the CRs and assuming no signal presence. The normalisation of the WZ background is left floating and constrained by the fit using the WZ CRs. The normalisation factors and nuisance parameters are adjusted by maximising the likelihood. The background prediction as obtained from this fit is compared to data in the VRs to assess the quality of the background modelling.
- A "*discovery fit*" is performed to derive model-independent constraints, setting upper limits on the new physics cross section. The fit considers the target single-bin SR and the associated CRs, constraining the backgrounds following the same method as in the background-only fit. A signal contribution is allowed only in the SR, and a non-negative signal strength parameter assuming generic beyond-the-SM (BSM) signals is derived.
- An "*exclusion fit*" is performed to set exclusion limits on the target models. The backgrounds are again constrained following the same method as in the background-only fit, and the signal contribution to each region participating in the fit is taken into account according to the model predictions.

For each discovery or exclusion fit, the compatibility of the observed data with the background-only or signal-plus-background hypotheses is checked using the CL_s prescription [134], and limits on the cross section are set at 95% confidence level (CL).

Following the independent optimisation of the CRs and SRs, the simultaneous fits are performed separately for the different selections: once for the on-shell WZ and Wh selections combined, and once for the off-shell WZ selection. The results are presented in Section 8.

6 On-shell WZ and Wh selections

The following subsections discuss the implementation and optimisation specific to the on-shell WZ and Wh selections.

6.1 Search regions

The $\mathrm{SR}^{\mathrm{WZ}}$ and $\mathrm{SR}^{\mathrm{Wh}}$ selections as introduced in Section 5.1 are further refined, taking into consideration differences in signal and background kinematics and composition. Driven by the p_{T} thresholds of the di-lepton triggers used in this selection, the leading and sub-leading leptons in the event must satisfy $p_{\mathrm{T}} > 25, 20$ GeV, while the third lepton must satisfy $p_{\mathrm{T}} > 10$ GeV. To reduce SM backgrounds with little to no real $E_{\mathrm{T}}^{\mathrm{miss}}$, events are required to have $E_{\mathrm{T}}^{\mathrm{miss}} > 50$ GeV. To suppress the contribution of $t\bar{t}$ events and single-boson production in association with a $t\bar{t}$ pair, events with at least one b-jet are rejected.

To reduce the contribution from processes with low-mass dilepton resonances, events are vetoed if they contain a SFOS lepton pair with an invariant mass below 12 GeV. Additionally, in events with a SFOS pair, the three-lepton invariant mass $m_{3\ell}$ is required to be inconsistent with the mass of a Z boson, $|m_{3\ell} - m_Z| > 15$ GeV, in order to suppress contributions from asymmetric photon conversions from the Z+jets process with $Z \to \ell\ell\gamma^{(*)}$and $\gamma^{(*)} \to \ell\ell$, where one of the leptons is out of acceptance. A summary of the preselection criteria is presented in Table 2.

Table 2: Summary of the preselection criteria applied in all regions of the on-shell WZ and Wh selections. In rows where only one value is given it applies to all regions. "-" indicates no requirement is applied for a given variable/region.

	Preselection requirements			
Variable	$\mathrm{SR}^{\mathrm{WZ}}$	$\mathrm{SR}^{\mathrm{Wh}}_{\mathrm{SFOS}}$	$\mathrm{SR}^{\mathrm{Wh}}_{\mathrm{DFOS}}$	$\mathrm{CR}^{\mathrm{WZ}}/\mathrm{VR}^{\mathrm{WZ}}$
$n_{\mathrm{lep}}^{\mathrm{baseline}}$, $n_{\mathrm{lep}}^{\mathrm{signal}}$		$= 3$		$= 3$
trigger		di-lepton		di-lepton
$p_{\mathrm{T}}^{\ell_1}$, $p_{\mathrm{T}}^{\ell_2}$, $p_{\mathrm{T}}^{\ell_3}$ [GeV]		$> 25, 20, 10$		$> 25, 20, 10$
$E_{\mathrm{T}}^{\mathrm{miss}}$ [GeV]		> 50		-
$n_{\mathrm{b-jets}}$		$= 0$		-
resonance veto $m_{\ell\ell}$ [GeV]		> 12		-
n_{SFOS}	≥ 1	≥ 1	$= 0$	-
$m_{\ell\ell}$ [GeV]	$\in [75, 105]$	$\notin [75, 105]$	$\notin [75, 105]$	-
$\lvert m_{3\ell} - m_Z \rvert$ [GeV]	> 15	> 15	-	-

The $\mathrm{SR}^{\mathrm{WZ}}$ and $\mathrm{SR}^{\mathrm{Wh}}_{\mathrm{SFOS}}$ groups are divided into three bins of SFOS lepton pair invariant mass, $m_{\ell\ell}$, in order to separate processes that include a Z boson in the decay chain from processes where a Higgs boson is involved. One of the $m_{\ell\ell}$ bins is defined below the Z-boson mass ($m_{\ell\ell} \leq 75$ GeV) and the second one contains the events with $m_{\ell\ell}$ above the Z-boson mass ($m_{\ell\ell} \geq 105$ GeV). The third one is defined as the Z-boson mass window ($m_{\ell\ell} \in [75, 105]$ GeV), and is expected to contain a larger irreducible SM background contribution than the other bins.

Each $m_{\ell\ell}$ bin is further divided into m_{T} and $E_{\mathrm{T}}^{\mathrm{miss}}$ bins, which enhances the sensitivity to various Δm scenarios. The m_{T} distribution is steeply falling around the W-boson mass, and facilitates discrimination against the background from WZ production. Three m_{T} bins, $m_{\mathrm{T}} < 100$, $100 \leq m_{\mathrm{T}} \leq 160$, and $m_{\mathrm{T}} > 160$ GeV, are defined to separate processes with and without a leptonic W-boson decay. The lower and upper bounds on the $E_{\mathrm{T}}^{\mathrm{miss}}$ bins vary with the $m_{\ell\ell}$ and m_{T} thresholds. SM background contribution is expected to be higher in low m_{T} and $E_{\mathrm{T}}^{\mathrm{miss}}$ bins, while the signal populates different m_{T} and $E_{\mathrm{T}}^{\mathrm{miss}}$ bins, depending on the mass splitting. Signals with smaller Δm tend to have more events in the lower $E_{\mathrm{T}}^{\mathrm{miss}}$ and m_{T} range, shifting to higher $E_{\mathrm{T}}^{\mathrm{miss}}$ and m_{T} bins as the mass difference increases.

The ISR topology is exploited further in the jet-inclusive regions of $\mathrm{SR}^{\mathrm{WZ}}$ and $\mathrm{SR}^{\mathrm{Wh}}$ by categorising the events with at least one jet according to their H_{T}. At higher H_{T}, signals with mass splitting $\Delta m \approx m_{\mathrm{Z}}$ tend to have more events at high values of $E_{\mathrm{T}}^{\mathrm{miss}}$ and m_{T} than the SM background, due to the recoil against ISR jets. In the high H_{T} ($H_{\mathrm{T}} > 200$ GeV) regions, softer lepton p_{T} spectra are expected for the signal due to the presence of a massive $\tilde{\chi}_1^0$, which carries most of the transverse momenta of the boosted $\widetilde{\chi}_1^{\pm}\widetilde{\chi}_2^0$ system. Therefore $H_{\mathrm{T}}^{\mathrm{lep}}$, the scalar p_{T} sum of the three selected leptons, is required to be less than 350 GeV. The H_{T} categorisation is applied in regions with $m_{\ell\ell} < 105$ GeV. Finally, in the high-mass off-peak region ($m_{\ell\ell} \geq 105$ GeV), only jet-veto events are considered. The full set of 20 $\mathrm{SR}^{\mathrm{WZ}}$ and 19 $\mathrm{SR}^{\mathrm{Wh}}_{\mathrm{SFOS}}$ signal regions is summarised in Tables 3 and 4.

In the $\mathrm{SR}^{\mathrm{Wh}}_{\mathrm{DFOS}}$ regions events are required to have one same-flavour same-charge sign (SFSS) lepton pair as well a third lepton which is a different flavour and opposite sign to the SFSS pair, and is referred to as the DF lepton. In order to minimise contributions from the $t\bar{t}$ background, only events with low jet multiplicity ($n_{\mathrm{jets}} < 3$) are kept. These are then further split into two SR bins, one with $n_{\mathrm{jets}} = 0$ ($\mathrm{SR}^{\mathrm{Wh}}_{\mathrm{DFOS}}$-1) and the other satisfying $n_{\mathrm{jets}} \in [1, 2]$ ($\mathrm{SR}^{\mathrm{Wh}}_{\mathrm{DFOS}}$-2). Due to the presence of the $\widetilde{\chi}_1^0$, signals tend

Table 3: Summary of the selection criteria for SRs targeting events with at least one SFOS lepton pair and $m_{\ell\ell} \in [75, 105]$ GeV, for the on-shell WZ search regions. Region selections are binned by m_{T} (rows) and $E_{\mathrm{T}}^{\mathrm{miss}}$ for the two sets of regions, where each set has different n_{jets}, and H_{T} requirements. $\mathtt{SR}^{\mathtt{WZ}}$ preselection criteria are applied (Table 2).

Selection requirements				
$n_{\mathrm{jets}} = 0$				
m_{T} [GeV]	$E_{\mathrm{T}}^{\mathrm{miss}}$ [GeV]			
[100,160]	$\mathtt{SR}^{\mathtt{WZ}}$-1: [50,100]	$\mathtt{SR}^{\mathtt{WZ}}$-2: [100,150]	$\mathtt{SR}^{\mathtt{WZ}}$-3: [150,200]	$\mathtt{SR}^{\mathtt{WZ}}$-4: > 200
> 160	$\mathtt{SR}^{\mathtt{WZ}}$-5: [50,150]	$\mathtt{SR}^{\mathtt{WZ}}$-6: [150,200]	$\mathtt{SR}^{\mathtt{WZ}}$-7: [200,350]	$\mathtt{SR}^{\mathtt{WZ}}$-8: > 350
$n_{\mathrm{jets}} > 0$, $H_{\mathrm{T}} < 200$ GeV				
m_{T} [GeV]	$E_{\mathrm{T}}^{\mathrm{miss}}$ [GeV]			
[100,160]	$\mathtt{SR}^{\mathtt{WZ}}$-9: [100,150]	$\mathtt{SR}^{\mathtt{WZ}}$-10: [150,250]	$\mathtt{SR}^{\mathtt{WZ}}$-11: [250,300]	$\mathtt{SR}^{\mathtt{WZ}}$-12: > 300
> 160	$\mathtt{SR}^{\mathtt{WZ}}$-13: [50,150]	$\mathtt{SR}^{\mathtt{WZ}}$-14: [150,250]	$\mathtt{SR}^{\mathtt{WZ}}$-15: [250,400]	$\mathtt{SR}^{\mathtt{WZ}}$-16: > 400
$n_{\mathrm{jets}} > 0$, $H_{\mathrm{T}} > 200$ GeV, $H_{\mathrm{T}}^{\mathrm{lep}} < 350$ GeV				
m_{T} [GeV]	$E_{\mathrm{T}}^{\mathrm{miss}}$ [GeV]			
> 100	$\mathtt{SR}^{\mathtt{WZ}}$-17: [150,200]	$\mathtt{SR}^{\mathtt{WZ}}$-18: [200,300]	$\mathtt{SR}^{\mathtt{WZ}}$-19: [300,400]	$\mathtt{SR}^{\mathtt{WZ}}$-20: > 400

Table 4: Summary of the selection criteria for SRs targeting events with at least one SFOS lepton pair and $m_{\ell\ell} \notin [75, 105]$ GeV, for the Wh search regions. Region selections binned by m_{T} (rows) and $E_{\mathrm{T}}^{\mathrm{miss}}$ for the three sets of regions, where each set has different $m_{\ell\ell}$, n_{jets}, and H_{T} requirements. $\mathtt{SR}_{\mathtt{SFOS}}^{\mathtt{Wh}}$ preselection criteria are applied (Table 2).

Selection requirements				
$m_{\ell\ell} \leq 75$ GeV, $n_{\mathrm{jets}} = 0$				
m_{T} [GeV]	$E_{\mathrm{T}}^{\mathrm{miss}}$ [GeV]			
[0,100]	$\mathtt{SR}_{\mathtt{SFOS}}^{\mathtt{Wh}}$-1: [50,100]	$\mathtt{SR}_{\mathtt{SFOS}}^{\mathtt{Wh}}$-2: [100,150]	$\mathtt{SR}_{\mathtt{SFOS}}^{\mathtt{Wh}}$-3 > 150	
[100,160]	$\mathtt{SR}_{\mathtt{SFOS}}^{\mathtt{Wh}}$-4: [50,100]		$\mathtt{SR}_{\mathtt{SFOS}}^{\mathtt{Wh}}$-5: > 100	
> 160	$\mathtt{SR}_{\mathtt{SFOS}}^{\mathtt{Wh}}$-6: [50,100]		$\mathtt{SR}_{\mathtt{SFOS}}^{\mathtt{Wh}}$-7: > 100	
$m_{\ell\ell} \leq 75$ GeV, $n_{\mathrm{jets}} > 0$, $H_{\mathrm{T}} < 200$				
m_{T} [GeV]	$E_{\mathrm{T}}^{\mathrm{miss}}$ [GeV]			
[0,50]	$\mathtt{SR}_{\mathtt{SFOS}}^{\mathtt{Wh}}$-8: [50,100]			
[50,100]	$\mathtt{SR}_{\mathtt{SFOS}}^{\mathtt{Wh}}$-9: [50,100]			
[0,100]	$\mathtt{SR}_{\mathtt{SFOS}}^{\mathtt{Wh}}$-10: [100,150]		$\mathtt{SR}_{\mathtt{SFOS}}^{\mathtt{Wh}}$-11: > 150	
[100,160]	$\mathtt{SR}_{\mathtt{SFOS}}^{\mathtt{Wh}}$-12: [50,100]	$\mathtt{SR}_{\mathtt{SFOS}}^{\mathtt{Wh}}$-13: [100,150]	$\mathtt{SR}_{\mathtt{SFOS}}^{\mathtt{Wh}}$-14: > 150	
> 160	$\mathtt{SR}_{\mathtt{SFOS}}^{\mathtt{Wh}}$-15: [50,150]		$\mathtt{SR}_{\mathtt{SFOS}}^{\mathtt{Wh}}$-16: > 150	
$m_{\ell\ell} \geq 105$ GeV, $n_{\mathrm{jets}} = 0$				
m_{T} [GeV]	$E_{\mathrm{T}}^{\mathrm{miss}}$ [GeV]			
> 100	$\mathtt{SR}_{\mathtt{SFOS}}^{\mathtt{Wh}}$-17: [50,100]	$\mathtt{SR}_{\mathtt{SFOS}}^{\mathtt{Wh}}$-18: [100,200]	$\mathtt{SR}_{\mathtt{SFOS}}^{\mathtt{Wh}}$-19: > 200	

to have higher $E_{\mathrm{T}}^{\mathrm{miss}}$ significance than the SM background, therefore, the events are required to have $E_{\mathrm{T}}^{\mathrm{miss}}$ significance > 8. The third lepton is more likely to be a FNP lepton in the reducible background than for the signal. To reduce this contribution, the lower bound on the third lepton p_{T} is increased to 15 and 20 GeV in the $\mathrm{SR}^{\mathrm{Wh}}_{\mathrm{DFOS}}$-1 and $\mathrm{SR}^{\mathrm{Wh}}_{\mathrm{DFOS}}$-2 regions, respectively. Angular proximity between leptons coming from a Higgs-boson decay is used for further event separation, using the variable $\Delta R_{\mathrm{OS,near}}$, defined as the ΔR between the DF lepton and the SFSS lepton nearest in ϕ. The signal is expected to populate the lower range in $\Delta R_{\mathrm{OS,near}}$, while the SM background tends to have a more flat distribution. Events in $\mathrm{SR}^{\mathrm{Wh}}_{\mathrm{DFOS}}$-1 are required to pass $\Delta R_{\mathrm{OS,near}} < 1.2$. To suppress the higher $t\bar{t}$ contribution in the $\mathrm{SR}^{\mathrm{Wh}}_{\mathrm{DFOS}}$-2, a tighter selection on $\Delta R_{\mathrm{OS,near}}$ is imposed. A complete summary of the selection criteria in $\mathrm{SR}^{\mathrm{Wh}}_{\mathrm{DFOS}}$ is presented in Table 5.

Table 5: Summary of the selection criteria for SRs targeting events with a DFOS lepton pair, for the *Wh* selection. $\mathrm{SR}^{\mathrm{Wh}}_{\mathrm{DFOS}}$ preselection criteria are applied (Table 2).

	Selection requirements	
Variable	$\mathrm{SR}^{\mathrm{Wh}}_{\mathrm{DFOS}}$-1	$\mathrm{SR}^{\mathrm{Wh}}_{\mathrm{DFOS}}$-2
n_{jets}	$= 0$	$\in [1, 2]$
$E_{\mathrm{T}}^{\mathrm{miss}}$ significance	> 8	> 8
$p_{\mathrm{T}}^{\ell_3}$ [GeV]	> 15	> 20
$\Delta R_{\mathrm{OS,near}}$	< 1.2	< 1.0

6.2 Background estimation

The normalisation of the *WZ* background is measured in CRs characterised by moderate values of the $E_{\mathrm{T}}^{\mathrm{miss}}$ and m_{T} variables. The CRs contain only events with a SFOS pair with an invariant mass of $75 < m_{\ell\ell} < 105$ GeV, targeting on-shell decays. Additional requirements of $50 < E_{\mathrm{T}}^{\mathrm{miss}} < 100$ GeV and $20 < m_{\mathrm{T}} < 100$ GeV improve the *WZ* purity. To address the possible mis-modelling of the jet multiplicity in the *WZ* simulated samples, the cross-section normalisation factor is extracted separately in each jet multiplicity and H_{T} category, using $\mathrm{CRWZ}^{\mathrm{WZ}}_{0\mathrm{j}}$, $\mathrm{CRWZ}^{\mathrm{WZ}}_{\text{low-}H_{\mathrm{T}}}$, and $\mathrm{CRWZ}^{\mathrm{WZ}}_{\text{high-}H_{\mathrm{T}}}$. The estimation is cross-checked in kinematically similar, orthogonal VRs: $\mathrm{VRWZ}^{\mathrm{WZ}}_{0\mathrm{j}}$, $\mathrm{VRWZ}^{\mathrm{WZ}}_{\text{low-}H_{\mathrm{T}}}$, and $\mathrm{VRWZ}^{\mathrm{WZ}}_{\text{high-}H_{\mathrm{T}}}$. A summary of the selection criteria defining the *WZ* CRs and VRs is presented in Table 6. The *WZ* purity is about 80% in all CRs and VRs. The signal contamination is almost negligible in the CRs and increases up to 10% in the VRs.

Table 6: Summary of the selection criteria for the CRs and VRs for *WZ*, for the on-shell *WZ* and *Wh* selections. On-shell preselection criteria are applied (Table 2). In rows where only one value is given it applies to all regions. "-" indicates no requirement is applied for a given variable/region.

Variable	$\mathrm{CRWZ}^{\mathrm{WZ}}$			$\mathrm{VRWZ}^{\mathrm{WZ}}$		
	0j	low-H_{T}	high-H_{T}	0j	low-H_{T}	high-H_{T}
n_{jets}	=0	≥ 1	≥ 1	=0	≥ 1	≥ 1
H_{T} [GeV]	-	< 200 GeV	> 200 GeV	-	< 200 GeV	> 200 GeV
n_{SFOS}		≥ 1			≥ 1	
m_{T} [GeV]		$\in [20, 100]$			$\in [20, 100]$	
$m_{\ell\ell}$ [GeV]		$\in [75, 105]$			$\in [75, 105]$	
$\lvert m_{3\ell} - m_Z \rvert$ [GeV]		> 15			> 15	
$E_{\mathrm{T}}^{\mathrm{miss}}$ [GeV]		$\in [50, 100]$			> 100	

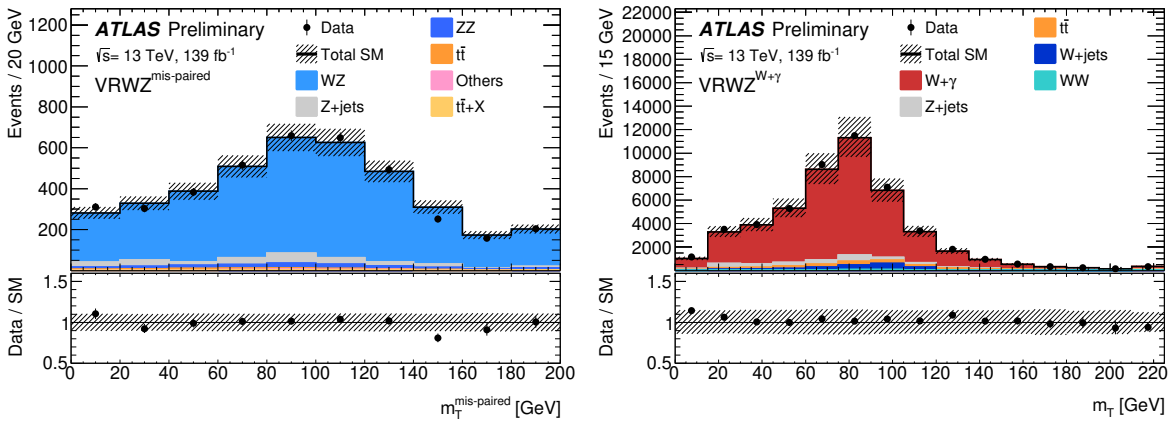

Figure 3: Distributions of m_{T} showing the data and the pre-fit expected background in (left) the mis-paired lepton validation region and (right) the $W + \gamma$ validation region, which are used to validate the WZ background. The first (last) bin includes underflow (overflow). The "Others" category contains backgrounds from single-top, WW, triboson, Higgs and rare top processes. The bottom panel shows the ratio of the observed data to the predicted yields. The hatched bands indicate the combined theoretical, experimental, and MC statistical uncertainties.

Performing the simultaneous background-only fit for the on-shell WZ and Wh selections, normalisation factors for WZ of 1.07 ± 0.02 ($\mathtt{CRWZ}^{\mathtt{WZ}}_{\mathtt{0j}}$), 0.94 ± 0.03 ($\mathtt{CRWZ}^{\mathtt{WZ}}_{\mathtt{low\text{-}H_T}}$) and 0.85 ± 0.05 ($\mathtt{CRWZ}^{\mathtt{WZ}}_{\mathtt{high\text{-}H_T}}$) are found.

A good description of the m_{T} and $E_{\mathrm{T}}^{\mathrm{miss}}$ distributions in the WZ simulation is crucial in this analysis, especially in the high-m_{T} and high-$E_{\mathrm{T}}^{\mathrm{miss}}$ tails where new physics may appear. The tail of the m_{T} distribution is a result of, in decreasing order of importance: the use of a wrong pair of leptons to compute the mass of the Z-boson candidate and the m_{T} of the W-boson candidate ("mis-pairing" of the leptons), the $E_{\mathrm{T}}^{\mathrm{miss}}$ resolution, and the W-boson width. The prediction of lepton mis-pairing in simulation is validated in a control sample in data similar to the one used to calculate the cross-section normalisation factor, but only allowing events with a SFOS pair of different flavour than the W lepton. The Z-boson candidate can then unambiguously be identified, and a mis-paired control sample is obtained using the DFOS pair in the $m_{\ell\ell}$ computation and using the third lepton to calculate m_{T}. Finally, the modelling of the m_{T} and $E_{\mathrm{T}}^{\mathrm{miss}}$ distributions is validated in a $W + \gamma$ control sample. The $W + \gamma$ and WZ processes have very similar m_{T} shapes because their production mechanisms are similar, with the exception that the FSR production diagram of $W + \gamma$ is much more common than the corresponding diagram in WZ, which is doubly suppressed due to the mass of the Z boson and its weak coupling to leptons. Furthermore, a photon is a good proxy for a leptonically decaying Z boson since photons and leptons are reconstructed with comparable resolutions, and no large extra mis-measurements are expected. The enhancement of the FSR diagram in the $W + \gamma$ process leads to differences in the m_{T} shapes between WZ and $W + \gamma$. When a photon is radiated, leptons lose energy, resulting in a lower m_{T}. In order to use the $W + \gamma$ m_{T} shape to validate the WZ MC prediction, the FSR contribution in the $W + \gamma$ control region has to be suppressed. This is done by applying thresholds on the p_{T} of the photon, $p_{\mathrm{T}}^{\gamma} > 50$ GeV, and the separation between the lepton and the photon, $\Delta\mathrm{R}(\mathrm{l}, \gamma) > 0.4$, in $W + \gamma$ events, as FSR photons are expected to be close to the lepton radiating them and also tend to have low p_{T}. The m_{T} and $E_{\mathrm{T}}^{\mathrm{miss}}$ shapes, as well as other kinematic variables, are compared in data and MC in the $\mu + \gamma$ region. The m_{T} distribution in the validation region with mispaired leptons and the $W + \gamma$ validation region are demonstrated in Figure 3. Good agreement in both control samples is observed and no extra corrections or scale factors are applied to correct the m_{T} distribution for the WZ background.

The $t\bar{t}$ MC modelling is validated in VRs, enhancing the $t\bar{t}$ contribution by requiring a DFOS lepton pair and using a moderate $E_{\mathrm{T}}^{\mathrm{miss}} > 50$ GeV selection. The main VR, $\mathtt{VRtt}^{\mathtt{WZ}}$, requires the presence of one or two b-jets, further increasing the $t\bar{t}$ contribution. To validate the modelling also in the $n_{\mathrm{jets}} = 0$ region, an additional VR inclusive in b-jets, $\mathtt{VRtt}^{\mathtt{WZ}}_{\mathrm{incl}}$, is considered, with a $E_{\mathrm{T}}^{\mathrm{miss}}$ significance < 8 requirement to ensure orthogonality with the $\mathtt{SR}^{\mathtt{Wh}}_{\mathtt{DFOS}}$ regions. The selection requirements for the $t\bar{t}$ VRs are summarised in Table 7.

Z+jets is estimated using the FF method as described in Section 5.2. For measurement region $\mathtt{CRFF}^{\mathtt{WZ}}$, the Z-boson candidate mass must be compatible with the Z-boson mass within 15 GeV, and low $E_{\mathrm{T}}^{\mathrm{miss}}$ and m_{T} are required to minimise WZ contributions. The FFs are parametrised as a function of lepton p_{T} and η in the event. The Z+jets estimation is then validated in $\mathtt{VRFF}^{\mathtt{WZ}}$, considering the intermediate $E_{\mathrm{T}}^{\mathrm{miss}}$ range closer to but orthogonal to the SRs, and adding a $m_{3\ell}$ lower bound to reduce WZ contamination. The selection criteria for $\mathtt{CRFF}^{\mathtt{WZ}}$ as well as those of $\mathtt{VRFF}^{\mathtt{WZ}}$ are summarised in Table 7.

Figure 4 presents the m_{T} distributions in $\mathtt{CRWZ}^{\mathtt{WZ}}_{\mathtt{high\text{-}H_T}}$ and $\mathtt{VRWZ}^{\mathtt{WZ}}_{\mathtt{high\text{-}H_T}}$, and the $\Delta R_{\mathrm{OS,near}}$ and $E_{\mathrm{T}}^{\mathrm{miss}}$ distributions in $\mathtt{VRtt}^{\mathtt{WZ}}$, showing good agreement between observed data and background estimation. The comparisons between the expected and observed yields in the $\mathtt{CRWZ}^{\mathtt{WZ}}$and all $\mathtt{VR}^{\mathtt{WZ}}_{\cdot}$ are given in Figure 5.

The systematic uncertainties considered in the on-shell WZ and Wh SRs follow the approach discussed in Section 5.3. An additional source of uncertainty is considered that accounts for the different fake lepton compositions in the CRFF and $\mathtt{SR}^{\mathtt{WZ}}$. This uncertainty arises from the performance of the method in the simulation (closure) in various regions of parameter space and is given by the deviations between the estimated and the simulated events in the given region. In the DFOS region where triboson contribution becomes dominant, the uncertainties related to the QCD renormalisation and factorisation scales are evaluated also for this background component, in the same way as previously described for diboson and $t\bar{t}$. A summary of the considered systematic uncertainties is presented in Figure 6. The uncertainties related to experimental effects are grouped and shown as "Experimental" uncertainty. This uncertainty is applied for all processes whose yield is estimated from simulation. The "Modelling" uncertainty groups the uncertainties due to the theoretical uncertainties. The "Fakes" group represents the uncertainties for FNP background processes whose yield is estimated from data. The "MC stat" stands for the statistical uncertainties on the simulated events. Finally, the "Normalisation" group describes the uncertainties related to the normalisation factors.

Table 7: Summary of the selection criteria for the CRs and VRs for $t\bar{t}$ and Z+jets, for the on-shell WZ and Wh selections. On-shell preselection criteria are applied (Table 2) "-" indicates no requirement is applied for a given variable/region.

Variable	$\mathtt{VRtt}^{\mathtt{WZ}}$	$\mathtt{VRtt}^{\mathtt{WZ}}_{\mathrm{incl}}$	$\mathtt{CRFF}^{\mathtt{WZ}}$	$\mathtt{VRFF}^{\mathtt{WZ}}$
n_{SFOS}	$= 0$	$= 0$	≥ 1	≥ 1
$n_{b\text{-jets}}$	$\in [1, 2]$	-	=0	=0
$\lvert m_{\ell\ell} - m_Z \rvert$ [GeV]	-	-	< 15	< 15
$p_{\mathrm{T}}{}^{\ell_{Z1}}$, $p_{\mathrm{T}}{}^{\ell_{Z2}}$ [GeV]	-	-	$> 25, > 20$	-
$E_{\mathrm{T}}^{\mathrm{miss}}$ [GeV]	> 50	> 50	$\in [20, 50]$	$\in [50, 100]$
$E_{\mathrm{T}}^{\mathrm{miss}}$ significance	-	< 8	-	-
m_{T} [GeV]	-	-	< 20	< 20
$m_{3\ell}$ [GeV]	-	-	-	$\in [105, 160]$

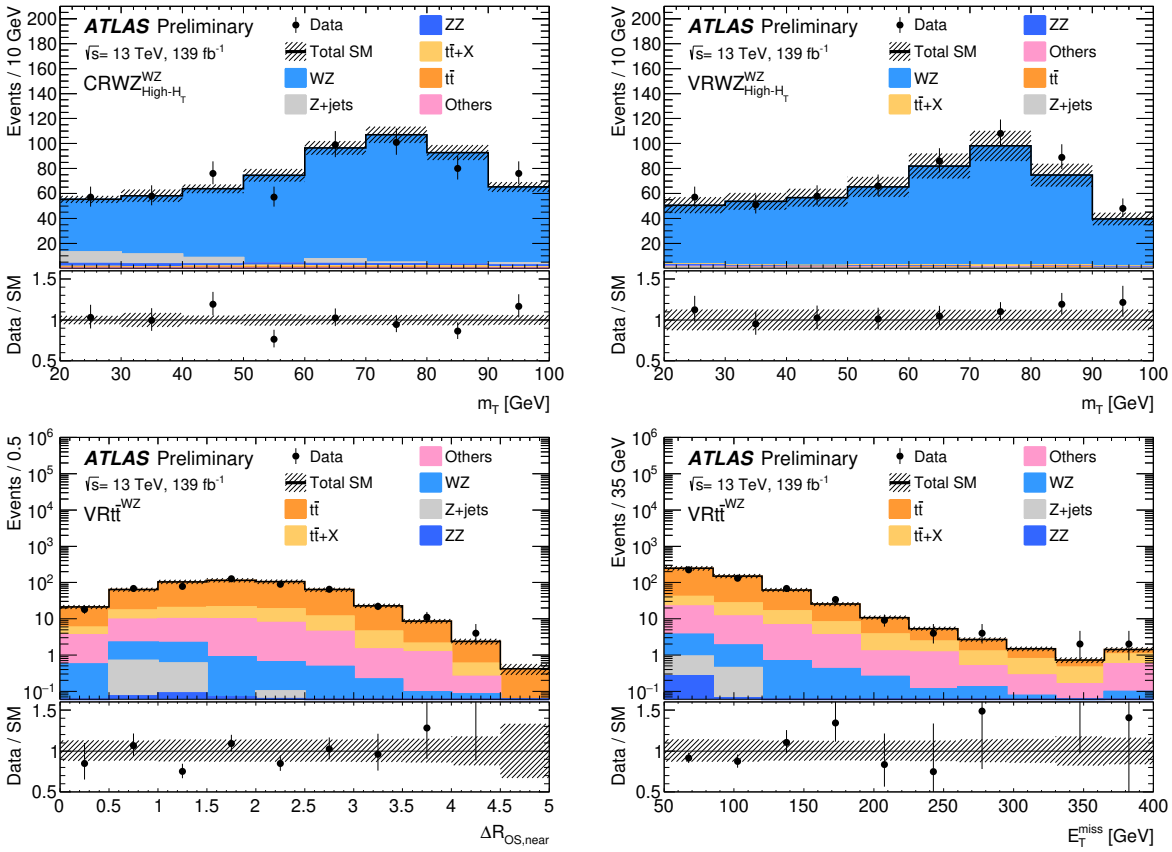

Figure 4: Example of kinematic distribution after the background-only fit, showing the data and the post-fit expected background, in regions of the on-shell WZ and Wh selections. The figure shows the m_{T} distribution in (top left) $\mathtt{CRWZ}^{\mathtt{WZ}}_{\mathtt{high\text{-}H_T}}$ and (top right) $\mathtt{VRWZ}^{\mathtt{WZ}}_{\mathtt{high\text{-}H_T}}$, and the (bottom left) $\Delta R_{\mathrm{OS,near}}$ and (bottom right) $E_{\mathrm{T}}^{\mathrm{miss}}$ distributions in $\mathtt{VRtt}^{\mathtt{WZ}}$. The first (last) bin includes underflow (overflow). The "Others" category contains backgrounds from single-top, WW, triboson, Higgs and rare top processes. The bottom panel shows the ratio of the observed data to the predicted yields. The hatched bands indicate the combined theoretical, experimental, and MC statistical uncertainties.

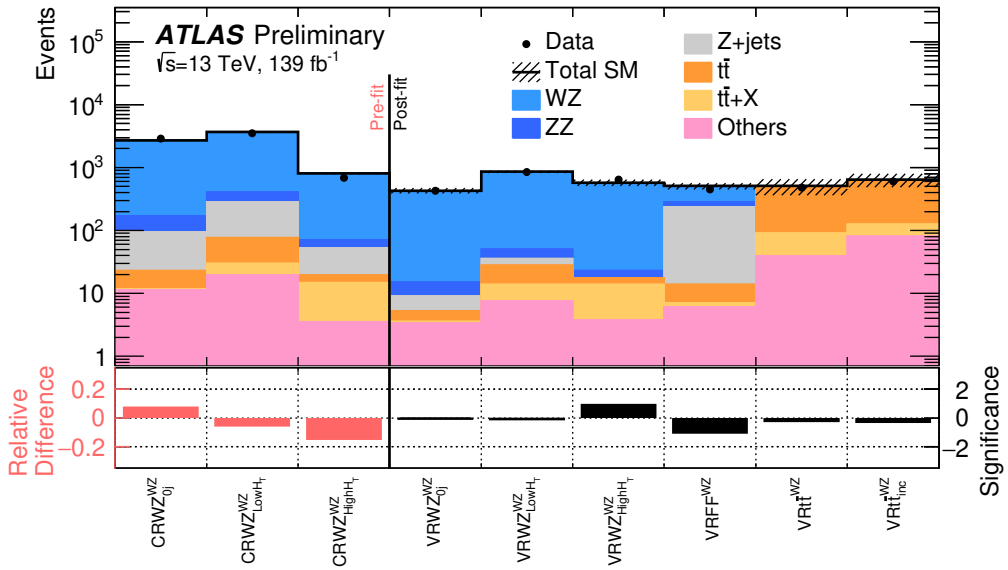

Figure 5: Comparison of the observed data and expected SM background yields in the CRs (pre-fit) and VRs (post-fit) of the on-shell *WZ* and *Wh* selections. The "Others" category contains the single-top, WW, triboson, Higgs and rare top processes. The hatched band indicates the combined theoretical, experimental, and MC statistical uncertainties. The bottom panel shows the relative difference between the observed data and expected yields for the CRs and the significance of the difference for the VRs, calculated with the profile likelihood method from [135], adding a minus sign if the yield is below the prediction.

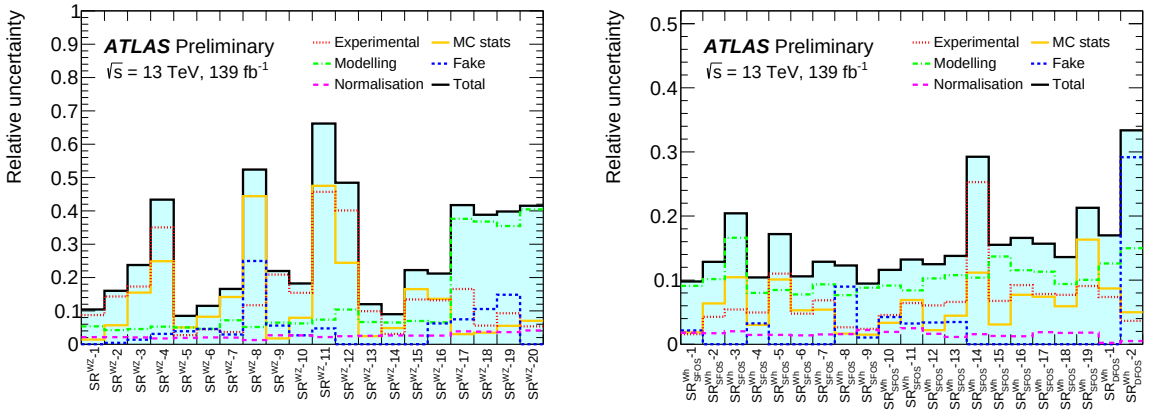

Figure 6: Breakdown of the systematic uncertainties in the event yields in the SRs for (left) the on-shell *WZ* selection and (right) the *Wh* selection.

Bin-to-bin fluctuations in the statistical uncertainty as well as the experimental uncertainty reflect the difference in expected yields in the various search regions, which varies by an order of magnitude. These uncertainties become the dominant ones in $\mathrm{SR}^{\mathrm{WZ}}$-3-4, 6-8, 11-12 and 15-16 of the on-shell *WZ* selection, and $\mathrm{SR}^{\mathrm{Wh}}_{\mathrm{SFOS}}$-5, $\mathrm{SR}^{\mathrm{Wh}}_{\mathrm{SFOS}}$-14, and $\mathrm{SR}^{\mathrm{Wh}}_{\mathrm{SFOS}}$-19 of the *Wh* selections, due to limited MC simulation statistics at high $E_{\mathrm{T}}^{\mathrm{miss}}$ and m_{T}. Although the fakes uncertainty is negligible in the majority of the search bins, its relative size goes up to 30% in $\mathrm{SR}^{\mathrm{Wh}}_{\mathrm{DFOS}}$-2, due to the low statistics in the corresponding anti-ID sample. The modelling uncertainty, mainly due to the QCD renormalisation and factorisation scales, is more pronounced in the high H_{T} regions ($\mathrm{SR}^{\mathrm{WZ}}$-17–$\mathrm{SR}^{\mathrm{WZ}}$-20), reflecting poorer ISR jets modelling in the MC simulation samples.

7 Off-shell WZ selection

The following subsections discuss the implementation and optimisation specific to the off-shell WZ selection.

7.1 Search regions

The $\mathtt{SR}^{\mathtt{offWZ}}$ selection targets the off-shell region, rejecting events with on-shell Z-boson candidates by requiring $m_{\ell\ell}^{\min} \leq m_{\ell\ell} < 75$ GeV. In order to maximally suppress combinatorial backgrounds with an on-shell Z boson, $m_{\ell\ell}^{\max} < 75$ GeV is also required, where $m_{\ell\ell}^{\max}$ is the largest SFOS lepton pair invariant mass in the event. The event preselection also vetoes events with a b-jet to reduce contamination from $t\bar{t}$, requires the three leptons to be well separated in $\min \Delta R_{3\ell} = \min[\Delta R(\ell_i, \ell_j)$; for all lepton pairs $(\ell_i, \ell_j)]$, and requires a lower bound on $m_{\ell\ell}^{\min}$ of 1 GeV to remove events with collimated leptons for which FNP lepton background estimation is challenging. Finally, $m_{\ell\ell}^{\min}$ mass ranges of $[3.0, 3.2]$ and $[9, 12]$ GeV are vetoed to avoid contribution from J/ψ and Υ resonance backgrounds associated with a FNP lepton, except in the jet-inclusive high $E_{\mathrm{T}}^{\mathrm{miss}}$ regions ($E_{\mathrm{T}}^{\mathrm{miss}} > 200$ GeV) where the contribution is negligible.

Preselected events are further divided into four categories based on jet multiplicity and $E_{\mathrm{T}}^{\mathrm{miss}}$. The two jet-veto categories reject events containing jets with $p_{\mathrm{T}} > 30$ GeV and select high (low) $E_{\mathrm{T}}^{\mathrm{miss}}$ for $\mathtt{SR}^{\mathtt{offWZ}}_{\mathtt{high}\not{E}_{\mathrm{T}}}\mathtt{-0j}$ ($\mathtt{SR}^{\mathtt{offWZ}}_{\mathtt{low}\not{E}_{\mathrm{T}}}\mathtt{-0j}$) respectively. The two jet-inclusive categories require at least one jet with $p_{\mathrm{T}} > 30$ GeV and select high (low) $E_{\mathrm{T}}^{\mathrm{miss}}$ for $\mathtt{SR}^{\mathtt{offWZ}}_{\mathtt{high}\not{E}_{\mathrm{T}}}\mathtt{-nj}$ ($\mathtt{SR}^{\mathtt{offWZ}}_{\mathtt{low}\not{E}_{\mathrm{T}}}\mathtt{-nj}$) respectively. As the $E_{\mathrm{T}}^{\mathrm{miss}}$ is harder in the jet-inclusive categories, due to the recoil between the $\tilde{\chi}_1^{\pm}\tilde{\chi}_2^0$ system and the jets, the boundary between the low and high $E_{\mathrm{T}}^{\mathrm{miss}}$ bins is set at 50 GeV for the jet-veto categories and at 200 GeV for the jet-inclusive categories. The $\mathtt{SR}^{\mathtt{offWZ}}_{\mathtt{low}\not{E}_{\mathrm{T}}}\mathtt{-0j}$, $\mathtt{SR}^{\mathtt{offWZ}}_{\mathtt{low}\not{E}_{\mathrm{T}}}\mathtt{-nj}$ and $\mathtt{SR}^{\mathtt{offWZ}}_{\mathtt{high}\not{E}_{\mathrm{T}}}\mathtt{-0j}$ primarily target signals with moderate mass splitting ($\Delta m \sim [40, 90]$ GeV), and rely mostly on moderate kinematics and lepton triggers. The $\mathtt{SR}^{\mathtt{offWZ}}_{\mathtt{high}\not{E}_{\mathrm{T}}}\mathtt{-nj}$ also targets signals with highly compressed mass spectra ($\Delta m \lesssim 40$ GeV), resulting in events with very soft leptons, by exploiting events with large $E_{\mathrm{T}}^{\mathrm{miss}}$ recoiling off of hard hadronic activity.

Further preselection criteria are applied to reduce the contamination from Z+jets. First, a lower bound is set at $E_{\mathrm{T}}^{\mathrm{miss}}$ significance > 1.5 or 3.0, depending on the SR category. For $\mathtt{SR}^{\mathtt{offWZ}}_{\mathtt{low}\not{E}_{\mathrm{T}}}$, events are then treated separately based on the flavour of the lepton from the W-boson decay, as selected using $m_{\ell\ell}$ lepton assignment (ℓ_W). To suppress the contribution from $Z(+\gamma) \to \ell\ell ee$ caused by bremsstrahlung from prompt electrons and subsequent photon conversions, if ℓ_W is an electron, the tri-lepton invariant mass $m_{3\ell}$ is required to be off the Z-boson peak ($|m_{3\ell} - m_Z| > 20$ GeV), and the minimum angular distance between all SFOS lepton pairs must be within $\min \Delta R_{\mathrm{SFOS}} \in [0.6, 2.4]$, with $\min \Delta R_{\mathrm{SFOS}}$ defined as $\min[\Delta R(\ell_i, \ell_j)$; for all SFOS lepton pairs $(\ell_i, \ell_j)]$. The preselection criteria and categorisation are summarised in Table 8.

The primary discriminant in $\mathtt{SR}^{\mathtt{offWZ}}$ is $m_{\ell\ell}^{\min}$. This variable serves as a proxy for the mass splitting of the targeted signals, and displays a characteristic kinematic edge at their mass splitting value: $m_{\ell\ell}^{\min} = \Delta m$, as demonstrated in Figure 7. A shape fit over the $m_{\ell\ell}^{\min}$ spectrum is performed in each SR category. Seven $m_{\ell\ell}^{\min}$ bins are defined with boundaries at 1, 12, 15, 20, 30, 40, 60 and 75 GeV, and labelled a through g; the $m_{\ell\ell}^{\min}$ bin labels are added to the region names as defined above. Signal regions "a" are dropped everywhere except in $\mathtt{SR}^{\mathtt{offWZ}}_{\mathtt{high}\not{E}_{\mathrm{T}}}\mathtt{-nj}$, to avoid hard-to-estimate low mass resonance backgrounds.

A second, similar kinematic edge is present in stransverse mass m_{T2} [136, 137], reflecting the kinematic constraint originating from the $\tilde{\chi}_1^{\pm} \to W^*\tilde{\chi}_1^0$ decay chain. In this selection, m_{T2} is constructed by assigning

Table 8: Summary of the preselection criteria applied in all regions of the off-shell WZ selection. In rows where only one value is given it applies to all regions. "-" indicates no requirement is applied for a given variable/region.

Variable	Preselection requirements				
	$\text{SR}^{\text{offWZ}}_{\text{low}E_{\text{T}}}$-0j	$\text{SR}^{\text{offWZ}}_{\text{low}E_{\text{T}}}$-nj	$\text{SR}^{\text{offWZ}}_{\text{high}E_{\text{T}}}$-0j	$\text{SR}^{\text{offWZ}}_{\text{high}E_{\text{T}}}$-nj	CR^{offWZ}/VR^{offWZ}
$n_{\text{lep}}^{\text{baseline}}$, $n_{\text{lep}}^{\text{signal}}$	= 3				= 3
n_{SFOS}	≥ 1				-
$m_{\ell\ell}$, $m_{\ell\ell}^{\text{max}}$ [GeV]	< 75				-
$m_{\ell\ell}^{\text{min}}$ [GeV]	∈ [1, 75]				-
$n_{b\text{-jets}}$	= 0				-
min $\Delta R_{3\ell}$	> 0.4				> 0.4
resonance veto $m_{\ell\ell}^{\text{min}}$ [GeV]	∉ [3, 3.2], ∉ [9, 12]			-	∉ [3, 3.2], ∉ [9, 12]
trigger	(multi-)lepton		((multi-)lepton ∥ $E_{\text{T}}^{\text{miss}}$)		((multi-)lepton ∥ $E_{\text{T}}^{\text{miss}}$)
$n_{\text{jets}}^{30\text{ GeV}}$	= 0	≥ 1	= 0	≥ 1	-
$E_{\text{T}}^{\text{miss}}$ [GeV]	< 50	< 200	> 50	> 200	-
$E_{\text{T}}^{\text{miss}}$ significance	> 1.5	> 3.0	> 3.0	> 3.0	-
$\lvert m_{3\ell} - m_Z \rvert$ [GeV]	> 20 ($l_W = e$ only)		-		-
min ΔR_{SFOS}	[0.6, 2.4] ($l_W = e$ only)		-		-

the di-lepton system providing $m_{\ell\ell}^{\text{min}}$ ($\ell_1\ell_2$) to one visible particle leg, and the remaining lepton (ℓ_3) to the other leg:

$$m_{\text{T2}}^{m_\chi}\left(\mathbf{p}_{\text{T}}^{\ell_1\ell_2}, \mathbf{p}_{\text{T}}^{\ell_3}, \mathbf{p}_{\text{T}}^{\text{miss}}\right) = \min_{\mathbf{q}_{\text{T}}}\left(\max\left[m_{\text{T}}\left(\mathbf{p}_{\text{T}}^{\ell_1\ell_2}, \mathbf{q}_{\text{T}}, m_\chi\right), m_{\text{T}}\left(\mathbf{p}_{\text{T}}^{\ell_3}, \mathbf{p}_{\text{T}}^{\text{miss}} - \mathbf{q}_{\text{T}}, m_\chi\right)\right]\right),$$

where the transverse mass m_T in this m_{T2} formula is defined by

$$m_{\text{T}}\left(\mathbf{p}_{\text{T}}^{\ell}, \mathbf{q}_{\text{T}}, m_\chi\right) = \sqrt{m_\ell^2 + m_\chi^2 + 2\left(\sqrt{(p_{\text{T}}^{\ell})^2 + m_\ell^2}\sqrt{q_{\text{T}}^2 + m_\chi^2} - \mathbf{p}_{\text{T}}^{\ell}\cdot\mathbf{q}_{\text{T}}\right)}.$$

m_χ is the hypothesised mass assigned to each invisible particle leg, corresponding to the $\tilde{\chi}_1^0$ mass; m_χ is fixed to 100 GeV[5] in this selection. The kinematic edge for signals appears at $m_{\text{T2}}^{100} = \Delta m(\tilde{\chi}_2^0, \tilde{\chi}_1^0) + 100$ GeV as illustrated in Figure 7. To take advantage of this feature, a sliding cut is applied per $m_{\ell\ell}^{\text{min}}$ bin, requiring m_{T2}^{100} to be smaller than the upper $m_{\ell\ell}^{\text{min}}$ bin edge - 100 GeV. SM backgrounds can exceed the boundary and are suppressed, while a large fraction of the signal contribution targeted by a given bin is maintained. The cut is particularly effective in the lowest $m_{\ell\ell}^{\text{min}}$ bins, targeting the smallest mass splittings: e.g. in $\text{SR}^{\text{offWZ}}_{\text{high}E_{\text{T}}}$-nja ($m_{\ell\ell}^{\text{min}} \in [1, 12]$ GeV) the total background reduction due to $m_{\ell\ell}^{\text{min}} < 112$ GeV is 1/3, while the efficiency for $\Delta m = 10$ GeV signals is > 95%.

Event selection is tightened further employing various background rejection criteria, optimised separately for each SR^{offWZ} category and each $m_{\ell\ell}^{\text{min}}$ bin. The discriminating variables used and the detailed bin-by-bin cut values are summarised in Table 9.

[5] The dependency of the performance on hypothetical invisible particle mass m_χ is generally small except when assuming $m_\chi \sim 0$ GeV for signals with finite $\tilde{\chi}_1^0$ mass, where the signal kinematic edges become significantly smeared.

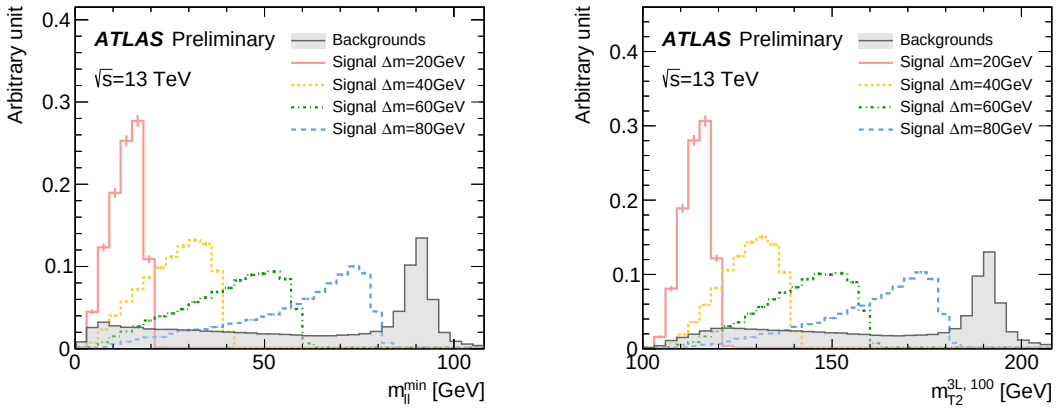

Figure 7: Distributions of (left) $m_{\ell\ell}^{\text{min}}$ and (right) m_{T2}^{100} showing the expected SM background as well as signals with various mass splittings ($m(\tilde{\chi}_1^{\pm}) = m(\tilde{\chi}_2^0) = 200$ GeV), for a selection of exactly three baseline and signal leptons. The distributions are normalised to unity. Signals demonstrate a cut-off in both variables matching the mass splitting, while backgrounds do not. The dominant background in this selection is WZ, with the Z-boson mass peak visible in both distributions.

Table 9: Summary of the selection criteria for SRs for the off-shell WZ selection. SR^{offWZ} preselection criteria are applied (Table 8). "-" indicates no requirement is applied for a given variable/region, while × is marked for regions that aren't considered.

	Selection requirements								
Variable	a	b	c	d	e	f1	f2	g1	g2
$m_{\ell\ell}^{\text{min}}$ [GeV]	[1,12]	[12,15]	[15,20]	[20,30]	[30,40]	[40,60]		[60,75]	
	$\text{SR}^{\text{offWZ}}_{\text{low}E_{\text{T}}^{\text{miss}}}$ common								
$m_{\ell\ell}^{\text{max}}$ [GeV]	×	< 60	< 60	< 60	< 60	-	-	-	-
$m_{\text{T}}^{\text{mllmin}}$ [GeV]	×	< 50	< 50	< 50	< 60	< 60	< 90	< 60	> 90
m_{T2}^{100} [GeV]	×	< 115	< 120	< 130	-	-	-	-	-
$\min \Delta R_{\text{SFOS}}$	×	< 1.6	< 1.6	< 1.6	-	-	-	-	-
$p_{\text{T}}^{\ell_1}, p_{\text{T}}^{\ell_2}, p_{\text{T}}^{\ell_3}$ [GeV]	×	> 10	> 10	> 10	> 10	> 15	> 15	> 15	> 15
	$\text{SR}^{\text{offWZ}}_{\text{low}E_{\text{T}}^{\text{miss}}}$-0j								
$\lvert\mathbf{p}_{\text{T}}^{\text{lep}}\rvert / E_{\text{T}}^{\text{miss}}$	×	< 1.1	< 1.1	< 1.1	< 1.3	< 1.4	< 1.4	< 1.4	< 1.4
$m_{3\ell}$ [GeV]	×	-	-	-	-	> 100	> 100	> 100	> 100
	$\text{SR}^{\text{offWZ}}_{\text{low}E_{\text{T}}^{\text{miss}}}$-nj								
$\lvert\mathbf{p}_{\text{T}}^{\text{lep}}\rvert / E_{\text{T}}^{\text{miss}}$	×	< 1.0	< 1.0	< 1.0	< 1.0	< 1.2	< 1.2	< 1.2	< 1.2
	$\text{SR}^{\text{offWZ}}_{\text{high}E_{\text{T}}^{\text{miss}}}$ common								
m_{T2}^{100} [GeV]	< 112	< 115	< 120	< 130	< 140	< 160	< 160	< 175	< 175
	$\text{SR}^{\text{offWZ}}_{\text{high}E_{\text{T}}^{\text{miss}}}$-0j								
$p_{\text{T}}^{\ell_1}, p_{\text{T}}^{\ell_2}, p_{\text{T}}^{\ell_3}$ [GeV]	-	> 25, > 15, > 10							
$m_{\text{T}}^{\text{mllmin}}$ [GeV]	-	< 50	< 50	< 60	< 60	< 70	> 90	< 70	> 90
	$\text{SR}^{\text{offWZ}}_{\text{high}E_{\text{T}}^{\text{miss}}}$-nj								
						f		g	
$\lvert\mathbf{p}_{\text{T}}^{\text{lep}}\rvert / E_{\text{T}}^{\text{miss}}$	< 0.2	< 0.2	< 0.3	< 0.3	< 0.3	< 1.0		< 1.0	

The transverse mass $m_{\mathrm{T}}^{\mathrm{mllmin}}$ is used in $\mathrm{SR}^{\mathtt{offWZ}}_{\mathtt{low}\not{E}_{\mathrm{T}}}\text{-}\mathtt{0j}$, $\mathrm{SR}^{\mathtt{offWZ}}_{\mathtt{low}\not{E}_{\mathrm{T}}}\text{-}\mathtt{nj}$ and $\mathrm{SR}^{\mathtt{offWZ}}_{\mathtt{high}\not{E}_{\mathrm{T}}}\text{-}\mathtt{0j}$ to suppress the SM WZ contribution; the $m_{\mathrm{T}}^{\mathrm{mllmin}}$ variable is constructed using $m_{\ell\ell}^{\mathrm{min}}$ lepton assignment and marked with "minmll" to distinguish it from the m_{T} variable in the on-shell WZ selection. SRs target phase space either below or above the SM W-boson peak present at $m_{\mathrm{T}}^{\mathrm{mllmin}} \sim m_W$. An upper bound of $m_{\mathrm{T}}^{\mathrm{mllmin}} < 50 - 70$ GeV is applied in low $m_{\ell\ell}^{\mathrm{min}}$ bins, while the "`f`" and "`g`" bins are split into two parts below ("`f1`", "`g1`") and above ("`f2`", "`g2`") the Jacobian peak of SM WZ. Lepton p_{T} thresholds are raised in these SR categories as well, in order to reduce the FNP lepton background contributions from Z+jets and $t\bar{t}$.

In $\mathrm{SR}^{\mathtt{offWZ}}_{\mathtt{low}\not{E}_{\mathrm{T}}}$, the selection on $\min \Delta R_{\mathrm{SFOS}}$ is tightened in the low $m_{\ell\ell}^{\mathrm{min}}$ bins exploiting the topology with a relatively boosted Z^* in the target signatures, and a lower bound on $m_{3\ell}$ is applied for the high $m_{\ell\ell}^{\mathrm{min}}$ bins to reject the SM $Z \to 4\ell$ background peaking at $m_{3\ell} \sim m_Z$. The ratio of the magnitude of a vectorial p_{T} sum of the three leptons, $|\mathbf{p}_{\mathrm{T}}^{\mathrm{lep}}|$, to $E_{\mathrm{T}}^{\mathrm{miss}}$, is labelled $|\mathbf{p}_{\mathrm{T}}^{\mathrm{lep}}|/E_{\mathrm{T}}^{\mathrm{miss}}$ and represents the extent to which the transverse momentum of the hard-scatter $\widetilde{\chi}_1^{\pm}\widetilde{\chi}_2^0$ system, recoiling against ISR jets, is converted into leptons as opposed to $E_{\mathrm{T}}^{\mathrm{miss}}$. Due to the presence of a massive $\widetilde{\chi}_1^0$, contributing to the $E_{\mathrm{T}}^{\mathrm{miss}}$, signals tend to populate lower parts of the $|\mathbf{p}_{\mathrm{T}}^{\mathrm{lep}}|/E_{\mathrm{T}}^{\mathrm{miss}}$ spectrum than SM backgrounds, particularly for the compressed signals in the high $E_{\mathrm{T}}^{\mathrm{miss}}$ regions where the $E_{\mathrm{T}}^{\mathrm{miss}}$ is almost fully generated by the ISR jets. A tight upper bound $|\mathbf{p}_{\mathrm{T}}^{\mathrm{lep}}|/E_{\mathrm{T}}^{\mathrm{miss}}$ is therefore placed in the low $m_{\ell\ell}^{\mathrm{min}}$ bins of $\mathrm{SR}^{\mathtt{offWZ}}_{\mathtt{high}\not{E}_{\mathrm{T}}}\text{-}\mathtt{nj}$.

7.2 Background estimation

The selection criteria for the CRs and the VRs for WZ estimation are summarised in Table 10. An on-shell Z boson ($m_{\ell\ell} \in [81, 101]$ GeV) is required to ensure orthogonality to the $\mathrm{SR}^{\mathtt{offWZ}}$, and an upper-cut in $E_{\mathrm{T}}^{\mathrm{miss}}$ to be orthogonal to the $\mathrm{SR}^{\mathtt{WZ}}$. A lower cut in m_{T} is applied to suppress the Z+jets background. The CRs are further split into two bins ($\mathrm{CRWZ}^{\mathtt{offWZ}}_{\mathtt{0j}}$ and $\mathrm{CRWZ}^{\mathtt{offWZ}}_{\mathtt{nj}}$) based on the presence of jets, to separately constrain WZ events with or without hard ISR jets with individual normalisation factors.

Three validation regions are defined in the region with $m_{\ell\ell}^{\mathrm{min}} \leq m_{\ell\ell} < 75$ GeV, similar to $\mathrm{SR}^{\mathtt{offWZ}}$. First, $\mathrm{VRWZ}^{\mathtt{offWZ}}_{\mathtt{0j}}$ and $\mathrm{VRWZ}^{\mathtt{offWZ}}_{\mathtt{nj}}$ are designed to validate the WZ estimation in the $\mathrm{SR}^{\mathtt{offWZ}}_{\mathtt{low}\not{E}_{\mathrm{T}}}$ phase space. A window in m_{T} around the Jacobian peak ($m_{\mathrm{T}} \in [60, 90]$ GeV) is selected to enhance WZ, as well as to ensure the orthogonality with respect to the SRs. Further kinematic selection criteria are applied similar to those in $\mathrm{SR}^{\mathtt{offWZ}}_{\mathtt{low}\not{E}_{\mathrm{T}}}$. Two additional variables are employed in the $\mathrm{VRWZ}^{\mathtt{offWZ}}_{\mathtt{0j}}$ to suppress the signal contamination in the region. The W-boson mass, $m_W^{\mathrm{reco}\,WZ}$, is reconstructed assuming the WZ topology and balanced longitudinal momenta of the W and Z bosons, and $\Delta R(\ell_W, E_{\mathrm{T}}^{\mathrm{miss}})$ is defined by $\sqrt{\eta^2_{\ell_W} + \Delta\phi(\ell_W, E_{\mathrm{T}}^{\mathrm{miss}})^2}$ where lepton assignment is done following the $m_{\ell\ell}^{\mathrm{min}}$ approach, and ℓ_W is the lepton associated to the W boson. As $m_W^{\mathrm{reco}\,WZ}$ peaks around m_W with a long, positive tail for WZ while signals tend to be more flat, $m_W^{\mathrm{reco}\,WZ} > 75$ GeV is found to effectively reduce signal contamination.

In the very low $m_{\ell\ell}^{\mathrm{min}}$ region, $\mathrm{VRWZ}^{\mathtt{offWZ}}_{\mathtt{nj\text{-}lowm}_{11}}$ is used to validate the WZ estimation in the $\mathrm{SR}^{\mathtt{offWZ}}_{\mathtt{high}\not{E}_{\mathrm{T}}}$ phase space. This region has the low-mass resonance veto applied and a lower bound on $|\mathbf{p}_{\mathrm{T}}^{\mathrm{lep}}|/E_{\mathrm{T}}^{\mathrm{miss}}$ to ensure orthogonality with the SRs. Other kinematic cuts are loosened or removed with respect to $\mathrm{SR}^{\mathtt{offWZ}}_{\mathtt{high}\not{E}_{\mathrm{T}}}$ to increase data statistics in the region. The WZ purity is 85-90% in the CRs and 70-75% in the VRs. The contamination from the benchmark signals is negligible in the CRs and below 15% in the VRs.

The $\texttt{VRtt}^{\texttt{offWZ}}$ selection criteria are summarised in Table 11. At least one b-jet is required to maintain orthogonality with the SRs, $E_{\mathrm{T}}^{\mathrm{miss}} > 50$ GeV is required to suppress the Z+jets contribution in the region, and the low-mass resonance background veto is applied. The $t\bar{t}$ purity in this region is approximately 65%.

The Z+jets background is estimated using the FF method as described in Section 5.2. The FF measurement region for the off-shell WZ selection, $\texttt{CRFF}^{\texttt{offWZ}}$, is summarised in Table 11. The Z-boson candidate is selected by requiring $|m_{\ell\ell} - m_Z| < 10$ GeV, and $E_{\mathrm{T}}^{\mathrm{miss}} < 30$ GeV and $m_{\mathrm{T}} < 30$ GeV are applied to reject contamination from WZ. Additionally $m_{3\ell} > 105$ GeV is applied to suppress $Z \to 4\ell$. To increase the statistics of FNP lepton candidates at high p_{T}, the overlap removal procedure described in Section 4 is modified for this FF measurement so that muons overlapping with jets are always kept. Finally, a jet veto is applied except for events where the FNP lepton candidate is a muon with $p_{\mathrm{T}} > 30$ GeV, in which case $n_{\mathrm{jets}}^{30\ \mathrm{GeV}} \leq 1$ is required to account for the special muon-vs-jet overlap-removal treatment applied to this region.

The FFs are derived separately per lepton flavour of FNP lepton candidates and per signal lepton criterion, i.e. with or without applying the non-prompt BDT, and are parametrised as a function of lepton p_{T} and $E_{\mathrm{T}}^{\mathrm{miss}}$ in the event. The parametrisation in $E_{\mathrm{T}}^{\mathrm{miss}}$ is used to reflect the variation of FNP lepton source with $E_{\mathrm{T}}^{\mathrm{miss}}$, which is required to model the shape of fake $E_{\mathrm{T}}^{\mathrm{miss}}$ correctly. Typically the fraction of FNP leptons originating from heavy-flavour decays varies with $E_{\mathrm{T}}^{\mathrm{miss}}$, because of the neutrinos from the leptonic b/c decays.

The contribution of non-Z+jets processes is subtracted using MC simulated samples. A small normalisation correction is applied to the $t\bar{t}$ events in the simulated anti-ID region to account for the different anti-ID lepton efficiencies in data and MC simulation. Normalisation factors are derived separately depending on the ℓ_W flavour and the b-jet multiplicity in the event. They are measured using the data events in a $t\bar{t}$-enriched control region, $\texttt{CRtt}_{\text{anti-ID}}^{\texttt{offWZ}}$, and are found to be between 0.88 and 0.95. The $\texttt{CRtt}_{\text{anti-ID}}^{\texttt{offWZ}}$ selection requires there to be no SFOS leptons pair in the event, as well as $p_{\mathrm{T}}^{\ell_3} > 10$ GeV and $E_{\mathrm{T}}^{\mathrm{miss}} > 50$ GeV to enhance the $t\bar{t}$ purity.

Two sources of uncertainty specific to the estimation in $\texttt{SR}^{\texttt{offWZ}}$ are considered in addition to those described in Section 5.3. The FF parametrisation uncertainty is evaluated by comparing with different $E_{\mathrm{T}}^{\mathrm{miss}}$ binning, or with a 3D-parametrisation in lepton p_{T}, $E_{\mathrm{T}}^{\mathrm{miss}}$ and lepton η, additionally taking into account the dependency on lepton η. The impact on the Z+jets background yields in the CRs is $\sim 5\%$, and $1-7\%$ in the SRs/VRs. The uncertainty from disabling the muon-vs-jet overlap removal procedure in the FF measurement region is assessed by comparing with alternative FFs measured with muon-vs-jet overlap removal applied for events with a FNP muon candidate of $p_{\mathrm{T}} < 30$ GeV. The variation in the estimated Z+jets yields in the SRs/CRs/VRs is found to be $5-15\%$.

The yields predicted by the FF method are cross-checked in dedicated VRs enriched in FNP lepton backgrounds, as summarised in Table 11. The $E_{\mathrm{T}}^{\mathrm{miss}}$ significance selection is inverted with respect to the SRs to ensure orthogonality. First, $\texttt{VRFF}_{\texttt{0j}}^{\texttt{offWZ}}$ and $\texttt{VRFF}_{\texttt{nj}}^{\texttt{offWZ}}$ are designed to validate the yields in $\texttt{SR}_{\texttt{low}\not{E}_{\tau}}^{\texttt{offWZ}}\texttt{-0j}$ and $\texttt{SR}_{\texttt{low}\not{E}_{\tau}}^{\texttt{offWZ}}\texttt{-nj}$, respectively, while $\texttt{VRFF}_{\texttt{nj-lowp}_{\tau}}^{\texttt{offWZ}}$ aims to cross-check the modelling of FNP leptons with $p_{\mathrm{T}} < 10$ GeV specifically. The Z+jets purity is in the VRs is 50%-80%, while the contamination from signals is negligible.

Table 10: Summary of the selection criteria for the CRs and VRs for WZ and $t\bar{t}$, for the off-shell WZ selection. Off-shell preselection criteria are also applied (Table 8). In rows where only one value is given it applies to all regions. "-" indicates no requirement is applied for a given variable/region.

Variable	$\texttt{CRWZ}_{\texttt{0j}}^{\texttt{offWZ}}$	$\texttt{CRWZ}_{\texttt{nj}}^{\texttt{offWZ}}$	$\texttt{VRWZ}_{\texttt{0j}}^{\texttt{offWZ}}$	$\texttt{VRWZ}_{\texttt{nj}}^{\texttt{offWZ}}$	$\texttt{VRWZ}_{\texttt{nj-lowm}_{11}}^{\texttt{offWZ}}$	$\texttt{VRtt}^{\texttt{offWZ}}$
n_{SFOS}	≥ 1		≥ 1			≥ 1
$n_{b\text{-jets}}$	$= 0$		$= 0$			≥ 1
$m_{\ell\ell}$ [GeV]	$\in [81, 101]$		< 75			< 75
$n_{\text{jets}}^{30\text{ GeV}}$	$= 0$	≥ 1	$= 0$	≥ 1	≥ 1	-
$E_{\text{T}}^{\text{miss}}$ [GeV]	< 50	< 50	< 50	< 80	> 80	> 50
$E_{\text{T}}^{\text{miss}}$ significance	-		> 1.5	> 1.5	> 1.5	-
m_{T} [GeV]	> 50	> 50	$\in [60, 90]$		> 30	-
$m_{\ell\ell}^{\text{min}}$ [GeV]	-		$\in [12, 75]$		$\in [1, 12]$	$\in [1, 75]$
resonance veto $m_{\ell\ell}^{\text{min}}$ [GeV]	-		-	-	$\notin [3, 3.2], \notin [9, 12]$	$\notin [3, 3.2], \notin [9, 12]$
$p_{\text{T}}^{\ell_1}, p_{\text{T}}^{\ell_2}, p_{\text{T}}^{\ell_3}$ [GeV]	> 10		> 10	> 10	-	-
min ΔR	-		$[0.6, 2.4]$ ($l_W = e$ only)		-	-
$\lvert m_{3\ell} - m_Z \rvert$ [GeV]	-		> 20 ($l_W = e$ only)		-	-
$m_W^{\text{reco}\,WZ}$ [GeV]	-		> 75	-	-	-
$\Delta R(\ell_W, E_{\text{T}}^{\text{miss}})$	-		> 2.6	-	-	-
$\lvert \mathbf{p}_{\text{T}}^{\text{lep}} \rvert / E_{\text{T}}^{\text{miss}}$	-		-	-	> 0.3	-

Table 11: Summary of the selection criteria for the CRs and VRs for Z+jets, for the off-shell WZ selection. Off-shell preselection criteria are applied (Table 8). The corresponding anti-ID regions used for the Z+jets prediction follow the same selection criteria, except that at least one of the leptons is anti-ID instead of signal. "-" indicates no requirement is applied for a given variable/region.

Variable	$\texttt{CRFF}^{\texttt{offWZ}}$	$\texttt{CRtt}_{\text{anti-ID}}^{\texttt{offWZ}}$	$\texttt{VRFF}_{\texttt{0j}}^{\texttt{offWZ}}$	$\texttt{VRFF}_{\texttt{nj}}^{\texttt{offWZ}}$	$\texttt{VRFF}_{\texttt{nj-lowp}_{\tau}}^{\texttt{offWZ}}$
n_{SFOS}	≥ 1	$= 0$		≥ 1	
$n_{b\text{-jets}}$	$= 0$	$= 0$ or ≥ 1		$= 0$	
$m_{\ell\ell}$ [GeV]	$\in [81, 101]$	-		< 75	
$n_{\text{jets}}^{30\text{ GeV}}$	≤ 1 if $p_{\text{T}}^{l_W=\mu} > 30$ GeV $= 0$ otherwise	-	$= 0$	≥ 1	≥ 1
$E_{\text{T}}^{\text{miss}}$ [GeV]	< 40	> 50	< 50	< 200	$\in [50, 200]$
$E_{\text{T}}^{\text{miss}}$ significance	-	-	$\in [0.5, 1.5]$	$\in [0.5, 3.0]$	$\in [0.5, 3.0]$
$p_{\text{T}}^{\ell_1}, p_{\text{T}}^{\ell_2}, p_{\text{T}}^{\ell_3}$ [GeV]	-	> 10	> 10	> 10	< 10
$m_{\ell\ell}^{\text{min}}$ [GeV]	-	-	$\in [12, 75]$	$\in [12, 75]$	$\in [1, 75]$
m_{T} [GeV]	< 30	-		< 50	
min ΔR	-	-		$[0.6, 2.4]$ ($l_W = e$ only)	
$m_{3\ell}$ [GeV]	> 105	-		$[81.2, 101.2]$ ($l_W = e$ only)	

Performing the background-only fit, WZ normalisation factors of 1.06 ± 0.03 ($\texttt{CRWZ}^{\texttt{offWZ}}_{\texttt{0j}}$), and 0.93 ± 0.03 ($\texttt{CRWZ}^{\texttt{offWZ}}_{\texttt{nj}}$) are determined. Examples of kinematic distributions in the CRs and VRs, demonstrating good agreement, are presented in Figures 8 and 9. Observed and expected yields for all CRs and VRs are summarised in Figure 10.

The systematic uncertainties considered in the off-shell WZ selection are summarised in Figure 11. They are grouped in the same way as discussed for the on-shell WZ and Wh selections in Section 6.2. As the expected yields can vary by an order of magnitude throughout the regions, bin-to-bin fluctuations are expected in the statistical as well as experimental uncertainty; these uncertainties are often dominant in bins with limited MC statistics in the phase-space of the selection. The fakes uncertainty is naturally more important in bins with larger FNP background contribution, and can fluctuate in bins with low statistics in the corresponding anti-ID sample, such as $\texttt{SR}^{\texttt{offWZ}}_{\texttt{high}\not{E}_{\mathrm{T}}}\texttt{-0jb}$ and $\texttt{SR}^{\texttt{offWZ}}_{\texttt{high}\not{E}_{\mathrm{T}}}\texttt{-njb}$. The modelling uncertainty is larger in the presence of ISR jets and at higher values of $E_{\mathrm{T}}^{\mathrm{miss}}$; the fluctuation in $\texttt{SR}^{\texttt{offWZ}}_{\texttt{low}\not{E}_{\mathrm{T}}}\texttt{-njg2}$ originates from the QCD scale uncertainty on the WZ background.

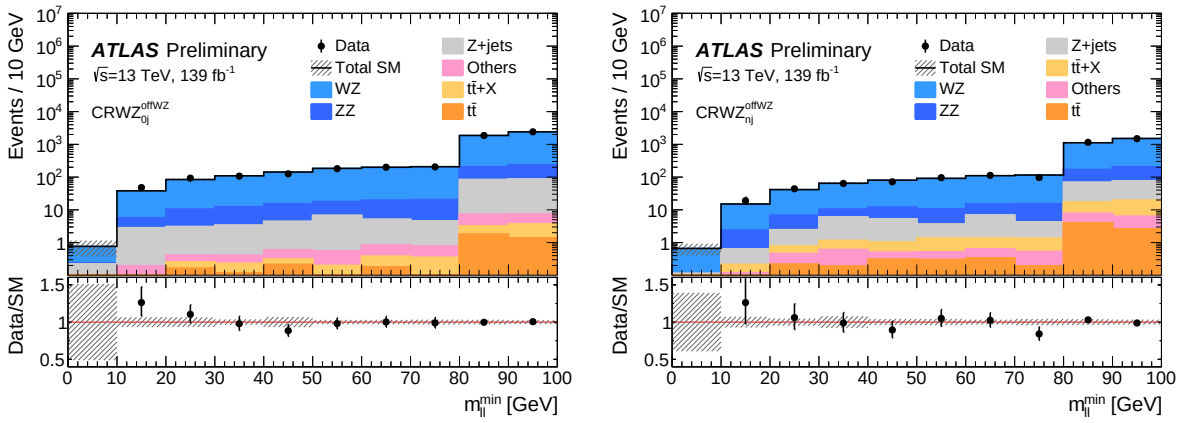

Figure 8: Distribution of $m_{\ell\ell}^{\mathrm{min}}$ after the background-only fit, showing the data and the post-fit expected background, in (left) $\texttt{CRWZ}^{\texttt{offWZ}}_{\texttt{0j}}$ and (right) $\texttt{CRWZ}^{\texttt{offWZ}}_{\texttt{nj}}$. The first (last) bin includes underflow (overflow). The "Others" category contains backgrounds from single-top, WW, triboson, Higgs and rare top processes. The bottom panel shows the ratio of the observed data to the predicted yields. The hatched bands indicate the combined theoretical, experimental, and MC statistical uncertainties.

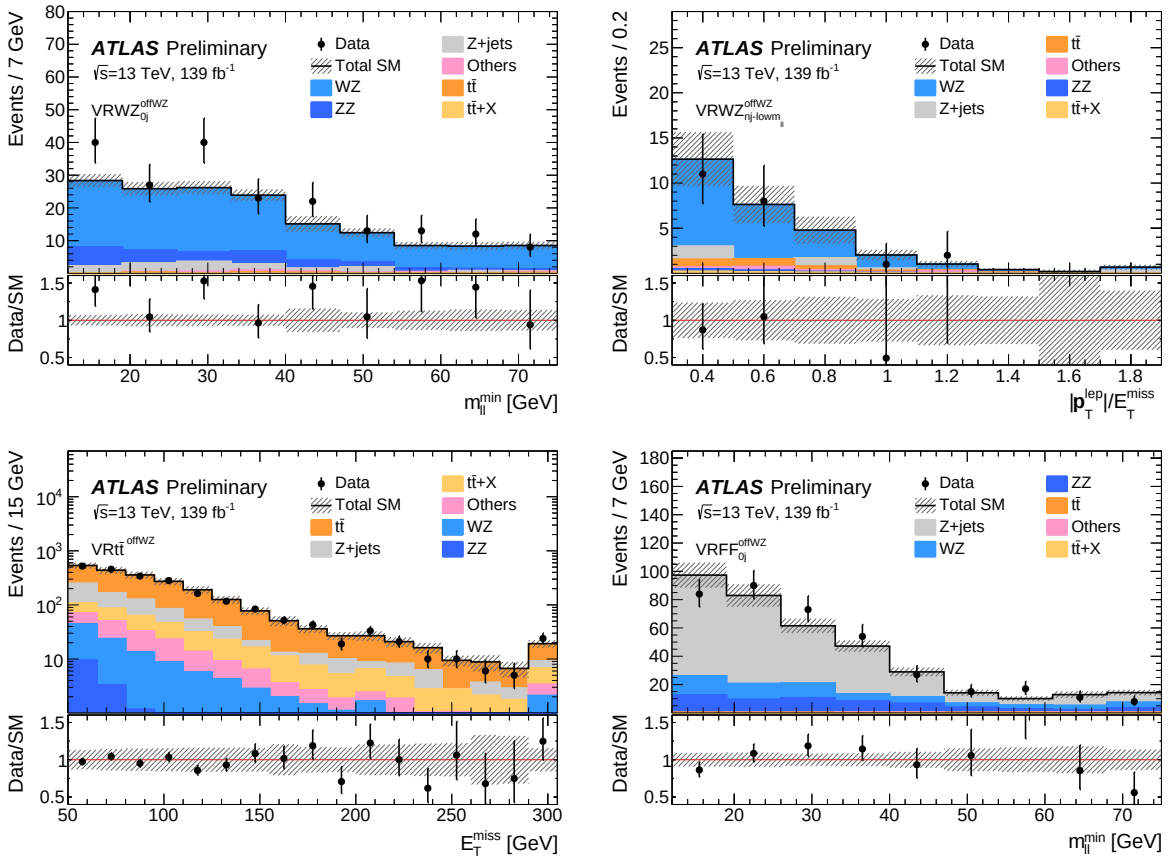

Figure 9: Example of kinematic distributions after the background-only fit, showing the data and the post-fit expected background, in regions of the off-shell WZ selection. The figure shows (top left) the $m_{\ell\ell}^{\text{min}}$ distribution in $\texttt{VRWZ}_{0j}^{\texttt{offWZ}}$, (top right) the $|\mathbf{p}_{\text{T}}^{\text{lep}}|/E_{\text{T}}^{\text{miss}}$ distribution in $\texttt{VRWZ}_{\texttt{nj-lowm}_{11}}^{\texttt{offWZ}}$, (bottom left) the $E_{\text{T}}^{\text{miss}}$ distribution in $\texttt{VRtt}^{\texttt{offWZ}}$, and (bottom right), the $m_{\ell\ell}^{\text{min}}$ distribution in $\texttt{VRFF}_{0j}^{\texttt{offWZ}}$. The first (last) bin includes underflow (overflow). The "Others" category contains backgrounds from single-top, WW, triboson, Higgs and rare top processes. The bottom panel shows the ratio of the observed data to the predicted yields. The hatched bands indicate the combined theoretical, experimental, and MC statistical uncertainties. The slope change in the bottom left $E_{\text{T}}^{\text{miss}}$ distribution also illustrates the selection extension with $E_{\text{T}}^{\text{miss}}$ triggered events, which start contributing at $E_{\text{T}}^{\text{miss}} \gtrsim 200$ GeV.

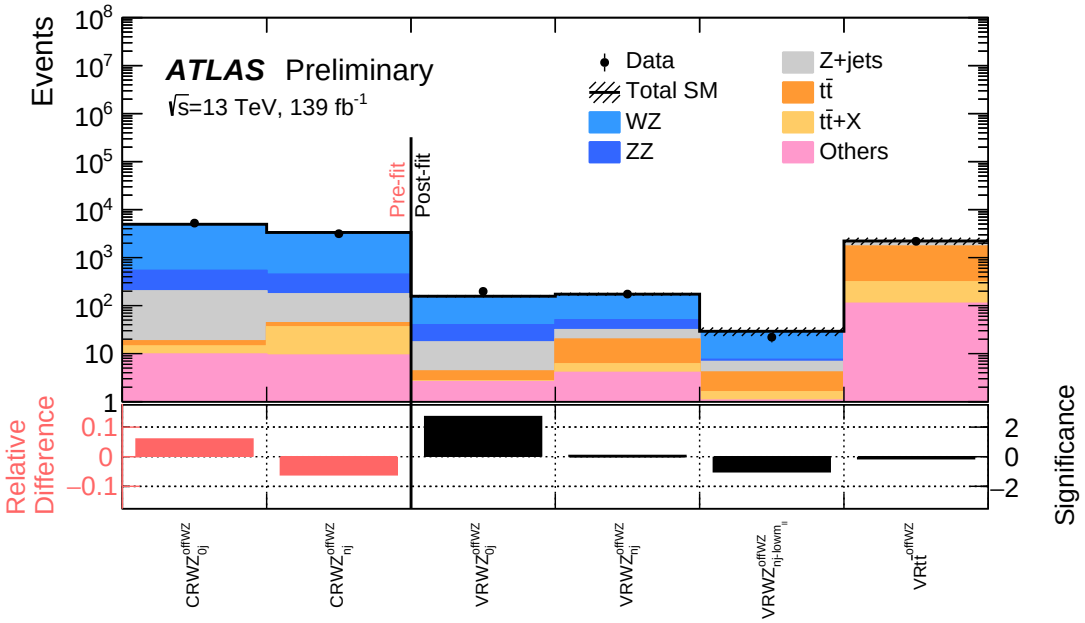

Figure 10: Comparison of the observed data and expected SM background yields in the CRs and VRs of the off-shell *WZ* selection. The SM prediction is taken from the background-only fit. The "Others category contains the single-top, WW, triboson, Higgs and rare top processes. The hatched band indicates the combined theoretical, experimental, and MC statistical uncertainties. The bottom panel shows the significance of the difference between the observed and expected yields, calculated with the profile likelihood method from [135], adding a minus sign if the yield is below the prediction.

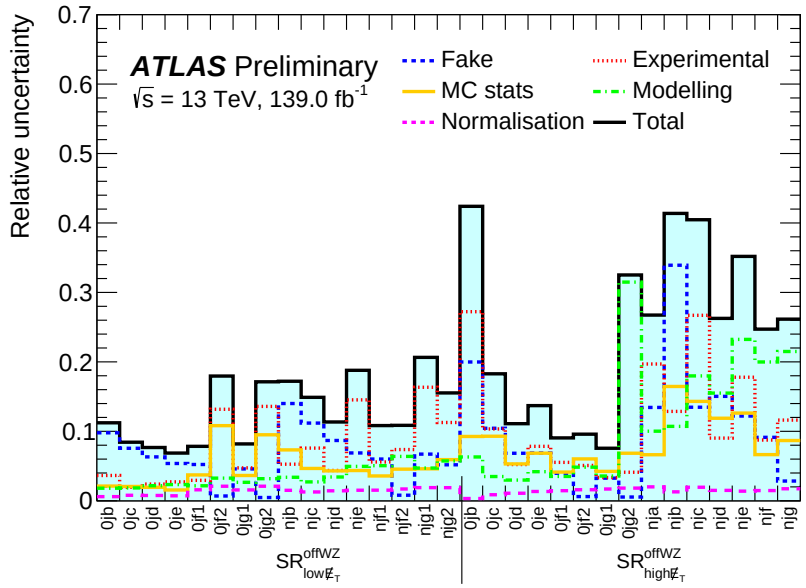

Figure 11: Breakdown of the systematic uncertainties in the event yields in the SRs of the off-shell *WZ* selection.

8 Results

The observed data in the SRs is compared with the background expectation obtained by the two background-only fits described in Section 5.2. The results are summarised in Tables 12–13 as well as visualised in Figures 12-13 for the $\mathrm{SR}^{\mathtt{WZ}}$ and $\mathrm{SR}^{\mathtt{Wh}}$ regions, and in Table 14-15 and Figure 14 for the $\mathrm{SR}^{\mathtt{offWZ}}$.

To illustrate the sensitivity to various $\widetilde{\chi}_1^{\pm}\widetilde{\chi}_2^0$ signals throughout the regions, representative signal MC predictions are overlaid on the figures. The sensitivity to WZ-mediated models, when the mass difference between the $\tilde{\chi}_1^{\pm}/\tilde{\chi}_2^0$ and $\tilde{\chi}_1^0$ is large, is driven by the $\mathrm{SR}^{\mathtt{WZ}}$ with large m_{T} and $E_{\mathrm{T}}^{\mathrm{miss}}$ values. On the other hand, when the mass splitting is close to the Z-boson mass, the sensitivity is dominated by the high H_{T} region and moderate m_{T} and $E_{\mathrm{T}}^{\mathrm{miss}}$ bins of the $n_{\mathrm{jets}} = 0$ and low H_{T} regions. For the Wh-mediated scenarios the sensitivity is driven by $\mathrm{SR}^{\mathtt{Wh}}_{\mathtt{SFOS}}$ and $\mathrm{SR}^{\mathtt{Wh}}_{\mathtt{DFOS}}$ regions, with $\mathrm{SR}^{\mathtt{Wh}}_{\mathtt{DFOS}}$-1 contributing the most.

Table 12: Observed and expected yields after the background-only fit in the SRs for the on-shell WZ selection. The normalization factors of the WZ sample are extracted separately for the 0j, low-H_{T} and high-H_{T} regions, and are treated separately in the combined fit. The "Others" category contains the single-top, WW, triboson, Higgs and rare top processes. Combined statistical and systematic uncertainties are presented.

Regions	$\mathrm{SR}^{\mathtt{WZ}}$-1	$\mathrm{SR}^{\mathtt{WZ}}$-2	$\mathrm{SR}^{\mathtt{WZ}}$-3	$\mathrm{SR}^{\mathtt{WZ}}$-4	$\mathrm{SR}^{\mathtt{WZ}}$-5	$\mathrm{SR}^{\mathtt{WZ}}$-6	$\mathrm{SR}^{\mathtt{WZ}}$-7
Observed	331	31	3	2	42	7	3
Fitted SM	314 ± 33	35 ± 6	4.1 ± 1.0	1.2 ± 0.5	58 ± 5	8.0 ± 0.9	5.8 ± 1.0
WZ	294 ± 31	32 ± 5	3.7 ± 0.9	0.9 ± 0.5	48 ± 4	7.1 ± 0.8	5.0 ± 0.9
ZZ	12.1 ± 3.1	0.66 ± 0.35	0.08 ± 0.04	0.04 ± 0.02	2.3 ± 0.6	0.12 ± 0.04	0.08 ± 0.03
$t\bar{t}$	2.8 ± 0.8	0.36 ± 0.26	0.04 ± 0.01	$0.00\pm^{0.01}_{0.00}$	1.4 ± 0.4	$0.00\pm^{0.01}_{0.00}$	0.04 ± 0.02
Z+jets	0.01 ± 0.01	0.14 ± 0.14	0.05 ± 0.06	0.06 ± 0.04	2.8 ± 2.3	0.3 ± 0.4	0.26 ± 0.17
$t\bar{t}$ +X	0.16 ± 0.06	0.13 ± 0.05	0.03 ± 0.04	0.01 ± 0.01	0.10 ± 0.06	0.05 ± 0.03	0.01 ± 0.01
Others	5.1 ± 0.8	1.1 ± 0.4	0.21 ± 0.06	0.17 ± 0.06	3.2 ± 0.5	0.38 ± 0.11	0.34 ± 0.10

Regions	$\mathrm{SR}^{\mathtt{WZ}}$-8	$\mathrm{SR}^{\mathtt{WZ}}$-9	$\mathrm{SR}^{\mathtt{WZ}}$-10	$\mathrm{SR}^{\mathtt{WZ}}$-11	$\mathrm{SR}^{\mathtt{WZ}}$-12	$\mathrm{SR}^{\mathtt{WZ}}$-13	$\mathrm{SR}^{\mathtt{WZ}}$-14
Observed	1	77	11	0	0	111	19
Fitted SM	0.8 ± 0.4	90 ± 19	13.4 ± 2.4	0.5 ± 0.4	0.49 ± 0.24	89 ± 11	16.0 ± 1.4
WZ	0.44 ± 0.32	77 ± 18	11.3 ± 2.4	0.37 ± 0.31	0.38 ± 0.22	72 ± 9	13.4 ± 1.3
ZZ	0.01 ± 0.01	1.9 ± 0.9	0.24 ± 0.13	0.01 ± 0.01	0.01 ± 0.01	5.8 ± 2.8	0.39 ± 0.18
$t\bar{t}$	$0.00\pm^{0.01}_{0.00}$	3.3 ± 0.9	0.45 ± 0.28	$0.00\pm^{0.01}_{0.00}$	$0.00\pm^{0.01}_{0.00}$	6.0 ± 1.4	0.24 ± 0.17
Z+jets	0.28 ± 0.20	4 ± 5	0.2 ± 0.4	0.02 ± 0.03	0.02 ± 0.03	0.02 ± 0.03	0.02 ± 0.03
$t\bar{t}$ +X	0 ± 0	1.3 ± 0.4	0.40 ± 0.14	0.05 ± 0.04	0.02 ± 0.01	1.6 ± 0.5	0.56 ± 0.16
Others	0.08 ± 0.06	2.3 ± 0.5	0.79 ± 0.22	0.08 ± 0.05	0.08 ± 0.03	3.5 ± 0.7	1.37 ± 0.33

Regions	$\mathrm{SR}^{\mathtt{WZ}}$-15	$\mathrm{SR}^{\mathtt{WZ}}$-16	$\mathrm{SR}^{\mathtt{WZ}}$-17	$\mathrm{SR}^{\mathtt{WZ}}$-18	$\mathrm{SR}^{\mathtt{WZ}}$-19	$\mathrm{SR}^{\mathtt{WZ}}$-20
Observed	5	1	13	9	3	1
Fitted SM	2.8 ± 0.6	1.30 ± 0.28	14 ± 6	9.2 ± 3.5	2.3 ± 0.9	1.1 ± 0.5
WZ	2.3 ± 0.6	1.07 ± 0.24	10 ± 5	6.7 ± 3.4	1.6 ± 0.8	0.9 ± 0.5
ZZ	0.07 ± 0.04	0.04 ± 0.03	0.13 ± 0.06	0.10 ± 0.04	0.02 ± 0.01	0.02 ± 0.01
$t\bar{t}$	$0.00\pm^{0.01}_{0.00}$	$0.00\pm^{0.01}_{0.00}$	0.77 ± 0.32	0.45 ± 0.26	$0.00\pm^{0.01}_{0.00}$	$0.00\pm^{0.01}_{0.00}$
Z+jets	0.02 ± 0.02	0.07 ± 0.08	1 ± 1	0.7 ± 1.0	0.25 ± 0.34	0.02 ± 0.02
$t\bar{t}$ +X	0.07 ± 0.03	$0.00^{0.03}_{0.00}$	0.53 ± 0.17	0.33 ± 0.10	0.07 ± 0.04	0.03 ± 0.02
Others	0.37 ± 0.11	0.12 ± 0.04	1.1 ± 0.8	0.9 ± 0.7	0.27 ± 0.07	0.18 ± 0.05

For the WZ-mediated models targeted with the $\mathrm{SR}^{\mathtt{offWZ}}$, with mass differences between the $\tilde{\chi}_1^{\pm}/\tilde{\chi}_2^0$ and $\tilde{\chi}_1^0$ smaller than the Z-boson mass, the sensitivity to signals with different Δm depends on the $m_{\ell\ell}^{\mathrm{min}}$ range of the bins. The bins with larger (smaller) $m_{\ell\ell}^{\mathrm{min}}$ values are sensitive to signals with larger (smaller) mass splittings; for the lowest mass splitting signals, only $\mathrm{SR}^{\mathtt{offWZ}}_{\mathtt{high}\not{E}_{\mathrm{T}}}\mathtt{-nja}$ has sensitivity.

No significant excesses are observed in any of the SRs. The maximum deviation of the data from the background expectation is in $\mathrm{SR}^{\mathtt{offWZ}}_{\mathtt{low}\not{E}_{\mathrm{T}}}\mathtt{-0jd}$ with a 2.3 σ data excess, followed by a 2.1 σ deficit in $\mathrm{SR}^{\mathtt{offWZ}}_{\mathtt{high}\not{E}_{\mathrm{T}}}\mathtt{-0jf2}$, a 2.0 σ excess in $\mathrm{SR}^{\mathtt{Wh}}_{\mathtt{DFOS}}\mathtt{-1}$, and a 2.0 σ deficit in $\mathrm{SR}^{\mathtt{WZ}}\mathtt{-5}$; the significance are computed following the profile likelihood method in [135].

Post-fit distributions of key kinematic observables for the $\mathrm{SR}^{\mathtt{WZ}}$ and $\mathrm{SR}^{\mathtt{Wh}}$ regions are shown in Figure 15, including signal MC predictions for two representative mass points. The data are compatible with the prediction within systematic uncertainties in all SRs except $\mathrm{SR}^{\mathtt{Wh}}_{\mathtt{DFOS}}\mathtt{-1}$, where a 2.0$\sigma$ deviation is observed. Similar distributions are shown for the $\mathrm{SR}^{\mathtt{offWZ}}$ regions in Figure 16. The overall agreement of the data with the prediction is reasonable, and none of the deviations agree with any of the benchmark signal hypotheses.

Table 13: Observed and expected yields after the background-only fit in the SRs for the Wh selection. The normalization factors of the WZ sample are extracted separately for the $\mathtt{0j}$, $\mathtt{low}\text{-}H_{\mathrm{T}}$ and $\mathtt{high}\text{-}H_{\mathrm{T}}$ regions, and are treated separately in the combined fit. The "Others" category contains the single-top, WW, $t\bar{t}$ +X and rare top processes. Combined statistical and systematic uncertainties are presented.

Regions	$\mathrm{SR}^{\mathtt{Wh}}_{\mathtt{SFOS}}\mathtt{-1}$	$\mathrm{SR}^{\mathtt{Wh}}_{\mathtt{SFOS}}\mathtt{-2}$	$\mathrm{SR}^{\mathtt{Wh}}_{\mathtt{SFOS}}\mathtt{-3}$	$\mathrm{SR}^{\mathtt{Wh}}_{\mathtt{SFOS}}\mathtt{-4}$	$\mathrm{SR}^{\mathtt{Wh}}_{\mathtt{SFOS}}\mathtt{-5}$	$\mathrm{SR}^{\mathtt{Wh}}_{\mathtt{SFOS}}\mathtt{-6}$	$\mathrm{SR}^{\mathtt{Wh}}_{\mathtt{SFOS}}\mathtt{-7}$
Observed	152	14	8	47	6	15	19
Fitted SM	136 ± 13	13.5 ± 1.7	4.3 ± 0.9	50 ± 5	4.3 ± 0.7	20.2 ± 2.1	16.0 ± 2.1
WZ	107 ± 12	10.2 ± 1.7	3.8 ± 0.8	32 ± 4	2.7 ± 0.6	12.3 ± 1.6	10.8 ± 1.7
$t\bar{t}$	10.3 ± 2.5	1.6 ± 0.6	0.13 ± 0.12	7.7 ± 1.9	0.74 ± 0.34	3.5 ± 1.0	2.5 ± 0.7
Z+jets	2.5 ± 2.9	$0.00\pm^{0.02}_{0.00}$	$0.00\pm^{0.02}_{0.00}$	2.0 ± 1.6	$0.00\pm^{0.04}_{0.00}$	$0.00\pm^{0.04}_{0.00}$	$0.00\pm^{0.02}_{0.00}$
Higgs	5.7 ± 0.6	0.69 ± 0.07	0.20 ± 0.03	3.12 ± 0.31	0.26 ± 0.05	1.29 ± 0.14	0.81 ± 0.09
VVV	1.9 ± 0.5	0.22 ± 0.07	0.07 ± 0.02	1.4 ± 0.4	0.28 ± 0.09	0.61 ± 0.18	0.83 ± 0.24
Others	8.6 ± 1.9	0.84 ± 0.11	0.08 ± 0.05	4.0 ± 0.5	0.23 ± 0.24	2.54 ± 0.22	1.11 ± 0.15

Regions	$\mathrm{SR}^{\mathtt{Wh}}_{\mathtt{SFOS}}\mathtt{-8}$	$\mathrm{SR}^{\mathtt{Wh}}_{\mathtt{SFOS}}\mathtt{-9}$	$\mathrm{SR}^{\mathtt{Wh}}_{\mathtt{SFOS}}\mathtt{-10}$	$\mathrm{SR}^{\mathtt{Wh}}_{\mathtt{SFOS}}\mathtt{-11}$	$\mathrm{SR}^{\mathtt{Wh}}_{\mathtt{SFOS}}\mathtt{-12}$	$\mathrm{SR}^{\mathtt{Wh}}_{\mathtt{SFOS}}\mathtt{-13}$	$\mathrm{SR}^{\mathtt{Wh}}_{\mathtt{SFOS}}\mathtt{-14}$
Observed	113	184	28	5	82	16	4
Fitted SM	108 ± 13	180 ± 17	31 ± 4	6.6 ± 0.9	90 ± 11	18.7 ± 2.6	2.5 ± 0.7
WZ	54 ± 6	127 ± 13	19.3 ± 2.3	5.3 ± 0.8	47 ± 6	6.8 ± 1.7	1.26 ± 0.26
$t\bar{t}$	21 ± 6	33 ± 10	8.2 ± 2.3	0.7 ± 0.5	28 ± 8	8.0 ± 2.2	0.9 ± 0.5
Z+jets	19 ± 10	2.3 ± 1.9	1.0 ± 1.3	0.10 ± 0.21	2.1 ± 3.1	1.2 ± 0.7	$0.00\pm^{0.12}_{0.00}$
Higgs	1.91 ± 0.19	3.63 ± 0.35	0.67 ± 0.06	0.15 ± 0.02	2.98 ± 0.25	0.61 ± 0.07	0.07 ± 0.07
VVV	0.79 ± 0.24	1.4 ± 0.4	0.41 ± 0.13	0.12 ± 0.05	1.6 ± 0.5	0.56 ± 0.18	0.13 ± 0.05
Others	11.1 ± 2.2	12.2 ± 2.2	1.8 ± 0.4	0.22 ± 0.05	9.0 ± 1.1	1.6 ± 0.7	0.10 ± 0.05

Regions	$\mathrm{SR}^{\mathtt{Wh}}_{\mathtt{SFOS}}\mathtt{-15}$	$\mathrm{SR}^{\mathtt{Wh}}_{\mathtt{SFOS}}\mathtt{-16}$	$\mathrm{SR}^{\mathtt{Wh}}_{\mathtt{SFOS}}\mathtt{-17}$	$\mathrm{SR}^{\mathtt{Wh}}_{\mathtt{SFOS}}\mathtt{-18}$	$\mathrm{SR}^{\mathtt{Wh}}_{\mathtt{SFOS}}\mathtt{-19}$	$\mathrm{SR}^{\mathtt{Wh}}_{\mathtt{DFOS}}\mathtt{-1}$	$\mathrm{SR}^{\mathtt{Wh}}_{\mathtt{DFOS}}\mathtt{-2}$
Observed	51	5	37	7	4	10	10
Fitted SM	46 ± 7	9.8 ± 1.6	43 ± 7	12.6 ± 1.7	1.8 ± 0.4	4.5 ± 0.8	7.0 ± 2.3
WZ	18.9 ± 2.2	3.9 ± 0.8	35 ± 6	9.8 ± 1.6	1.44 ± 0.32	0.44 ± 0.14	1.05 ± 0.20
$t\bar{t}$	18 ± 6	3.2 ± 1.3	1.00 ± 0.34	0.33 ± 0.17	$0.00\pm^{0.01}_{0.00}$	1.0 ± 0.6	1.7 ± 1.1
Z+jets	$0.00\pm^{0.12}_{0.00}$	$0.00\pm^{0.12}_{0.00}$	$0.00\pm^{0.12}_{0.00}$	$0.00\pm^{0.12}_{0.00}$	$0.00\pm^{0.12}_{0.00}$	$0.00\pm^{0.20}_{0.00}$	2.5 ± 2.0
Higgs	2.06 ± 0.23	0.36 ± 0.05	1.02 ± 0.12	0.44 ± 0.05	0.05 ± 0.05	1.59 ± 0.22	0.96 ± 0.11
VVV	1.5 ± 0.4	0.53 ± 0.17	2.5 ± 0.7	1.3 ± 0.4	0.2 ± 0.1	0.66 ± 0.15	0.64 ± 0.16
Others	5.0 ± 0.6	1.8 ± 0.5	3.0 ± 0.7	0.73 ± 0.15	0.14 ± 0.05	0.81 ± 0.09	0.21 ± 0.07

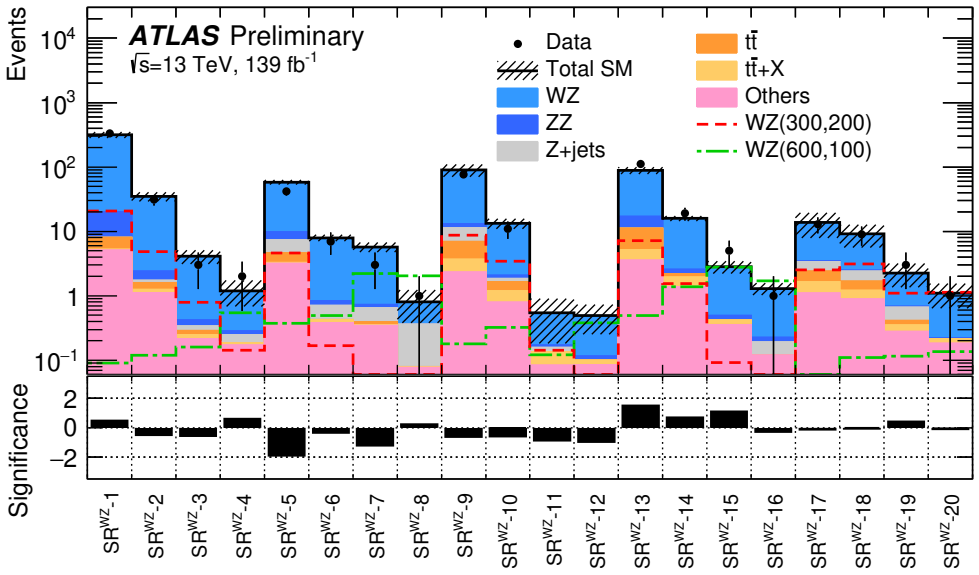

Figure 12: Comparison of the observed data and expected SM background yields in the SRs of the on-shell WZ selection. The SM prediction is taken from the background-only fit. The "Others" category contains the single-top, WW, triboson, Higgs and rare top processes. The hatched band indicates the combined theoretical, experimental, and MC statistical uncertainties. Distributions for $\widetilde{\chi}_1^{\pm}\widetilde{\chi}_2^0 \rightarrow WZ$ signals are overlaid, with mass values given as $(m(\widetilde{\chi}_1^{\pm}), m(\widetilde{\chi}_1^0))$ GeV. The bottom panel shows the significance of the difference between the observed and expected yields, calculated with the profile likelihood method from [135], adding a minus sign if the yield is below the prediction.

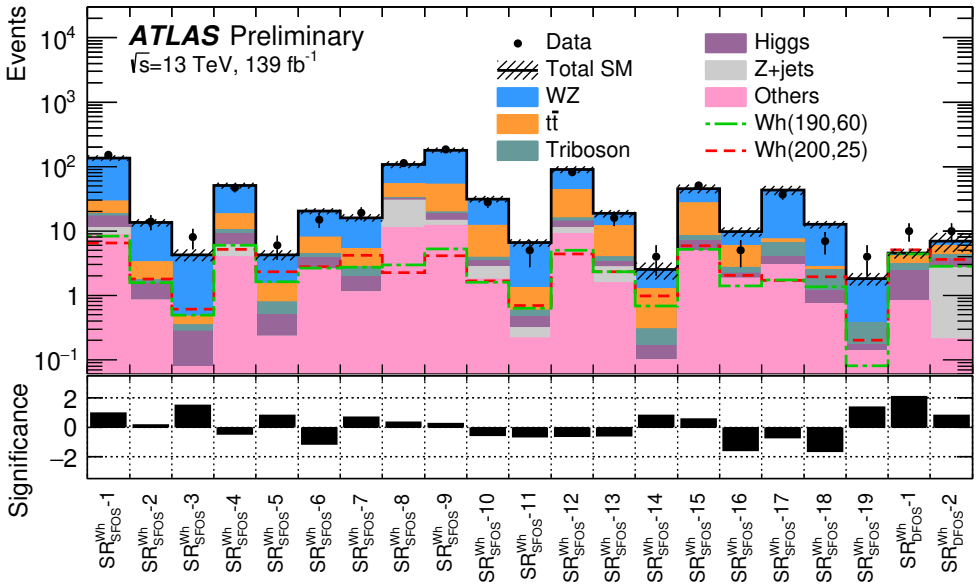

Figure 13: Comparison of the observed data and expected SM background yields in the SRs of the Wh selection. The SM prediction is taken from the background-only fit. The "Others" category contains the single-top, WW, $t\bar{t}$ +X and rare top processes. The hatched band indicates the combined theoretical, experimental, and MC statistical uncertainties. Distributions for $\widetilde{\chi}_1^{\pm}\widetilde{\chi}_2^0 \rightarrow Wh$ signals are overlaid, with mass values given as $(m(\widetilde{\chi}_1^{\pm}), m(\widetilde{\chi}_1^0))$ GeV. The bottom panel shows the significance of the difference between the observed and expected yields, calculated with the profile likelihood method from [135], adding a minus sign if the yield is below the prediction.

Table 14: Observed and expected yields after the background-only fit in $\mathrm{SR}^{\mathrm{offWZ}}_{\mathrm{low}E_{\mathrm{T}}^{\mathrm{miss}}}$. The normalization factors of the *WZ* sample extracted separately for 0j and nj, and are treated separately in the combined fit. The "Others" category contains the single-top, WW, triboson, Higgs and rare top processes. Combined statistical and systematic uncertainties are presented.

Region	$\mathrm{SR}^{\mathrm{offWZ}}_{\mathrm{low}E_{\mathrm{T}}^{\mathrm{miss}}}$-0jb	$\mathrm{SR}^{\mathrm{offWZ}}_{\mathrm{low}E_{\mathrm{T}}^{\mathrm{miss}}}$-0jc	$\mathrm{SR}^{\mathrm{offWZ}}_{\mathrm{low}E_{\mathrm{T}}^{\mathrm{miss}}}$-0jd	$\mathrm{SR}^{\mathrm{offWZ}}_{\mathrm{low}E_{\mathrm{T}}^{\mathrm{miss}}}$-0je	$\mathrm{SR}^{\mathrm{offWZ}}_{\mathrm{low}E_{\mathrm{T}}^{\mathrm{miss}}}$-0jf1	$\mathrm{SR}^{\mathrm{offWZ}}_{\mathrm{low}E_{\mathrm{T}}^{\mathrm{miss}}}$-0jf2
Observed	25	42	77	101	33	7
Fitted SM events	32 ± 4	44 ± 4	54 ± 4	91 ± 6	32.2 ± 2.5	5.9 ± 1.1
WZ	7.6 ± 0.9	13.8 ± 1.3	16.3 ± 1.9	25.6 ± 1.8	20.1 ± 1.5	4.9 ± 1.0
ZZ	5.5 ± 1.3	7.4 ± 1.2	9.6 ± 1.6	21.8 ± 3.2	2.7 ± 1.1	0.43 ± 0.14
Z+jets	19.1 ± 3.2	22.7 ± 3.4	26.5 ± 3.5	40 ± 5	7.2 ± 1.7	$0.00 \pm {}^{0.04}_{0.00}$
$t\bar{t}$	$0.05 \pm {}^{0.18}_{0.05}$	$0.11 \pm {}^{0.17}_{0.11}$	0.38 ± 0.22	1.1 ± 0.4	0.78 ± 0.29	$0.08 \pm {}^{0.10}_{0.08}$
$t\bar{t} + X$	$0.007 \pm {}^{0.019}_{0.007}$	$0.002 \pm {}^{0.008}_{0.002}$	$0.009 \pm {}^{0.019}_{0.009}$	$0.019 \pm {}^{0.026}_{0.019}$	$0.026 \pm {}^{0.026}_{0.026}$	$0.010 \pm {}^{0.015}_{0.010}$
Others	0.045 ± 0.031	0.30 ± 0.12	1.3 ± 0.6	1.9 ± 0.6	1.4 ± 0.4	0.51 ± 0.18

Region	$\mathrm{SR}^{\mathrm{offWZ}}_{\mathrm{low}E_{\mathrm{T}}^{\mathrm{miss}}}$-0jg1	$\mathrm{SR}^{\mathrm{offWZ}}_{\mathrm{low}E_{\mathrm{T}}^{\mathrm{miss}}}$-0jg2	$\mathrm{SR}^{\mathrm{offWZ}}_{\mathrm{low}E_{\mathrm{T}}^{\mathrm{miss}}}$-njb	$\mathrm{SR}^{\mathrm{offWZ}}_{\mathrm{low}E_{\mathrm{T}}^{\mathrm{miss}}}$-njc	$\mathrm{SR}^{\mathrm{offWZ}}_{\mathrm{low}E_{\mathrm{T}}^{\mathrm{miss}}}$-njd	$\mathrm{SR}^{\mathrm{offWZ}}_{\mathrm{low}E_{\mathrm{T}}^{\mathrm{miss}}}$-nje
Observed	34	9	6	13	17	14
Fitted SM events	34.7 ± 2.8	6.3 ± 1.1	3.5 ± 0.6	8.0 ± 1.2	13.5 ± 1.5	18.2 ± 3.4
WZ	21.4 ± 2.1	5.2 ± 1.0	1.62 ± 0.30	3.2 ± 0.6	6.0 ± 0.8	8.6 ± 1.3
ZZ	4.7 ± 1.4	0.45 ± 0.14	0.45 ± 0.13	0.72 ± 0.22	1.00 ± 0.28	1.4 ± 0.9
Z+jets	6.6 ± 1.6	$0.001 \pm {}^{0.029}_{0.001}$	1.2 ± 0.5	3.7 ± 0.9	4.5 ± 1.2	3.3 ± 1.3
$t\bar{t}$	0.8 ± 0.4	0.36 ± 0.21	0.15 ± 0.13	0.28 ± 0.14	1.5 ± 0.4	3.3 ± 0.9
$t\bar{t} + X$	0.039 ± 0.025	$0.003 \pm {}^{0.008}_{0.003}$	0.030 ± 0.013	0.052 ± 0.019	0.24 ± 0.06	0.33 ± 0.07
Others	1.16 ± 0.27	0.27 ± 0.09	0.006 ± 0.004	$0.14 \pm {}^{0.34}_{0.14}$	0.21 ± 0.06	$1.3 \pm {}^{1.8}_{1.3}$

Region	$\mathrm{SR}^{\mathrm{offWZ}}_{\mathrm{low}E_{\mathrm{T}}^{\mathrm{miss}}}$-njf1	$\mathrm{SR}^{\mathrm{offWZ}}_{\mathrm{low}E_{\mathrm{T}}^{\mathrm{miss}}}$-njf2	$\mathrm{SR}^{\mathrm{offWZ}}_{\mathrm{low}E_{\mathrm{T}}^{\mathrm{miss}}}$-njg1	$\mathrm{SR}^{\mathrm{offWZ}}_{\mathrm{low}E_{\mathrm{T}}^{\mathrm{miss}}}$-njg2
Observed	25	20	22	12
Fitted SM events	23.4 ± 2.5	17.9 ± 1.9	17.0 ± 3.5	12.4 ± 1.9
WZ	11.1 ± 1.2	9.4 ± 1.1	10.0 ± 1.2	7.3 ± 1.3
ZZ	4.0 ± 1.6	0.66 ± 0.25	$1.1 \pm {}^{2.6}_{1.1}$	0.34 ± 0.11
Z+jets	2.2 ± 1.4	$0.00 \pm {}^{0.14}_{0.00}$	1.8 ± 1.1	$0.0 \pm {}^{0.6}_{0.0}$
$t\bar{t}$	4.6 ± 1.1	5.7 ± 1.2	3.0 ± 0.8	2.9 ± 0.7
$t\bar{t} + X$	0.44 ± 0.09	0.72 ± 0.11	0.36 ± 0.08	0.44 ± 0.09
Others	1.0 ± 0.4	1.4 ± 0.9	0.71 ± 0.21	1.4 ± 0.6

Table 15: Observed and expected yields after the background-only fit in $\mathrm{SR}^{\mathrm{offWZ}}_{\mathrm{high}\not{E}_{\mathrm{T}}}$. The normalization factors of the WZ sample extracted separately for 0j and nj, and are treated separately in the combined fit. The "Others" category contains the single-top, WW, triboson, Higgs and rare top processes. Combined statistical and systematic uncertainties are presented.

Region	$\mathrm{SR}^{\mathrm{offWZ}}_{\mathrm{high}\not{E}_{\mathrm{T}}}$-0jb	$\mathrm{SR}^{\mathrm{offWZ}}_{\mathrm{high}\not{E}_{\mathrm{T}}}$-0jc	$\mathrm{SR}^{\mathrm{offWZ}}_{\mathrm{high}\not{E}_{\mathrm{T}}}$-0jd	$\mathrm{SR}^{\mathrm{offWZ}}_{\mathrm{high}\not{E}_{\mathrm{T}}}$-0je	$\mathrm{SR}^{\mathrm{offWZ}}_{\mathrm{high}\not{E}_{\mathrm{T}}}$-0jf1
Observed	1	4	11	13	37
Fitted SM events	1.5 ± 0.7	4.3 ± 0.8	14.0 ± 1.6	11.5 ± 1.6	35.7 ± 3.2
WZ	$0.20 \pm {}^{0.27}_{0.20}$	1.5 ± 0.5	6.0 ± 0.9	6.1 ± 1.1	20.5 ± 2.1
ZZ	$0.5 \pm {}^{0.5}_{0.5}$	0.31 ± 0.12	1.8 ± 0.8	0.89 ± 0.24	3.1 ± 1.0
Z+jets	0.81 ± 0.31	1.7 ± 0.4	4.4 ± 1.0	1.1 ± 0.8	4.3 ± 1.4
$t\bar{t}$	$0.05 \pm {}^{0.05}_{0.05}$	0.45 ± 0.17	0.64 ± 0.28	1.8 ± 0.6	4.4 ± 1.0
$t\bar{t}+X$	$0.003 \pm {}^{0.014}_{0.003}$	$0.009 \pm {}^{0.013}_{0.009}$	0.029 ± 0.015	0.08 ± 0.04	0.11 ± 0.05
Others	$0.014 \pm {}^{0.018}_{0.014}$	$0.3 \pm {}^{0.4}_{0.3}$	1.1 ± 0.4	1.6 ± 0.4	3.3 ± 0.8

Region	$\mathrm{SR}^{\mathrm{offWZ}}_{\mathrm{high}\not{E}_{\mathrm{T}}}$-0jf2	$\mathrm{SR}^{\mathrm{offWZ}}_{\mathrm{high}\not{E}_{\mathrm{T}}}$-0jg1	$\mathrm{SR}^{\mathrm{offWZ}}_{\mathrm{high}\not{E}_{\mathrm{T}}}$-0jg2	$\mathrm{SR}^{\mathrm{offWZ}}_{\mathrm{high}\not{E}_{\mathrm{T}}}$-nja	$\mathrm{SR}^{\mathrm{offWZ}}_{\mathrm{high}\not{E}_{\mathrm{T}}}$-njb
Observed	14	43	17	3	2
Fitted SM events	25.5 ± 2.4	39.5 ± 3.0	21 ± 7	6.0 ± 1.6	1.4 ± 0.6
WZ	16.0 ± 2.3	26.4 ± 2.2	15 ± 7	3.8 ± 1.2	0.57 ± 0.18
ZZ	0.95 ± 0.35	3.0 ± 0.9	0.58 ± 0.17	0.044 ± 0.023	0.009 ± 0.005
Z+jets	$0.00 \pm {}^{0.15}_{0.00}$	3.4 ± 1.3	$0.00 \pm {}^{0.11}_{0.00}$	1.5 ± 0.8	$0.5 \pm {}^{0.5}_{0.5}$
$t\bar{t}$	4.4 ± 1.0	4.3 ± 0.9	3.1 ± 0.7	0.6 ± 0.5	$0.14 \pm {}^{0.15}_{0.14}$
$t\bar{t}+X$	0.109 ± 0.030	0.16 ± 0.05	0.09 ± 0.04	0.16 ± 0.06	$0.014 \pm {}^{0.025}_{0.014}$
Others	4.0 ± 1.0	2.3 ± 0.8	2.0 ± 0.5	0.038 ± 0.030	$0.22 \pm {}^{0.22}_{0.22}$

Region	$\mathrm{SR}^{\mathrm{offWZ}}_{\mathrm{high}\not{E}_{\mathrm{T}}}$-njc	$\mathrm{SR}^{\mathrm{offWZ}}_{\mathrm{high}\not{E}_{\mathrm{T}}}$-njd	$\mathrm{SR}^{\mathrm{offWZ}}_{\mathrm{high}\not{E}_{\mathrm{T}}}$-nje	$\mathrm{SR}^{\mathrm{offWZ}}_{\mathrm{high}\not{E}_{\mathrm{T}}}$-njf	$\mathrm{SR}^{\mathrm{offWZ}}_{\mathrm{high}\not{E}_{\mathrm{T}}}$-njg
Observed	2	2	2	11	4
Fitted SM events	2.1 ± 0.8	5.4 ± 1.4	3.0 ± 1.1	9.9 ± 2.5	6.8 ± 1.8
WZ	1.25 ± 0.25	2.5 ± 0.4	1.31 ± 0.25	4.5 ± 0.7	3.7 ± 0.6
ZZ	0.020 ± 0.011	0.014 ± 0.013	0.029 ± 0.014	0.081 ± 0.033	0.050 ± 0.020
Z+jets	$0.04 \pm {}^{0.28}_{0.04}$	$0.7 \pm {}^{0.8}_{0.7}$	$0.0 \pm {}^{0.4}_{0.0}$	$0.6 \pm {}^{0.9}_{0.6}$	$0.00 \pm {}^{0.19}_{0.00}$
$t\bar{t}$	0.6 ± 0.5	1.3 ± 0.8	1.2 ± 1.0	3.4 ± 2.0	2.5 ± 1.6
$t\bar{t}+X$	0.027 ± 0.023	$0.08 \pm {}^{0.08}_{0.08}$	0.09 ± 0.04	0.31 ± 0.08	0.21 ± 0.07
Others	$0.14 \pm {}^{0.36}_{0.14}$	0.8 ± 0.6	0.33 ± 0.21	1.0 ± 0.4	$0.3 \pm {}^{0.4}_{0.3}$

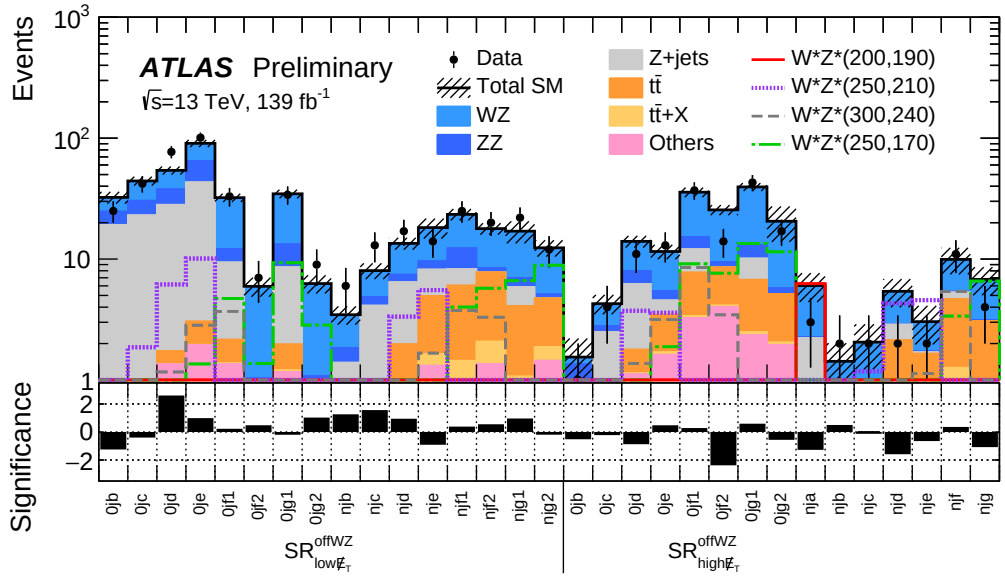

Figure 14: Comparison of the observed data and expected SM background yields in the SRs of the off-shell WZ selection. The SM prediction is taken from the background-only fit. The "Others" category contains the single-top, WW, triboson, Higgs and rare top processes. The hatched band indicates the combined theoretical, experimental, and MC statistical uncertainties. Distributions for $\widetilde{\chi}_1^{\pm}\widetilde{\chi}_2^0 \to W^*Z^*$ signals are overlaid, with mass values given as $(m(\widetilde{\chi}_1^{\pm}), m(\widetilde{\chi}_1^0))$ GeV. The bottom panel shows the significance of the difference between the observed and expected yields, calculated with the profile likelihood method from [135], adding a minus sign if the yield is below the prediction.

8.1 Model-independent limits on new physics in inclusive regions

Model-independent upper limits and discovery p-values in the SRs are derived performing the discovery fits as described in Section 5.4. The set of single-bin signal regions used in the fits, referred to as "inclusive SRs", is constructed by logically grouping adjoining, disjoint, nominal SRs of the on-shell WZ, Wh and off-shell WZ selections. Multiple, sometimes overlapping, regions are defined to capture signatures with different unknown $m_{\ell\ell}^{\text{min}}$ shapes and jet multiplicities inclusively. Based on best expected discovery sensitivity and using a number of signal points covering both WZ- and Wh-mediated scenarios and different mass splittings, twelve inclusive SRs are set up merging $\texttt{SR}^{\texttt{WZ}}$ and $\texttt{SR}^{\texttt{Wh}}$ regions, creating $\texttt{incSR}^{\texttt{WZ}}$ and $\texttt{incSR}^{\texttt{Wh}}$, respectively. They are summarised in Table 16. Similarly, 17 inclusive SRs are set up merging $\texttt{SR}^{\texttt{offWZ}}$ regions, creating $\texttt{incSR}^{\texttt{offWZ}}$; their definitions are summarised in Table 17. For $\texttt{incSR}^{\texttt{offWZ}}$, contiguous jet-veto regions are merged together with jet-inclusive regions, as the $m_{\ell\ell}^{\text{min}}$ shape of a signal is assumed to be insensitive to jet multiplicity. The $\texttt{SR}^{\texttt{offWZ}}_{\text{low}E_{\text{T}}^{\text{miss}}}$ and $\texttt{SR}^{\texttt{offWZ}}_{\text{high}E_{\text{T}}^{\text{miss}}}$ regions are kept separate, while the $\texttt{SR}^{\texttt{offWZ}}_{\text{high}E_{\text{T}}^{\text{miss}}}\texttt{-nj}$ regions are considered separately for $m_{\ell\ell}^{\text{min}} < 20$ GeV, as this selection provides the best sensitivity to low-mass-splitting models.

The 95% CL upper limits on the generic BSM cross section are calculated by performing a discovery fit for each target SR and its associated CRs.

Results are reported in Table 18 (19) for the on-shell WZ and Wh analysis selections (off-shell WZ selection). The tables list the observed (N_{obs}) and expected (N_{obs}) yields in the inclusive SRs, the upper limits on the observed (S_{obs}^{95}) and expected (S_{exp}^{95}) number of BSM events, and the visible cross section (σ_{vis}^{95}) reflecting the product of the production cross section, the acceptance, and the selection efficiency for a BSM process; the p-value and significance (Z) for the background-only hypothesis are also presented.

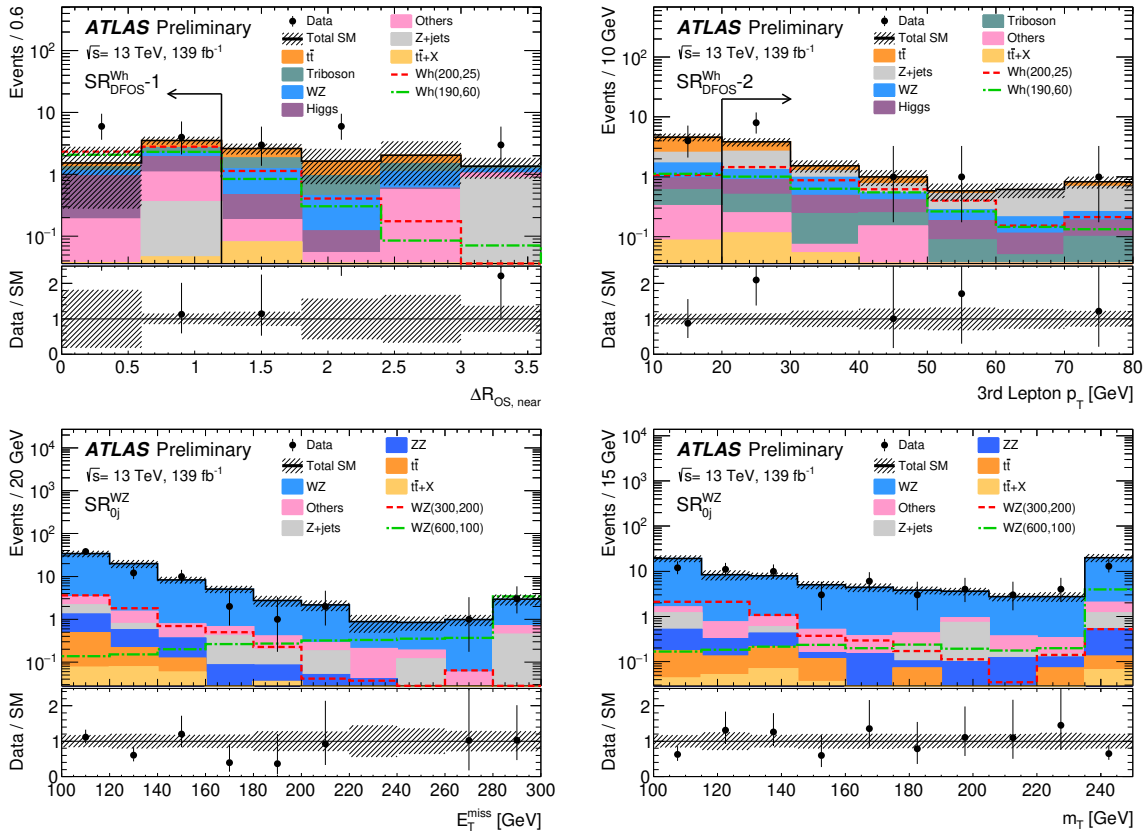

Figure 15: Kinematic distributions after the background-only fit showing the data and the post-fit expected background, in SRs of the on-shell WZ and Wh selections. The figure shows (top left) the $\Delta R_{\mathrm{OS,near}}$ distribution in $\mathrm{SR}^{\mathrm{Wh}}_{\mathrm{DFOS}}$-1, (top right) the 3rd leading lepton p_{T} in $\mathrm{SR}^{\mathrm{Wh}}_{\mathrm{DFOS}}$-2, and the (bottom left) $E_{\mathrm{T}}^{\mathrm{miss}}$ and (bottom right) m_{T} distributions in $\mathrm{SR}^{\mathrm{WZ}}_{0\mathrm{j}}$ (with all SR-i bins of $\mathrm{SR}^{\mathrm{WZ}}_{0\mathrm{j}}$ summed up). The SR selections are applied for each distribution, except for the variable shown, for which the selection is indicated by an arrow. The first (last) bin includes underflow (overflow). The "Others" category contains backgrounds from single-top, WW, triboson, Higgs and rare top processes, except in the top panels, where triboson and Higgs production contributions are shown separately, and $t\bar{t}$ +X is merged into Others. Distributions for $\widetilde{\chi}_1^{\pm}\widetilde{\chi}_2^0 \rightarrow WZ/Wh$ signals are overlaid, with mass values given as $(m(\widetilde{\chi}_1^{\pm}), m(\widetilde{\chi}_1^0))$ GeV. The bottom panel shows the ratio of the observed data to the predicted yields. The hatched bands indicate the combined theoretical, experimental, and MC statistical uncertainties.

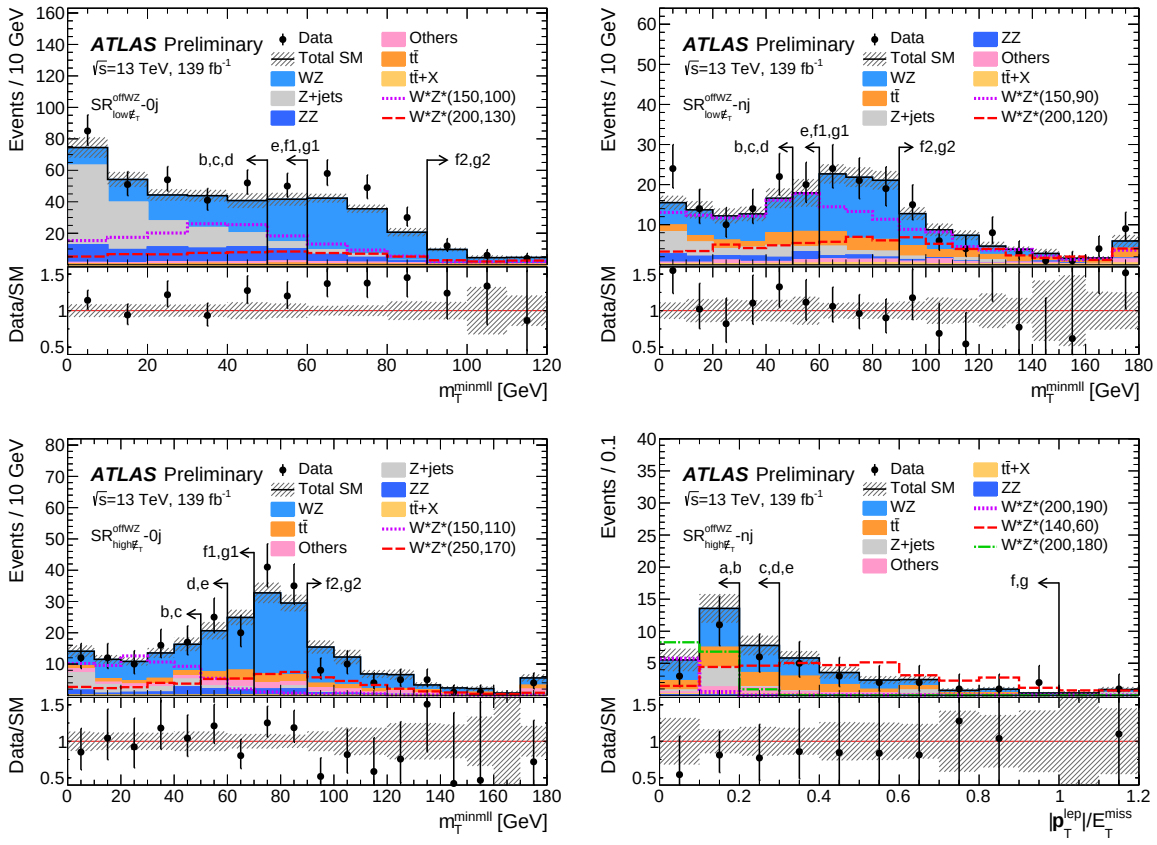

Figure 16: Kinematic distributions after the background-only fit showing the data and the post-fit expected background, in SRs of the off-shell WZ selection. The figure shows the $m_{\mathrm{T}}^{\mathrm{mllmin}}$ distribution in (top left) $\mathrm{SR}^{\mathtt{offWZ}}_{\mathtt{low}\not{E}_{\mathrm{T}}}\mathtt{-0j}$, (top right) $\mathrm{SR}^{\mathtt{offWZ}}_{\mathtt{low}\not{E}_{\mathrm{T}}}\mathtt{-nj}$ and (bottom left) $\mathrm{SR}^{\mathtt{offWZ}}_{\mathtt{high}\not{E}_{\mathrm{T}}}\mathtt{-0j}$, and the $|\mathbf{p}_{\mathrm{T}}^{\mathrm{lep}}|/E_{\mathrm{T}}^{\mathrm{miss}}$ distribution in (bottom right) $\mathrm{SR}^{\mathtt{offWZ}}_{\mathtt{high}\not{E}_{\mathrm{T}}}\mathtt{-nj}$. The contributing $m_{\ell\ell}^{\mathrm{min}}$ mass bins within each $\mathrm{SR}^{\mathtt{offWZ}}$ category are summed together. The SR selections are applied for each distribution, except for the variable shown, for which the selection is indicated by an arrow. The first (last) bin includes underflow (overflow). The "Others" category contains backgrounds from single-top, WW, triboson, Higgs and rare top processes. Distributions for $\tilde{\chi}_1^{\pm}\tilde{\chi}_2^0 \rightarrow W^*Z^*$ signals are overlaid, with mass values given as $(m(\tilde{\chi}_1^{\pm}), m(\tilde{\chi}_1^0))$ GeV. The bottom panel shows the ratio of the observed data to the predicted yields. The hatched bands indicate the combined theoretical, experimental, and MC statistical uncertainties.

Table 16: Summary of the selection criteria for the inclusive SRs in the on-shell WZ and Wh selections.

	SR^{WZ} ($m_{\ell\ell} \in [75, 105]$ GeV)			
	$n_{\text{jets}} = 0$		$n_{\text{jets}} > 0$	
m_{T} [GeV]	$E_{\text{T}}^{\text{miss}}$ [GeV]			
[100,160]	incSR^{WZ}-1: [100,200]	incSR^{WZ}-2: > 200	incSR^{WZ}-3: [150,250]	incSR^{WZ}-4: > 250
> 160	incSR^{WZ}-5: > 200		incSR^{WZ}-6: > 200	
	$\text{SR}^{\text{Wh}}_{\text{SFOS}}$ ($m_{\ell\ell} \leq 75$ GeV)			
	$n_{\text{jets}} = 0$		$n_{\text{jets}} > 0$	
m_{T} [GeV]	$E_{\text{T}}^{\text{miss}}$ [GeV]			
[0,100]	$\text{incSR}^{\text{Wh}}_{\text{SFOS}}$-7: > 50		-	
[100, 160]	$\text{incSR}^{\text{Wh}}_{\text{SFOS}}$-8: > 50		$\text{incSR}^{\text{Wh}}_{\text{SFOS}}$-9: > 75	
> 160	$\text{incSR}^{\text{Wh}}_{\text{SFOS}}$-10: > 50		$\text{incSR}^{\text{Wh}}_{\text{SFOS}}$-11: > 75	
	$\text{SR}^{\text{Wh}}_{\text{DFOS}}$			
	$\text{incSR}^{\text{Wh}}_{\text{DFOS}}$-12: $n_{\text{jets}} \in [0, 2]$, $\Delta R_{\text{OS,near}} < 1.2$, 3rd lepton p_{T} >20 GeV			

Table 17: Summary of the selection criteria for the inclusive SRs in the off-shell WZ selection.

	$\text{incSR}^{\text{offWZ}}_{\text{high}\not{E}_{\text{T}}}$-nj			
	a	b	c1	c2
$m_{\ell\ell}^{\text{min}}$ [GeV]	[1,12]	[12,15]	[1,20]	[15,20]
	$\text{SR}^{\text{offWZ}}_{\text{high}\not{E}_{\text{T}}}$-nj[a]	$\text{SR}^{\text{offWZ}}_{\text{high}\not{E}_{\text{T}}}$-nj[b]	$\text{SR}^{\text{offWZ}}_{\text{high}\not{E}_{\text{T}}}$-nj[a-c]	$\text{SR}^{\text{offWZ}}_{\text{high}\not{E}_{\text{T}}}$-nj[c]
	$\text{incSR}^{\text{offWZ}}_{\text{low}\not{E}_{\text{T}}}$		$\text{incSR}^{\text{offWZ}}_{\text{high}\not{E}_{\text{T}}}$	
	b	c	b	c
$m_{\ell\ell}^{\text{min}}$ [GeV]	[12,15]	[12,20]	[12,15]	[12,20]
	$\text{SR}^{\text{offWZ}}_{\text{low}\not{E}_{\text{T}}}$-0j[b], $\text{SR}^{\text{offWZ}}_{\text{low}\not{E}_{\text{T}}}$-nj[b]	$\text{SR}^{\text{offWZ}}_{\text{low}\not{E}_{\text{T}}}$-0j[b-c], $\text{SR}^{\text{offWZ}}_{\text{low}\not{E}_{\text{T}}}$-nj[b-c]	$\text{SR}^{\text{offWZ}}_{\text{high}\not{E}_{\text{T}}}$-0j[b], $\text{SR}^{\text{offWZ}}_{\text{high}\not{E}_{\text{T}}}$-nj[b]	$\text{SR}^{\text{offWZ}}_{\text{high}\not{E}_{\text{T}}}$-0j[b-c], $\text{SR}^{\text{offWZ}}_{\text{high}\not{E}_{\text{T}}}$-nj[b-c]
	$\text{incSR}^{\text{offWZ}}$			
	d	e1	e2	f1	f2
$m_{\ell\ell}^{\text{min}}$ [GeV]	[12,30]	[12,40]	[20,40]	[12,60]	[30,60]
	$\text{SR}^{\text{offWZ}}_{\text{low}\not{E}_{\text{T}}}$-0j[b-d], $\text{SR}^{\text{offWZ}}_{\text{low}\not{E}_{\text{T}}}$-nj[b-d], $\text{SR}^{\text{offWZ}}_{\text{high}\not{E}_{\text{T}}}$-0j[b-d], $\text{SR}^{\text{offWZ}}_{\text{high}\not{E}_{\text{T}}}$-nj[b-d]	$\text{SR}^{\text{offWZ}}_{\text{low}\not{E}_{\text{T}}}$-0j[b-e], $\text{SR}^{\text{offWZ}}_{\text{low}\not{E}_{\text{T}}}$-nj[b-e], $\text{SR}^{\text{offWZ}}_{\text{high}\not{E}_{\text{T}}}$-0j[b-e], $\text{SR}^{\text{offWZ}}_{\text{high}\not{E}_{\text{T}}}$-nj[b-e]	$\text{SR}^{\text{offWZ}}_{\text{low}\not{E}_{\text{T}}}$-0j[c-e], $\text{SR}^{\text{offWZ}}_{\text{low}\not{E}_{\text{T}}}$-nj[c-e], $\text{SR}^{\text{offWZ}}_{\text{high}\not{E}_{\text{T}}}$-0j[c-e], $\text{SR}^{\text{offWZ}}_{\text{high}\not{E}_{\text{T}}}$-nj[c-e]	$\text{SR}^{\text{offWZ}}_{\text{low}\not{E}_{\text{T}}}$-0j[c-f2], $\text{SR}^{\text{offWZ}}_{\text{low}\not{E}_{\text{T}}}$-nj[c-f2], $\text{SR}^{\text{offWZ}}_{\text{high}\not{E}_{\text{T}}}$-0j[c-f2], $\text{SR}^{\text{offWZ}}_{\text{high}\not{E}_{\text{T}}}$-nj[c-f]	$\text{SR}^{\text{offWZ}}_{\text{low}\not{E}_{\text{T}}}$-0j[e-f2], $\text{SR}^{\text{offWZ}}_{\text{low}\not{E}_{\text{T}}}$-nj[e-f2], $\text{SR}^{\text{offWZ}}_{\text{high}\not{E}_{\text{T}}}$-0j[e-f2], $\text{SR}^{\text{offWZ}}_{\text{high}\not{E}_{\text{T}}}$-nj[e-f]
	$\text{incSR}^{\text{offWZ}}$			
	g1	g2	g3	g4
$m_{\ell\ell}^{\text{min}}$ [GeV]	[12,75]	[30,75]	[40,75]	[60,75]
	$\text{SR}^{\text{offWZ}}_{\text{low}\not{E}_{\text{T}}}$-0j[b-g2], $\text{SR}^{\text{offWZ}}_{\text{low}\not{E}_{\text{T}}}$-nj[b-g2], $\text{SR}^{\text{offWZ}}_{\text{high}\not{E}_{\text{T}}}$-0j[b-g2], $\text{SR}^{\text{offWZ}}_{\text{high}\not{E}_{\text{T}}}$-nj[b-g]	$\text{SR}^{\text{offWZ}}_{\text{low}\not{E}_{\text{T}}}$-0j[e-g2], $\text{SR}^{\text{offWZ}}_{\text{low}\not{E}_{\text{T}}}$-nj[e-g2], $\text{SR}^{\text{offWZ}}_{\text{high}\not{E}_{\text{T}}}$-0j[e-g2], $\text{SR}^{\text{offWZ}}_{\text{high}\not{E}_{\text{T}}}$-nj[e-g]	$\text{SR}^{\text{offWZ}}_{\text{low}\not{E}_{\text{T}}}$-0j[f1-g2], $\text{SR}^{\text{offWZ}}_{\text{low}\not{E}_{\text{T}}}$-nj[f1-g2], $\text{SR}^{\text{offWZ}}_{\text{high}\not{E}_{\text{T}}}$-0j[f1-g2], $\text{SR}^{\text{offWZ}}_{\text{high}\not{E}_{\text{T}}}$-nj[f1-g]	$\text{SR}^{\text{offWZ}}_{\text{low}\not{E}_{\text{T}}}$-0j[g1-g2], $\text{SR}^{\text{offWZ}}_{\text{low}\not{E}_{\text{T}}}$-nj[g1-g2], $\text{SR}^{\text{offWZ}}_{\text{high}\not{E}_{\text{T}}}$-0j[g1-g2], $\text{SR}^{\text{offWZ}}_{\text{high}\not{E}_{\text{T}}}$-nj[g]

Table 18: Observed (N_{obs}) yields after the discovery-fit and expected (N_{exp}) after the background-only fit, for the inclusive SRs of the on-shell *WZ* and *Wh* selections. The third and fourth column list the 95% CL upper limits on the visible cross-section (σ^{95}_{vis}) and on the number of signal events (S^{95}_{obs}). The fifth column (S^{95}_{exp}) shows the 95% CL upper limit on the number of signal events, given the expected number (and $\pm 1\sigma$ excursions on the expectation) of background events. The last two columns indicate the CL_b value, i.e. the confidence level observed for the background-only hypothesis, and the discovery p-value ($p(s = 0)$). If the observed yield is below the expected yield, the p-value is capped at 0.5.

SR	N_{obs}	N_{exp}	σ^{95}_{vis}[fb]	S^{95}_{obs}	S^{95}_{exp}	CL_b	$p(s = 0)$ (Z)
$\texttt{incSR}^{\texttt{WZ}}\texttt{-1}$	34	38 ±5	0.10	13.5	$15.7^{+6.7}_{-4.1}$	0.32	0.50 (0.00)
$\texttt{incSR}^{\texttt{WZ}}\texttt{-2}$	2	1.2 ±0.5	0.04	5.0	$4.0^{+1.6}_{-0.7}$	0.76	0.23 (0.73)
$\texttt{incSR}^{\texttt{WZ}}\texttt{-3}$	4	6.5 ±1.1	0.03	4.8	$6.5^{+2.6}_{-1.8}$	0.19	0.50 (0.00)
$\texttt{incSR}^{\texttt{WZ}}\texttt{-4}$	25	31 ±6	0.09	12.4	$15.4^{+6.0}_{-4.1}$	0.25	0.50 (0.00)
$\texttt{incSR}^{\texttt{WZ}}\texttt{-5}$	1	5.2 ±1.1	0.03	3.9	$5.8^{+2.2}_{-1.4}$	0.03	0.50 (0.00)
$\texttt{incSR}^{\texttt{WZ}}\texttt{-6}$	23	16 ±2	0.12	17.0	$10.3^{+3.9}_{-3.0}$	0.93	0.07 (1.48)
$\texttt{incSR}^{\texttt{Wh}}_{\texttt{SFOS}}\texttt{-7}$	174	150 ±14	0.41	57.6	$37.8^{+15.1}_{-10.6}$	0.90	0.10 (1.27)
$\texttt{incSR}^{\texttt{Wh}}_{\texttt{SFOS}}\texttt{-8}$	53	55 ±5	0.12	17.1	$18.3^{+7.4}_{-4.6}$	0.42	0.50 (0.00)
$\texttt{incSR}^{\texttt{Wh}}_{\texttt{SFOS}}\texttt{-9}$	34	36 ±4	0.10	13.8	$15.0^{+6.2}_{-4.2}$	0.40	0.50 (0.00)
$\texttt{incSR}^{\texttt{Wh}}_{\texttt{SFOS}}\texttt{-10}$	56	55 ±7	0.16	21.7	$20.5^{+8.3}_{-5.8}$	0.55	0.41 (0.22)
$\texttt{incSR}^{\texttt{Wh}}_{\texttt{SFOS}}\texttt{-11}$	41	45 ±6	0.11	15.5	$17.9^{+7.2}_{-4.8}$	0.34	0.50 (0.00)
$\texttt{incSR}^{\texttt{Wh}}_{\texttt{DFOS}}\texttt{-12}$	18	11 ±3	0.12	17.0	$10.5^{+4.2}_{-2.7}$	0.92	0.07 (1.48)

Table 19: Observed (N_{obs}) yields after the discovery-fit and expected (N_{exp}) after the background-only fit, for the inclusive SRs of the off-shell *WZ* selection. The third and fourth column list the 95% CL upper limits on the visible cross section (σ^{95}_{vis}) and on the number of signal events (S^{95}_{obs}). The fifth column (S^{95}_{exp}) shows the 95% CL upper limit on the number of signal events, given the expected number (and $\pm 1\sigma$ excursions on the expectation) of background events. The last two columns indicate the CL_b value, i.e. the confidence level observed for the background-only hypothesis, and the discovery p-value (p($s = 0$)). If the observed yield is below the expected yield, the p-value is capped at 0.5.

SR	N_{obs}	N_{exp}	σ^{95}_{vis} [fb]	S^{95}_{obs}	S^{95}_{exp}	CL_b	$p(s = 0)$ (Z)
$\texttt{incSR}^{\texttt{offWZ}}_{\texttt{high}\not{E}_T}\texttt{-nja}$	3	6.0 ±1.6	0.03	4.6	$6.3^{+2.4}_{-2.0}$	0.16	0.50 (0.00)
$\texttt{incSR}^{\texttt{offWZ}}_{\texttt{high}\not{E}_T}\texttt{-njb}$	2	1.4 ±0.6	0.03	4.8	$4.0^{+1.6}_{-0.7}$	0.71	0.30 (0.53)
$\texttt{incSR}^{\texttt{offWZ}}_{\texttt{high}\not{E}_T}\texttt{-njc1}$	7	9.5 ±2.2	0.05	7.0	$8.4^{+2.9}_{-2.2}$	0.28	0.50 (0.00)
$\texttt{incSR}^{\texttt{offWZ}}_{\texttt{high}\not{E}_T}\texttt{-njc2}$	2	2.1 ±0.8	0.03	4.7	$4.6^{+1.8}_{-1.1}$	0.52	0.50 (0.00)
$\texttt{incSR}^{\texttt{offWZ}}_{\texttt{low}\not{E}_T}\texttt{-b}$	31	36 ±4	0.09	12.1	$14.9^{+5.7}_{-4.4}$	0.25	0.50 (0.00)
$\texttt{incSR}^{\texttt{offWZ}}_{\texttt{high}\not{E}_T}\texttt{-b}$	3	3.0 ±0.9	0.04	5.4	$5.2^{+2.0}_{-1.3}$	0.53	0.05 (0.00)
$\texttt{incSR}^{\texttt{offWZ}}_{\texttt{low}\not{E}_T}\texttt{-c}$	86	88 ±7	0.17	23.1	$24.4^{+9.1}_{-6.8}$	0.44	0.50 (0.00)
$\texttt{incSR}^{\texttt{offWZ}}_{\texttt{high}\not{E}_T}\texttt{-c}$	9	9.3 ±1.5	0.06	7.7	$7.7^{+3.4}_{-1.8}$	0.50	0.50 (0.00)
$\texttt{incSR}^{\texttt{offWZ}}\texttt{-d}$	202	184 ±12	0.37	51.0	$37.0^{+14.1}_{-10.8}$	0.84	0.16 (0.99)
$\texttt{incSR}^{\texttt{offWZ}}\texttt{-e1}$	332	308 ±17	0.49	68.0	$49.3^{+19.1}_{-14.8}$	0.84	0.16 (1.00)
$\texttt{incSR}^{\texttt{offWZ}}\texttt{-e2}$	298	269 ±15	0.50	69.1	$45.5^{+17.2}_{-13.6}$	0.90	0.10 (1.29)
$\texttt{incSR}^{\texttt{offWZ}}\texttt{-f1}$	479	457 ±22	0.56	77.6	$62.7^{+22.1}_{-19.6}$	0.77	0.23 (0.75)
$\texttt{incSR}^{\texttt{offWZ}}\texttt{-f2}$	277	272 ±13	0.33	45.7	$41.9^{+17.0}_{-11.8}$	0.60	0.37 (0.34)
$\texttt{incSR}^{\texttt{offWZ}}\texttt{-g1}$	620	593 ±28	0.69	96.0	$74.3^{+28.7}_{-22.0}$	0.77	0.21 (0.79)
$\texttt{incSR}^{\texttt{offWZ}}\texttt{-g2}$	418	408 ±20	0.46	63.8	$56.7^{+22.9}_{-15.1}$	0.65	0.32 (0.47)
$\texttt{incSR}^{\texttt{offWZ}}\texttt{-g3}$	288	285 ±16	0.35	48.4	$46.6^{+18.6}_{-11.9}$	0.55	0.38 (0.30)
$\texttt{incSR}^{\texttt{offWZ}}\texttt{-g4}$	141	136 ±10	0.25	34.5	$30.6^{+13.1}_{-7.5}$	0.64	0.35 (0.39)

8.2 Constraints on *WZ* and *Wh* mediated models

Constraints on the target simplified models are derived using the nominal SRs discussed in Sections 6.1 and 7.1. Model-dependent 95% CL exclusion limits are obtained by performing the exclusion fits as described in Section 5.4. Three separate fits are performed, targeting the *WZ*-mediated model using the on-shell *WZ* and *Wh* selections, targeting the *WZ*-mediated model using the off-shell *WZ* selection, and targeting the *Wh*-mediated model using the *Wh* selection.

The expected and observed exclusion contours are reported as a function of the $\widetilde{\chi}_1^0$ and $\widetilde{\chi}_1^\pm/\widetilde{\chi}_2^0$ masses, and shown in Figures 17. For each mass point, a CL_s value is given measuring the compatibility between the observed data and the signal-plus-background prediction obtained by the exclusion fit. For the *WZ*-mediated model, the best CL_s value out of two (taken from either the simultaneous fit with the 39 bins of $\mathtt{SR}^{\mathtt{WZ}}$ and $\mathtt{SR}^{\mathtt{Wh}}$ or the one with the 31 bins of $\mathtt{SR}^{\mathtt{offWZ}}$) is quoted. For the *Wh*-mediated model, the CL_s values are taken from the simultaneous fit with the 19 bins of $\mathtt{SR}^{\mathtt{Wh}}$.

For the *WZ*-mediated model, observed (expected) limits for equal mass $\tilde{\chi}_1^\pm/\tilde{\chi}_2^0$ are set at 640 (660) GeV for massless $\tilde{\chi}_1^0$, and up to 300 (300) GeV for scenarios with mass splittings Δm between the $\tilde{\chi}_1^\pm/\tilde{\chi}_2^0$ and $\tilde{\chi}_1^0$ near m_Z, driven by the on-shell *WZ* selection. The exclusion for the scenarios with $\Delta m < m_Z$ is driven by the off-shell *WZ* selection. For $\tilde{\chi}_1^\pm$ and $\tilde{\chi}_2^0$ decaying via off-shell *WZ* bosons observed and expected limits are set up to 300 GeV for $\Delta m > 35$ GeV, and up to 200-300 GeV for Δm = 10-35 GeV. The observed (expected) limit also extends down to a lowest Δm of 7 (8) GeV for $\tilde{\chi}_1^\pm/\tilde{\chi}_2^0$ masses below 140 GeV, showing good complementary with the ATLAS electroweak compressed search published in [31] (shown as a dark grey shaded area in Figure 17, top panels) that targeted low Δm scenarios. Furthermore, constraints are calculated in the bino-wino coannihilation dark-matter scenario by determining the area in the two-dimensional mass plane that yields a thermal dark-matter relic density equal to or below the observed value. Figure 17 (top right) shows the excluded areas in the bino-wino coannihilation dark-matter scenario, where $\tilde{\chi}_1^\pm/\tilde{\chi}_2^0$ ($\tilde{\chi}_1^0$) masses are excluded up to 210 (195) GeV. For the *Wh*-mediated model, observed (expected) limits for equal mass $\tilde{\chi}_1^\pm/\tilde{\chi}_2^0$ are set up to 185 (240) GeV for $\widetilde{\chi}_1^0$ masses below 20 GeV. The observed exclusion is weaker than the expected, which is explained by the mild excess found in $\mathtt{SR}^{\mathtt{Wh}}_{\mathtt{DFOS}}$; the limits are however compatible within 2σ.

The obtained exclusion limits are greatly improved compared to the previous equivalent search presented by the ATLAS experiment using the Run 1 8 TeV dataset [30] (shown as a light grey shaded area in Figure 17, top panels), due to a combination of increased production cross section given the increased collision center-of-mass energy, larger data sample statistics, and improved analysis techniques.

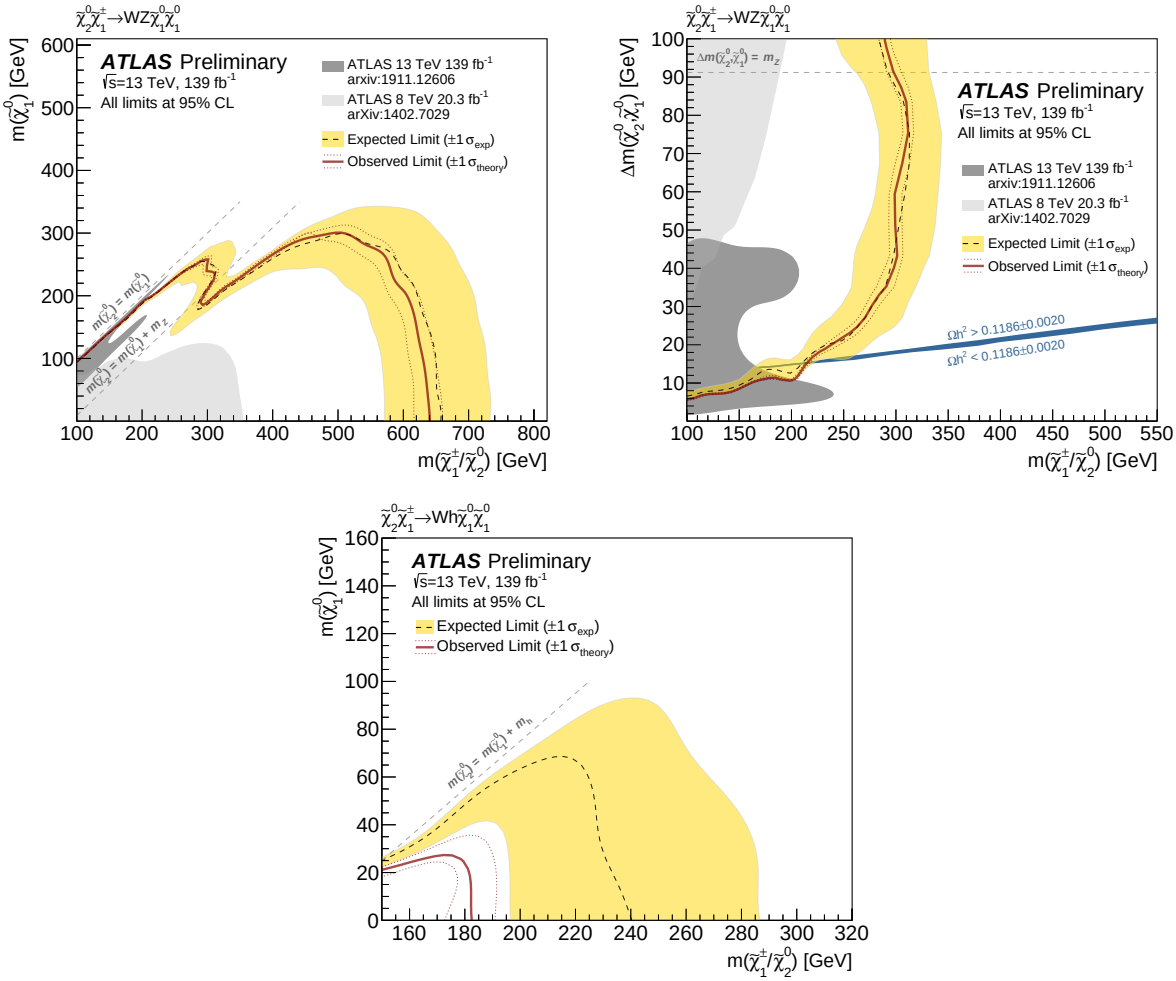

Figure 17: Exclusion limits obtained for the WZ-mediated model and the Wh-mediated model. The expected 95% CL sensitivity (dashed black line) is shown with $\pm 1\sigma_{\text{exp}}$ (yellow band) from experimental systematic uncertainties and statistical uncertainties on the data yields, the observed limit (red solid line) is shown with $\pm 1\sigma_{\text{theory}}$ (dotted red lines) from signal cross-section uncertainties. The exclusion for the WZ-mediated model is shown projected (top left) onto the $m(\widetilde{\chi}_1^{\pm}/\widetilde{\chi}_2^0)$ vs $m(\widetilde{\chi}_1^0)$ plane or (top right) onto the $m(\widetilde{\chi}_1^{\pm}/\widetilde{\chi}_2^0)$ vs Δm plane. The light and dark grey shade are the constraints obtained by the previous equivalent analysis in ATLAS using the 8 TeV 20.3 fb^{-1}dataset [30] and the compressed spectra search using the 13 TeV 139 fb^{-1}dataset [31] respectively. The dark blue line in the top right panel represents the mass splitting range that yields a dark-matter relic density equal to the observed relic density, $\Omega h^2 = 0.1186 \pm 0.0020$ [138], when the mass parameters of all the decoupled SUSY partners are set to 5 TeV and $\tan\beta$ is chosen such that the SM-like Higgs boson mass is consistent with the observed value [23]. The area above (below) the blue line represents a dark-matter relic density larger (smaller) than the observed. Exclusions on the Wh-mediated model model, projected onto the $m(\widetilde{\chi}_1^{\pm}/\widetilde{\chi}_2^0)$ vs $m(\widetilde{\chi}_1^0)$ plane, are shown in the bottom panel.

9 Conclusion

Results of a search for chargino-neutralino pair production decaying via WZ, W^*Z^* or Wh into three-lepton final states are presented. A dataset of $\sqrt{s}$ = 13 TeV proton–proton collisions corresponding to 139 fb^{-1}, collected by the ATLAS experiment at the CERN Large Hadron Collider is used. Events with three light-flavour charged leptons and missing transverse energy are preselected, and three selections are developed with a signal region strategy optimised for chargino-neutralino signals decaying via WZ, W^*Z^* and Wh, respectively. The data are found to be consistent with predictions of the Standard Model.

Assuming a simplified model with wino production, exclusion limits at 95% confidence level are placed on the minimum $\tilde{\chi}_1^\pm/\tilde{\chi}_2^0$ mass at 640 GeV for the WZ-mediated model signals in the limit of massless $\tilde{\chi}_1^0$, at 300 GeV for the mass splittings between $\tilde{\chi}_1^\pm/\tilde{\chi}_2^0$ and $\tilde{\chi}_1^0$ close to m_Z, and 200-300 GeV for the WZ-mediated model signals with a mass splitting between 10-90 GeV. The limit extends down to a smallest mass splitting of 7 GeV for $\tilde{\chi}_1^\pm$ masses below 140 GeV. A limit for Wh-mediated model signals in 3ℓ final states is set on the minimum $\tilde{\chi}_1^\pm/\tilde{\chi}_2^0$ mass at 185 GeV, for $\tilde{\chi}_1^0$ masses below 20 GeV. The limit extends down to a smallest mass splitting of 7 GeV for $\tilde{\chi}_1^\pm$ mass less than 140 GeV.

References

[1] Y. Golfand and E. Likhtman, *Extension of the Algebra of Poincare Group Generators and Violation of P Invariance*, JETP Lett. **13** (1971) 323, [Pisma Zh. Eksp. Teor. Fiz. **13** (1971) 452].

[2] D. Volkov and V. Akulov, *Is the neutrino a goldstone particle?*, Phys. Lett. B **46** (1973) 109.

[3] J. Wess and B. Zumino, *Supergauge transformations in four dimensions*, Nucl. Phys. B **70** (1974) 39.

[4] J. Wess and B. Zumino, *Supergauge invariant extension of quantum electrodynamics*, Nucl. Phys. B **78** (1974) 1.

[5] S. Ferrara and B. Zumino, *Supergauge invariant Yang-Mills theories*, Nucl. Phys. B **79** (1974) 413.

[6] A. Salam and J. Strathdee, *Super-symmetry and non-Abelian gauges*, Phys. Lett. B **51** (1974) 353.

[7] P. Fayet, *Supersymmetry and Weak, Electromagnetic and Strong Interactions*, Phys. Lett. B **64** (1976) 159.

[8] P. Fayet, *Spontaneously Broken Supersymmetric Theories of Weak, Electromagnetic and Strong Interactions*, Phys. Lett. B **69** (1977) 489.

[9] G. R. Farrar and P. Fayet, *Phenomenology of the production, decay, and detection of new hadronic states associated with supersymmetry*, Phys. Lett. B **76** (1978) 575.

[10] H. Goldberg, *Constraint on the Photino Mass from Cosmology*, Phys. Rev. Lett. **50** (1983) 1419, Erratum: Phys. Rev. Lett. **103** (2009) 099905.

[11] J. Ellis, J. Hagelin, D. V. Nanopoulos, K. A. Olive and M. Srednicki, *Supersymmetric relics from the big bang*, Nucl. Phys. B **238** (1984) 453.

[12] A. H. Chamseddine, R. L. Arnowitt and P. Nath, *Locally Supersymmetric Grand Unification*, Phys. Rev. Lett. **49** (1982) 970.

[13] R. Barbieri, S. Ferrara and C. A. Savoy, *Gauge Models with Spontaneously Broken Local Supersymmetry*, Phys. Lett. B **119** (1982) 343.

[14] G. L. Kane, C. F. Kolda, L. Roszkowski and J. D. Wells, *Study of constrained minimal supersymmetry*, Phys. Rev. D **49** (1994) 6173, arXiv: hep-ph/9312272.

[15] T. Moroi, *The Muon anomalous magnetic dipole moment in the minimal supersymmetric standard model*, Phys. Rev. D **53** (1996) 6565, [Erratum: Phys.Rev.D 56, 4424 (1997)], arXiv: hep-ph/9512396.

[16] J. L. Feng and T. Moroi, *Supernatural supersymmetry: Phenomenological implications of anomaly mediated supersymmetry breaking*, Phys. Rev. D **61** (2000) 095004, arXiv: hep-ph/9907319.

[17] M. Endo, K. Hamaguchi, S. Iwamoto and T. Kitahara, *Muon g-2 vs LHC Run 2 in Supersymmetric Models*, (2020), arXiv: 2001.11025 [hep-ph].

[18] K. Griest and D. Seckel, *Three exceptions in the calculation of relic abundances*, Phys. Rev. D **43** (1991) 3191.

[19] J. Edsjo and P. Gondolo, *Neutralino relic density including coannihilations*, Phys. Rev. D **56** (1997) 1879, arXiv: hep-ph/9704361.

[20] H. Baer et al., *Exploring the BWCA (bino-wino co-annihilation) scenario for neutralino dark matter*, JHEP **12** (2005) 011, arXiv: hep-ph/0511034.

[21] M. Ibe, A. Kamada and S. Matsumoto, *Mixed (cold+warm) dark matter in the bino-wino coannihilation scenario*, Phys. Rev. D **89** (2014) 123506, arXiv: 1311.2162 [hep-ph].

[22] S. Profumo, T. Stefaniak and L. Stephenson Haskins, *Not-so-well-tempered neutralino*, Phys. Rev. D **96** (2017) 055018, arXiv: 1706.08537 [hep-ph].

[23] G. H. Duan, K.-i. Hikasa, J. Ren, L. Wu and J. M. Yang, *Probing bino-wino coannihilation dark matter below the neutrino floor at the LHC*, Phys. Rev. D **98** (2018) 015010, arXiv: 1804.05238 [hep-ph].

[24] J. Alwall, M.-P. Le, M. Lisanti and J. G. Wacker, *Searching for directly decaying gluinos at the Tevatron*, Phys. Lett. B **666** (2008) 34, arXiv: 0803.0019 [hep-ph].

[25] J. Alwall, P. Schuster and N. Toro, *Simplified models for a first characterization of new physics at the LHC*, Phys. Rev. D **79** (2009) 075020, arXiv: 0810.3921 [hep-ph].

[26] D. Alves et al., *Simplified models for LHC new physics searches*, J. Phys. G **39** (2012) 105005, arXiv: 1105.2838 [hep-ph].

[27] ATLAS Collaboration, *Search for electroweak production of supersymmetric particles in final states with two or three leptons at $\sqrt{s} = 13$ TeV with the ATLAS detector*, Eur. Phys. J. C **78** (2018) 995, arXiv: 1803.02762 [hep-ex].

[28] ATLAS Collaboration, *Search for chargino–neutralino production using recursive jigsaw reconstruction in final states with two or three charged leptons in proton–proton collisions at $\sqrt{s} = 13$ TeV with the ATLAS detector*, Phys. Rev. D **98** (2018) 092012, arXiv: 1806.02293 [hep-ex].

[29] ATLAS Collaboration, *Search for chargino-neutralino production with mass splittings near the electroweak scale in three-lepton final states in $\sqrt{s} = 13$ TeV pp collisions with the ATLAS detector*, Phys. Rev. D **101** (2020) 072001, arXiv: 1912.08479 [hep-ex].

[30] ATLAS Collaboration, *Search for direct production of charginos and neutralinos in events with three leptons and missing transverse momentum in $\sqrt{s} = 8$ TeV pp collisions with the ATLAS detector*, JHEP **04** (2014) 169, arXiv: 1402.7029 [hep-ex].

[31] ATLAS Collaboration, *Searches for electroweak production of supersymmetric particles with compressed mass spectra in $\sqrt{s}$ = 13 TeV pp collisions with the ATLAS detector*, Phys. Rev. D **101** (2020) 052005, arXiv: 1911.12606 [hep-ex].

[32] ATLAS Collaboration, *Search for chargino and neutralino production in final states with a Higgs boson and missing transverse momentum at $\sqrt{s}$ = 13 TeV with the ATLAS detector*, Phys. Rev. D **100** (2019) 012006, arXiv: 1812.09432 [hep-ex].

[33] ATLAS Collaboration, *Search for direct production of electroweakinos in final states with missing transverse energy and a Higgs boson decaying into photons in pp collisions at $\sqrt{s}$ = 13 TeV with the ATLAS detector*, ATLAS-CONF-2019-019, 2019, URL: https://cds.cern.ch/record/2676596.

[34] CMS Collaboration, *Search for new phenomena in final states with two opposite-charge, same-flavor leptons, jets, and missing transverse momentum in pp collisions at $\sqrt{s}$ = 13 TeV*, JHEP **03** (2018) 076, arXiv: 1709.08908 [hep-ex].

[35] CMS Collaboration, *Combined search for electroweak production of charginos and neutralinos in proton–proton collisions at $\sqrt{s}$ = 13 TeV*, JHEP **03** (2018) 160, arXiv: 1801.03957 [hep-ex].

[36] CMS Collaboration, *Search for supersymmetry with a compressed mass spectrum in the vector boson fusion topology with 1-lepton and 0-lepton final states in proton–proton collisions at $\sqrt{s}$ = 13 TeV*, JHEP **08** (2019) 150, arXiv: 1905.13059 [hep-ex].

[37] CMS Collaboration, *Search for new physics in events with two soft oppositely charged leptons and missing transverse momentum in proton–proton collisions at $\sqrt{s}$ = 13 TeV*, Phys. Lett. B **782** (2018) 440, arXiv: 1801.01846 [hep-ex].

[38] CMS Collaboration, *Search for electroweak production of charginos and neutralinos in multilepton final states in proton–proton collisions at $\sqrt{s}$ = 13 TeV*, JHEP **03** (2018) 166, arXiv: 1709.05406 [hep-ex].

[39] CMS Collaboration, *Search for electroweak production of charginos and neutralinos in WH events in proton–proton collisions at $\sqrt{s}$ = 13 TeV*, JHEP **11** (2017) 029, arXiv: 1706.09933 [hep-ex].

[40] CMS Collaboration, *Search for supersymmetry with Higgs boson to diphoton decays using the razor variables at $\sqrt{s}$ = 13 TeV*, Phys. Lett. B **779** (2018) 166, arXiv: 1709.00384 [hep-ex].

[41] ATLAS Collaboration, *Evidence for the associated production of the Higgs boson and a top quark pair with the ATLAS detector*, Phys. Rev. D **97** (2018) 072003, arXiv: 1712.08891 [hep-ex].

[42] ATLAS Collaboration, *The ATLAS Experiment at the CERN Large Hadron Collider*, JINST **3** (2008) S08003.

[43] ATLAS Collaboration, *ATLAS Insertable B-Layer Technical Design Report*, ATLAS-TDR-19, 2010, URL: https://cds.cern.ch/record/1291633, Addendum: ATLAS-TDR-19-ADD-1, 2012, URL: https://cds.cern.ch/record/1451888.

[44] B. Abbott et al., *Production and integration of the ATLAS Insertable B-Layer*, JINST **13** (2018) T05008, arXiv: 1803.00844 [physics.ins-det].

[45] ATLAS Collaboration, *Performance of the ATLAS trigger system in 2015*, Eur. Phys. J. C **77** (2017) 317, arXiv: 1611.09661 [hep-ex].

[46] ATLAS Collaboration, *Luminosity determination in pp collisions at $\sqrt{s}$ = 13 TeV using the ATLAS detector at the LHC*, ATLAS-CONF-2019-021, 2019, URL: https://cds.cern.ch/record/2677054.

[47] G. Avoni et al., *The new LUCID-2 detector for luminosity measurement and monitoring in ATLAS*, JINST **13** (2018) P07017.

[48] ATLAS Collaboration, *The ATLAS Simulation Infrastructure*, Eur. Phys. J. C **70** (2010) 823, arXiv: 1005.4568 [physics.ins-det].

[49] S. Agostinelli et al., *GEANT4 – a simulation toolkit*, Nucl. Instrum. Meth. A **506** (2003) 250.

[50] ATLAS Collaboration, *The simulation principle and performance of the ATLAS fast calorimeter simulation FastCaloSim*, ATL-PHYS-PUB-2010-013, 2010, URL: https://cds.cern.ch/record/1300517.

[51] J. Alwall et al., *The automated computation of tree-level and next-to-leading order differential cross sections, and their matching to parton shower simulations*, JHEP **07** (2014) 079, arXiv: 1405.0301 [hep-ph].

[52] R. D. Ball et al., *Parton distributions with LHC data*, Nucl. Phys. B **867** (2013) 244, arXiv: 1207.1303 [hep-ph].

[53] W. Beenakker et al., *The Production of Charginos/Neutralinos and Sleptons at Hadron Colliders*, Phys. Rev. Lett. **83** (1999) 3780, arXiv: hep-ph/9906298, Erratum: Phys. Rev. Lett. **100** (2008) 029901.

[54] J. Debove, B. Fuks and M. Klasen, *Threshold resummation for gaugino pair production at hadron colliders*, Nucl. Phys. B **842** (2011) 51, arXiv: 1005.2909 [hep-ph].

[55] B. Fuks, M. Klasen, D. R. Lamprea and M. Rothering, *Gaugino production in proton-proton collisions at a center-of-mass energy of 8 TeV*, JHEP **10** (2012) 081, arXiv: 1207.2159 [hep-ph].

[56] B. Fuks, M. Klasen, D. R. Lamprea and M. Rothering, *Precision predictions for electroweak superpartner production at hadron colliders with RESUMMINO*, Eur. Phys. J. C **73** (2013) 2480, arXiv: 1304.0790 [hep-ph].

[57] J. Fiaschi and M. Klasen, *Neutralino-chargino pair production at NLO+NLL with resummation-improved parton density functions for LHC Run II*, Phys. Rev. D **98** (2018) 055014, arXiv: 1805.11322 [hep-ph].

[58] C. Borschensky et al., *Squark and gluino production cross sections in pp collisions at* $\sqrt{s} = 13, 14, 33$ *and* 100 *TeV*, Eur. Phys. J. C **74** (2014) 3174, arXiv: 1407.5066 [hep-ph].

[59] ATLAS Collaboration, *Multi-Boson Simulation for* 13 *TeV ATLAS Analyses*, ATL-PHYS-PUB-2017-005, 2017, URL: https://cds.cern.ch/record/2261933.

[60] E. Bothmann et al., *Event Generation with Sherpa 2.2*, (2019), arXiv: 1905.09127 [hep-ph].

[61] R. D. Ball et al., *Parton distributions for the LHC Run II*, JHEP **04** (2015) 040, arXiv: 1410.8849 [hep-ph].

[62] ATLAS Collaboration, *ATLAS simulation of boson plus jets processes in Run 2*, ATL-PHYS-PUB-2017-006, 2017, URL: https://cds.cern.ch/record/2261937.

[63] C. Anastasiou, L. J. Dixon, K. Melnikov and F. Petriello, *High precision QCD at hadron colliders: Electroweak gauge boson rapidity distributions at NNLO*, Phys. Rev. D **69** (2004) 094008, arXiv: hep-ph/0312266.

[64] S. Frixione, P. Nason and G. Ridolfi, *A positive-weight next-to-leading-order Monte Carlo for heavy flavour hadroproduction*, JHEP **09** (2007) 126, arXiv: 0707.3088 [hep-ph].

[65] P. Nason, *A new method for combining NLO QCD with shower Monte Carlo algorithms*, JHEP **11** (2004) 040, arXiv: hep-ph/0409146.

[66] S. Frixione, P. Nason and C. Oleari, *Matching NLO QCD computations with parton shower simulations: the POWHEG method*, JHEP **11** (2007) 070, arXiv: 0709.2092 [hep-ph].

[67] S. Alioli, P. Nason, C. Oleari and E. Re, *A general framework for implementing NLO calculations in shower Monte Carlo programs: the POWHEG BOX*, JHEP **06** (2010) 043, arXiv: 1002.2581 [hep-ph].

[68] M. Beneke, P. Falgari, S. Klein and C. Schwinn, *Hadronic top-quark pair production with NNLL threshold resummation*, Nucl. Phys. B **855** (2012) 695, arXiv: 1109.1536 [hep-ph].

[69] M. Cacciari, M. Czakon, M. Mangano, A. Mitov and P. Nason, *Top-pair production at hadron colliders with next-to-next-to-leading logarithmic soft-gluon resummation*, Phys. Lett. B **710** (2012) 612, arXiv: 1111.5869 [hep-ph].

[70] P. Bärnreuther, M. Czakon and A. Mitov, *Percent-Level-Precision Physics at the Tevatron: Next-to-Next-to-Leading Order QCD Corrections to $q\bar{q} \to t\bar{t} + X$*, Phys. Rev. Lett. **109** (2012) 132001, arXiv: 1204.5201 [hep-ph].

[71] M. Czakon and A. Mitov, *NNLO corrections to top-pair production at hadron colliders: the all-fermionic scattering channels*, JHEP **12** (2012) 054, arXiv: 1207.0236 [hep-ph].

[72] M. Czakon and A. Mitov, *NNLO corrections to top pair production at hadron colliders: the quark-gluon reaction*, JHEP **01** (2013) 080, arXiv: 1210.6832 [hep-ph].

[73] M. Czakon, P. Fiedler and A. Mitov, *Total Top-Quark Pair-Production Cross Section at Hadron Colliders Through $O(\alpha_S^4)$*, Phys. Rev. Lett. **110** (2013) 252004, arXiv: 1303.6254 [hep-ph].

[74] M. Czakon and A. Mitov, *Top++: A program for the calculation of the top-pair cross-section at hadron colliders*, Comput. Phys. Commun. **185** (2014) 2930, arXiv: 1112.5675 [hep-ph].

[75] E. Re, *Single-top Wt-channel production matched with parton showers using the POWHEG method*, Eur. Phys. J. C **71** (2011) 1547, arXiv: 1009.2450 [hep-ph].

[76] N. Kidonakis, *Two-loop soft anomalous dimensions for single top quark associated production with a W- or H-*, Phys. Rev. **D82** (2010) 054018, arXiv: 1005.4451 [hep-ph].

[77] N. Kidonakis, 'Top Quark Production', *Proceedings, Helmholtz International Summer School on Physics of Heavy Quarks and Hadrons (HQ 2013): JINR, Dubna, Russia, July 15-28, 2013*, 2014 139, arXiv: 1311.0283 [hep-ph].

[78] R. Frederix, E. Re and P. Torrielli, *Single-top t-channel hadroproduction in the four-flavour scheme with POWHEG and aMC@NLO*, JHEP **09** (2012) 130, arXiv: 1207.5391 [hep-ph].

[79] S. Alioli, P. Nason, C. Oleari and E. Re, *NLO single-top production matched with shower in POWHEG: s- and t-channel contributions*, JHEP **09** (2009) 111, [Erratum: JHEP02,011(2010)], arXiv: 0907.4076 [hep-ph].

[80] M. Aliev et al., *HATHOR – HAdronic Top and Heavy quarks crOss section calculatoR*, Comput. Phys. Commun. **182** (2011) 1034, arXiv: 1007.1327 [hep-ph].

[81] P. Kant et al., *HatHor for single top-quark production: Updated predictions and uncertainty estimates for single top-quark production in hadronic collisions*, Comput. Phys. Commun. **191** (2015) 74, arXiv: 1406.4403 [hep-ph].

[82] H. B. Hartanto, B. Jäger, L. Reina and D. Wackeroth, *Higgs boson production in association with top quarks in the POWHEG BOX*, Phys. Rev. D **91** (2015) 094003, arXiv: 1501.04498 [hep-ph].

[83] D. de Florian et al., *Handbook of LHC Higgs Cross Sections: 4. Deciphering the Nature of the Higgs Sector*, (2016), arXiv: 1610.07922 [hep-ph].

[84] C. Anastasiou et al., *High precision determination of the gluon fusion Higgs boson cross-section at the LHC*, JHEP **05** (2016) 058, arXiv: 1602.00695 [hep-ph].

[85] C. Anastasiou, C. Duhr, F. Dulat, F. Herzog and B. Mistlberger, *Higgs Boson Gluon-Fusion Production in QCD at Three Loops*, Phys. Rev. Lett. **114** (2015) 212001, arXiv: 1503.06056 [hep-ph].

[86] F. Dulat, A. Lazopoulos and B. Mistlberger, *iHixs 2 – Inclusive Higgs cross sections*, Comput. Phys. Commun. **233** (2018) 243, arXiv: 1802.00827 [hep-ph].

[87] U. Aglietti, R. Bonciani, G. Degrassi and A. Vicini, *Two-loop light fermion contribution to Higgs production and decays*, Phys. Lett. B **595** (2004) 432, arXiv: hep-ph/0404071.

[88] S. Actis, G. Passarino, C. Sturm and S. Uccirati, *NLO electroweak corrections to Higgs boson production at hadron colliders*, Phys. Lett. B **670** (2008) 12, arXiv: 0809.1301 [hep-ph].

[89] M. Bonetti, K. Melnikov and L. Tancredi, *Higher order corrections to mixed QCD-EW contributions to Higgs boson production in gluon fusion*, Phys. Rev. D **97** (2018) 056017, [Erratum: Phys. Rev. D 97 (2018) 099906], arXiv: 1801.10403 [hep-ph].

[90] M. Ciccolini, A. Denner and S. Dittmaier, *Strong and Electroweak Corrections to the Production of Higgs + 2 Jets via Weak Interactions at the Large Hadron Collider*, Phys. Rev. Lett. **99** (2007) 161803, arXiv: 0707.0381 [hep-ph].

[91] M. Ciccolini, A. Denner and S. Dittmaier, *Electroweak and QCD corrections to Higgs production via vector-boson fusion at the CERN LHC*, Phys. Rev. D **77** (2008) 013002, arXiv: 0710.4749 [hep-ph].

[92] P. Bolzoni, F. Maltoni, S.-O. Moch and M. Zaro, *Higgs Boson Production via Vector-Boson Fusion at Next-to-Next-to-Leading Order in QCD*, Phys. Rev. Lett. **105** (2010) 011801, arXiv: 1003.4451 [hep-ph].

[93] T. Sjöstrand et al., *An introduction to PYTHIA 8.2*, Comput. Phys. Commun. **191** (2015) 159, arXiv: 1410.3012 [hep-ph].

[94] ATLAS Collaboration, *ATLAS Pythia 8 tunes to 7 TeV data*, ATL-PHYS-PUB-2014-021, 2014, URL: https://cds.cern.ch/record/1966419.

[95] S. Schumann and F. Krauss, *A parton shower algorithm based on Catani–Seymour dipole factorisation*, JHEP **03** (2008) 038, arXiv: 0709.1027 [hep-ph].

[96] J. Pumplin et al., *New Generation of Parton Distributions with Uncertainties from Global QCD Analysis*, JHEP **07** (2002) 012, arXiv: hep-ph/0201195.

[97] ATLAS Collaboration, *Measurement of the Z/γ^* boson transverse momentum distribution in pp collisions at $\sqrt{s} = 7$ TeV with the ATLAS detector*, JHEP **09** (2014) 145, arXiv: 1406.3660 [hep-ex].

[98] P. Artoisenet, R. Frederix, O. Mattelaer and R. Rietkerk, *Automatic spin-entangled decays of heavy resonances in Monte Carlo simulations*, JHEP **03** (2013) 015, arXiv: 1212.3460 [hep-ph].

[99] L. Lönnblad, *Correcting the Colour-Dipole Cascade Model with Fixed Order Matrix Elements*, JHEP **05** (2002) 046, arXiv: hep-ph/0112284.

[100] L. Lönnblad and S. Prestel, *Matching tree-level matrix elements with interleaved showers*, JHEP **03** (2012) 019, arXiv: 1109.4829 [hep-ph].

[101] T. Gleisberg and S. Höche, *Comix, a new matrix element generator*, JHEP **12** (2008) 039, arXiv: 0808.3674 [hep-ph].

[102] S. Höche, F. Krauss, M. Schönherr and F. Siegert, *A critical appraisal of NLO+PS matching methods*, JHEP **09** (2012) 049, arXiv: 1111.1220 [hep-ph].

[103] S. Catani, F. Krauss, R. Kuhn and B. R. Webber, *QCD Matrix Elements + Parton Showers*, JHEP **11** (2001) 063, arXiv: hep-ph/0109231.

[104] S. Höche, F. Krauss, S. Schumann and F. Siegert, *QCD matrix elements and truncated showers*, JHEP **05** (2009) 053, arXiv: 0903.1219 [hep-ph].

[105] S. Höche, F. Krauss, M. Schönherr and F. Siegert, *QCD matrix elements + parton showers. The NLO case*, JHEP **04** (2013) 027, arXiv: 1207.5030 [hep-ph].

[106] F. Cascioli, P. Maierhöfer and S. Pozzorini, *Scattering Amplitudes with Open Loops*, Phys. Rev. Lett. **108** (2012) 111601, arXiv: 1111.5206 [hep-ph].

[107] A. Denner, S. Dittmaier and L. Hofer, *Collier: A fortran-based complex one-loop library in extended regularizations*, Comput. Phys. Commun. **212** (2017) 220, arXiv: 1604.06792 [hep-ph].

[108] ATLAS Collaboration, *Studies on top-quark Monte Carlo modelling for Top2016*, ATL-PHYS-PUB-2016-020, 2016, URL: https://cds.cern.ch/record/2216168.

[109] S. Frixione, E. Laenen, P. Motylinski, C. D. White and B. R. Webber, *Single-top hadroproduction in association with a W boson*, JHEP **07** (2008) 029, arXiv: 0805.3067 [hep-ph].

[110] D. J. Lange, *The EvtGen particle decay simulation package*, Nucl. Instrum. Meth. A **462** (2001) 152.

[111] ATLAS Collaboration, *The Pythia 8 A3 tune description of ATLAS minimum bias and inelastic measurements incorporating the Donnachie–Landshoff diffractive model*, ATL-PHYS-PUB-2016-017, 2016, URL: https://cds.cern.ch/record/2206965.

[112] ATLAS Collaboration, *Electron and photon performance measurements with the ATLAS detector using the 2015–2017 LHC proton–proton collision data*, JINST **14** (2019) P12006, arXiv: 1908.00005 [hep-ex].

[113] ATLAS Collaboration, *Muon reconstruction performance of the ATLAS detector in proton–proton collision data at* $\sqrt{s} = 13$ *TeV*, Eur. Phys. J. C **76** (2016) 292, arXiv: 1603.05598 [hep-ex].

[114] ATLAS Collaboration, *Topological cell clustering in the ATLAS calorimeters and its performance in LHC Run 1*, Eur. Phys. J. C **77** (2017) 490, arXiv: 1603.02934 [hep-ex].

[115] M. Cacciari, G. P. Salam and G. Soyez, *The anti-*k_t *jet clustering algorithm*, JHEP **04** (2008) 063, arXiv: 0802.1189 [hep-ph].

[116] M. Cacciari, G. P. Salam and G. Soyez, *FastJet user manual*, Eur. Phys. J. C **72** (2012) 1896, arXiv: 1111.6097 [hep-ph].

[117] ATLAS Collaboration, *Performance of pile-up mitigation techniques for jets in pp collisions at* $\sqrt{s} = 8$ *TeV using the ATLAS detector*, Eur. Phys. J. C **76** (2016) 581, arXiv: 1510.03823 [hep-ex].

[118] ATLAS Collaboration, *Jet energy scale measurements and their systematic uncertainties in proton–proton collisions at* $\sqrt{s} = 13$ *TeV with the ATLAS detector*, Phys. Rev. D **96** (2017) 072002, arXiv: 1703.09665 [hep-ex].

[119] ATLAS Collaboration, *ATLAS b-jet identification performance and efficiency measurement with* $t\bar{t}$ *events in pp collisions at* $\sqrt{s} = 13$ *TeV*, Eur. Phys. J. C **79** (2019) 970, arXiv: 1907.05120 [hep-ex].

[120] ATLAS Collaboration, *E_T^{miss} performance in the ATLAS detector using 2015–2016 LHC pp collisions*, ATLAS-CONF-2018-023, 2018, URL: https://cds.cern.ch/record/2625233.

[121] ATLAS Collaboration, *Performance of missing transverse momentum reconstruction with the ATLAS detector using proton–proton collisions at $\sqrt{s}$ = 13 TeV*, Eur. Phys. J. C **78** (2018) 903, arXiv: 1802.08168 [hep-ex].

[122] ATLAS Collaboration, *Object-based missing transverse momentum significance in the ATLAS Detector*, ATLAS-CONF-2018-038, 2018, URL: https://cds.cern.ch/record/2630948.

[123] ATLAS Collaboration, *Optimisation and performance studies of the ATLAS b-tagging algorithms for the 2017-18 LHC run*, ATL-PHYS-PUB-2017-013, 2017, URL: https://cds.cern.ch/record/2273281.

[124] ATLAS Collaboration, *Selection of jets produced in* 13 *TeV proton–proton collisions with the ATLAS detector*, ATLAS-CONF-2015-029, 2015, URL: https://cds.cern.ch/record/2037702.

[125] ATLAS Collaboration, *Tagging and suppression of pileup jets with the ATLAS detector*, ATLAS-CONF-2014-018, 2014, URL: https://cds.cern.ch/record/1700870.

[126] ATLAS Collaboration, *Search for electroweak production of charginos and sleptons decaying into final states with two leptons and missing transverse momentum in $\sqrt{s}$ = 13 TeV pp collisions using the ATLAS detector*, Eur. Phys. J. C **80** (2020) 123, arXiv: 1908.08215 [hep-ex].

[127] ATLAS Collaboration, *Search for direct production of electroweakinos in final states with one lepton, missing transverse momentum and a Higgs boson decaying into two b-jets in pp collisions at $\sqrt{s}$ = 13 TeV with the ATLAS detector*, (2019), arXiv: 1909.09226 [hep-ex].

[128] ATLAS Collaboration, *Measurement of the WW cross section in $\sqrt{s}$ = 7 TeV pp collisions with the ATLAS detector and limits on anomalous gauge couplings*, Phys. Lett. B **712** (2012) 289, arXiv: 1203.6232 [hep-ex].

[129] ATLAS Collaboration, *Prospects for Higgs boson searches using the $H \to WW^{(*)} \to \ell\nu\ell\nu$ decay mode with the ATLAS detector at* 10 *TeV*, ATL-PHYS-PUB-2010-005, 2010, URL: https://cds.cern.ch/record/1270568.

[130] M. Bahr et al., *Herwig++ physics and manual*, Eur. Phys. J. C **58** (2008) 639, arXiv: 0803.0883 [hep-ph].

[131] J. Bellm et al., *Herwig 7.0/Herwig++ 3.0 release note*, Eur. Phys. J. C **76** (2016) 196, arXiv: 1512.01178 [hep-ph].

[132] G. Cowan, K. Cranmer, E. Gross and O. Vitells, *Asymptotic formulae for likelihood-based tests of new physics*, Eur. Phys. J. C **71** (2011) 1554, arXiv: 1007.1727 [physics.data-an], Erratum: Eur. Phys. J. C **73** (2013) 2501.

[133] M. Baak et al., *HistFitter software framework for statistical data analysis*, Eur. Phys. J. C **75** (2015) 153, arXiv: 1410.1280 [hep-ex].

[134] A. L. Read, *Presentation of search results: the CL_S technique*, J. Phys. G **28** (2002) 2693.

[135] R. D. Cousins, J. T. Linnemann and J. Tucker, *Evaluation of three methods for calculating statistical significance when incorporating a systematic uncertainty into a test of the background-only hypothesis for a Poisson process*, Nucl. Instrum. Meth. A **595** (2008) 480, arXiv: physics/0702156 [physics.data-an].

[136] C. G. Lester and D. J. Summers, *Measuring masses of semi-invisibly decaying particles pair produced at hadron colliders*, Phys. Lett. B **463** (1999) 99, arXiv: hep-ph/9906349.

[137] A. Barr, C. Lester and P. Stephens, *A variable for measuring masses at hadron colliders when missing energy is expected; m_{T2}: the truth behind the glamour*, J. Phys. G **29** (2003) 2343, arXiv: hep-ph/0304226.

[138] N. Aghanim et al., *Planck 2015 results. XI. CMB power spectra, likelihoods, and robustness of parameters*, Astron. Astrophys. **594** (2016) A11, arXiv: 1507.02704 [astro-ph.CO].